BROAD-BAND SEISMIC STUDIES OF BODY WAVES

Thesis by

Lawrence James Burdick

In Partial Fulfillment of the Requirements

for the Degree of

Doctor of Philosophy

California Institute of Technology

Pasadena, California

1977

(Submitted May 16, 1977)

ACKNOWLEDGEMENTS

ABSTRACT

Analytic information from both long period and short period seis-
mometers is used in three different studies of teleseismic body waves.
The composite broad-band information is first used in a source study
of the 9/12/66 Truckee, 8/1/75 Oroville and 4/9/68 Borrego Mountain
earthquakes in California. The purpose of the study is to determine
the fault area and displacement from the body wave pulse shape and to
compare this information with the postseismic data. The pulse shapes
are determined by a simultaneous short period-long period deconvolution
procedure and matched with theoretical pulses from fault models. The
results indicate that the area which radiated the body waves was
smaller than the area of the aftershock zone and that the displacement
in this area was larger than the offsets observed at the surface. The
purpose of the second study is to find the value of t^*_β for teleseismic
S waves with a raypath under the continental United States. The data
set consists of long and short period body waves from the Borrego
Mountain earthquake as observed in the northeastern U. S. The P
waveforms are dominated by the sP phase and the SH waveforms by the sS.
It is assumed that there are no losses in pure compression so that the
relative attenuation rate of P and S waves is known. The initial source
radiation is determined from the sP phase and the value of t^*_β from the
spectral content of the S wave. The results indicate that t^*_β is
5.2 ± .7 seconds along this raypath. Long and short period body waves
from some deep South American events are used to test for lateral
asymmetry of the Q distribution under the U. S. The results indicate

that the attenuation rate of teleseismic body waves is roughly constant across the North American continent. The t_β^* value for a 600 km deep earthquake appears to be about 3. seconds. The purpose of the final study is to find an upper mantle compressional velocity profile which explains both the short period and long period waveform data. The region of study is the western or tectonically active portion of the United States. The short period waveforms are from NTS bombs and the long period waveforms are from shallow California earthquakes with known source mechanisms. Travel time and apparent velocity data are also used to constrain the model. The new velocity profile is called T7. It accurately predicts the long and short period body waveshapes from 10° to 30°. The new model is substantially different than the previous one for the region. The first discontinuity is at 400 km depth which is shallower than before and the second is at 670 km which is deeper. The velocity jumps have been reduced in size to 5% and 4% respectively. The velocities through much of the profile have been reduced slightly to improve the fit to the travel time data.

TABLE OF CONTENTS

INTRODUCTION

The world-wide seismograph station network has been in operation
for a period of more than ten years. It has provided global coverage
of moderate to large seismic events from nearly every major tectonically
active zone. Each station in the net has recorded the events on two
different seismic instruments. One is a long period Sprengnether and
the other is a short period Benioff seismometer. The long period
instrument has its peak response at around 15 seconds and effectively
filters out periods shorter than about 2 seconds. Its long period
response extends to beyond 100 seconds. The short period instrument
has its peak response at about .7 seconds. It filters out information
at periods longer than 2 seconds or shorter than .1 seconds. Records
from the short period instrument are most commonly used only for the
purpose of measuring arrival times of body wave phases. Most studies
of the shape or frequency content of body waves are based on the records
from the long period instrument. This is because the seismic information
at longer periods is inherently more stable. However, it is also
inherently less sensitive to the details of either the seismic velocity
structure or the seismic sources. This thesis presents three different
studies in which the records from the instruments are used together
as a single broad-band measurement of the analytic content of body
waves. This technique takes advantage of both the stability of the
information at longer periods and the sensitivity of the information
at shorter periods.

The understanding of the basic processes which affect the wave-
forms of body waves has advanced very rapidly in the last three or

four years. At the beginning of that time, there was a poor correspondence between the waveforms predicted by reasonable dislocation models of the seismic source and observed body waves. Most source models predicted that the far field wave pulse for a small to moderate sized earthquake should be a simple spike. The only observations which the models appeared to explain were those from deep earthquakes. The work of several different authors including Helmberger (1974) and Fukao (1971) showed that the pulse shape of the body waves from shallow events can be strongly affected by the interaction of the wave with the free surface. The work of Burdick and Mellman (1976) and Langston (1976) verified that most of the complexity of the body waves from moderate sized, shallow earthquakes could be modeled as the interaction of a simple pulse with the free surface. The subsequent work of Burdick and Langston (1977) and Langston (1976) showed that the complexity is also caused by the crustal velocity structure near the source and near the receiver. The techniques which were developed in the course of this research were the basic analytic tools used in all of the studies to be presented here.

The first investigation in which waveform analysis techniques are applied to short and long period records is a modeling study of the sources of three shallow earthquakes. Many previous studies which employed other methods showed that there is a rough correlation between the fault areas and average fault displacements computed from the body waves and the corresponding quantities determined from the surface offsets and aftershock zone areas. The results of the current study

indicate that the body waves may be radiated from an area smaller than the aftershock zone which has displacements larger than the measured surface offsets. The composite instrument system allows an accurate determination of the shape of the far field body wave pulses which in turn allows a determination of the fault area. The second study is a determination of the rate of attenuation of body waves beneath the North American continent. The short period S wave records are very useful because they are the most strongly attenuated. The long period S records can be used to normalize the short period S's, and the P wave records can be used to constrain the initial source radiation. The last study is a modeling study of the upper mantle compressional velocity profile. Short period P waveform data have been commonly used in this type of study in the past. Long period P waveforms can now be used in conjunction with the short periods because of the new methods for modeling the long period source. The appendices outline the methods for computing the response curve of the short period WWSSN instrument and for computing and plotting focal hemispheres for S waves. They also review the results of some important long period waveform modeling studies.

Chapter 1.

ESTIMATION OF FAULT AREA FROM BODY WAVE TIME FUNCTIONS

INTRODUCTION

The extent of the area on the fault plane which fractures during an earthquake is generally estimated using one of two different approaches. One method is to assume that the area covered by the aftershocks which occur in the first day or so after the main event will be the same as the failure zone (Kanamori and Anderson, 1975; Aki, 1972; Tsai and Aki, 1970). A second method is to model the asymmetry in the surface wave radiation, the body wave pulse shape or the static displacement in terms of a dislocation in an elastic medium (Kanamori, 1970 a, b; Savage, 1966, Savage and Hastie, 1966). The purpose of this report will be to present some new fault area estimates made from body wave pulses and to compare them with corresponding estimates made from aftershock zones. The determination of the body wave pulse shapes has been made using a sensitive new deconvolution technique. It uses information from both a long period record and a short period record to find a pulse shape which is compatible with both. The observed pulses have been interpreted in terms of kinematic fault models which are as realistic as possible.

The pulse shape method of fault area estimation has been used on three California earthquakes. These are the 4/9/68 Borrego Mountain event, the 8/1/75 Oroville event and the 9/12/66 Truckee event. They were chosen because the extent of aftershocking was accurately determined for each event and also because they are of moderate size. Determination of the fault area of moderate earthquakes using dislocation models is of particular interest because it has long been suspected that the

method of using the aftershock area as a measure of the fault area may result in an overestimate in these cases. There may be significant spreading of the aftershocks beyond the failure zone. The results of this study indicate that this may indeed be the case. The estimates of fault area have been combined with moment determinations to compute the average displacements on the faults. A comparison of the computed and observed displacements places an interesting constraint on the behavior of a rupture as it propagates up to the free surface.

DETERMINATION OF EARTHQUAKE TIME FUNCTIONS

To determine the body wave pulses radiated by the earthquakes, we will use records from WWSSN stations at distance ranges between 30° and 80°. At these ranges, the waveforms will be relatively unaffected by their propagation through the earth since they bottom in the smooth lower mantle. However, the wave pulse will be strongly affected by its interference with the free surface (Helmberger, 1974; Fukao, 1971; Herrmann, 1976; Bouchon, 1976). Some care will be taken to properly correct for this effect.

The shape of the wave pulse will be measured from the records using a deconvolution technique. This approach has been used before on long period WWSSN records from deep earthquakes (Burdick and Helmberger, 1974; Mikumo, 1971). Experience from these studies shows that although the long period records give a stable result they lack sensitivity. An alternative approach would be to use records from the WWSSN short period instrument which is much more sensitive to the detail of the wave. However, deconvolution of these records is a very unstable process. To

obtain both stability and sensitivity, we will use a deconvolution technique which simultaneously uses the information from the long and the short period records.

The purpose of the deconvolution operation is to remove the effects of both instrument and Q from the observed records. It is assumed that either the short period record SP(t) or the long period record LP(t) can be written as the convolution of two operators

$$SP(t) = R_{SP}(t) * S(t) \qquad (1)$$

$$LP(t) = R_{LP}(t) * S(t) \qquad (2)$$

The operators $R_{SP}(t)$ and $R_{LP}(t)$ are the theoretical instrument responses which have already been corrected for the effects of attenuation. That is,

$$R_{SP}(t) = I_{SP}(t) * A(t) \qquad (3)$$

$$R_{LP}(t) = I_{LP}(t) * A(t) \qquad (4)$$

where $I_{SP}(t)$ and $I_{LP}(t)$ are the theoretical instrument responses for the long and short period WWSSN instruments and A(t) is Futterman's (1962) attenuation operator. A(t) is evaluated at a **t*** value of about 1. S(t) in equations 1 and 2 is the unknown source pulse. If the power spectrum of the noise were known it would be possible to obtain a least squares estimate of S(t) from each of equations 1 and 2. (Lee, 1960). However, an appropriate statistical description of the noise is very difficult to obtain. Therefore, the usual approach is to use some other method for suppressing the effects of noise in the deconvolution process (Helmberger and Wiggins, 1971; Dey-Sarkar and Wiggins, 1976b).

The first step in the simultaneous deconvolution procedure is to make a separate estimate of S(t) from each of the two records. Equation

1 and 2 are Fourier transformed and solved for $S(\omega)$.

$$S_1(\omega) = \frac{SP(\omega)}{R_{SP}(\omega)} \tag{5}$$

$$S_2(\omega) = \frac{LP(\omega)}{R_{LP}(\omega)} \tag{6}$$

where ω is the transform variable and the subscripts merely differentiate between the two separate estimates of the source pulse. A final average estimate $\overline{S}(\omega)$ is obtained by taking a weighted average of the two spectra. The high frequency noise component is suppressed by multiplying $\overline{S}(\omega)$ with a gaussian filter given by $f(\omega) = e^{-(\omega/2\pi)^2}$ The final result in time domain is given by:

$$\overline{S}(t)*f(t) = \int_{-\infty}^{\infty}[W_1(\omega)S_1(\omega) + W_2(\omega)S_2(\omega)]\ f(\omega)\ e^{i\omega t}d\omega \tag{7}$$

$W_1(\omega)$ is a weighting function which is equal to 1.0 at frequencies higher than .5 hertz and 0. at frequencies lower than .25 hertz. It falls off linearly between these values. $W_2(\omega)$ is just 1.0 minus $W_1(\omega)$. The frequency band in which the two spectra are averaged will be referred to as the crossband. As will be shown in a following section, the choice of functional form for $W_1(\omega)$ and $W_2(\omega)$ is unimportant as long as they average the two spectra in the crossband chosen here. It is important to note that the final result of the simultaneous deconvolution as given by equation 7 is not just $\overline{S}$ but a filtered version of it. This is a natural result of the fact that we cannot estimate the source spectrum at frequencies higher than the passband of the short period instrument.

Figure 1.1 is meant to illustrate that the deconvolution process does not generate new information but only allows us to look at the already resolved information through a slightly different filter or effective instrument. The short period record is just the source pulse averaged
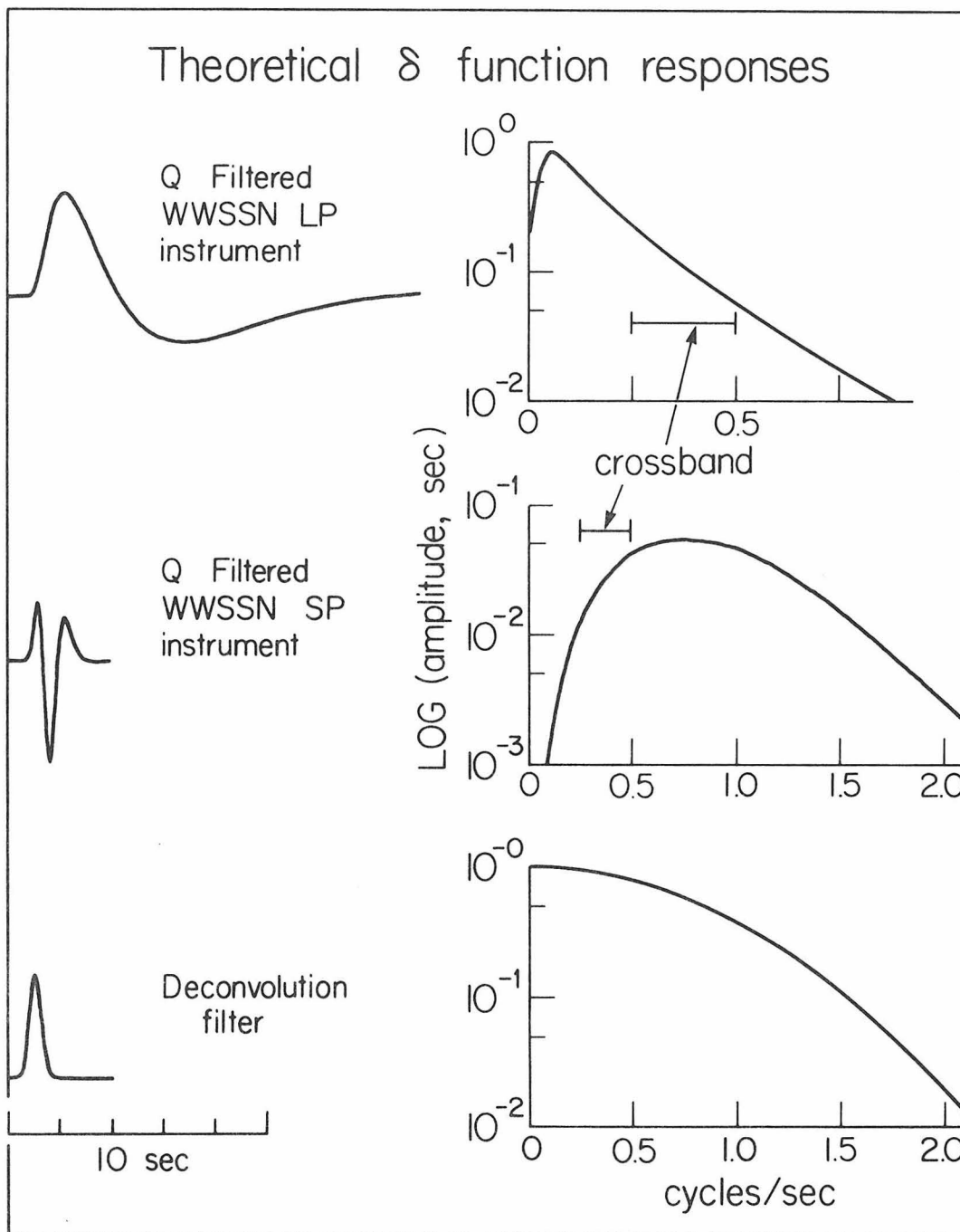
Figure 1.1   The figure compares the δ function responses of the two
WWSSN instruments to the response of the deconvolution
filter in both the time and frequency domains.   The cross-
band is the frequency band in which the information from
the two instruments is averaged together.   The information
from the spectral bands of the seismic instruments is used
to estimate the fourier spectrum in the band of the
deconvolution filter.

over by the operator at the left in the center. The final result should be the source averaged over by the operator on the bottom left. Note that the averaging length of the deconvolution filter is a little over a second. The **durations** of the swings of the short period instrument are even shorter than that. This means that we are not trying to resolve features of shorter **duration** than the original instrument system could resolve. The advantage of viewing the ground motion convolved with the gaussian filter instead of the instruments is that the pulse will be smoothed but not distorted. It is true that the filter is not causal, but this does not affect the way in which the results are interpreted. A frequency domain representation of the same filters is shown on the right of Figure 1.1. The spectra are Fourier amplitude spectra of the three different operators. Again it is shown that the deconvolution filter cuts off high frequencies slightly faster than the attenuation corrected short period instrument. The short period instrument falls off by less than an order of magnitude at low frequencies before it enters the crossband at .5 hertz. From this frequency down the long period instrument begins to **constrain the shape of the spectrum. The long period** instrument is also down by less than an order of magnitude before it enters the crossband at its high frequency end. The spectral estimate $\overline{S}$ will obviously be poor for very low frequencies, but this will be unimportant for the short record segments to be deconvolved in this study.

THEORETICAL TIME FUNCTIONS

Once the body wave pulses have been determined from the deconvolution technique, they can be interpreted in terms of a theoretical dislocation model. The class of fault models to be used for this study is the one originally described by Savage (1966). In these models, rupture is assumed to nucleate at a single point and propagate radially at constant speed to an elliptical boundary. Savage found closed form solutions for the pulse shape for two special cases. These were a circular fault with rupture initiating at a boundary and an elliptical fault with rupture initiating at a focus. His integral equations can be easily generalized to the case of rupture initiation at an arbitrary point on the ellipse by modifying the time dependent boundary conditions of the integral over the fault plane. The integrals must be evaluated numerically for this more general case. An advantage of doing the integrals numerically is that any distribution of final offset $\vec{U}$ can be specified on the fault surface. The distribution to be used for the pulses computed in this study will be the one derived by Eshelby (1957) for an elliptical crack in an elastic medium:

$$\vec{U} = U_o \ (1 - \frac{z^2}{a^2} - \frac{x^2}{b^2})^{\frac{1}{2}} \ \vec{K} \tag{8}$$

z and x are coordinates measured from the center of the ellipse along the axes, a and b are the semimajor and semiminor axes of the ellipse, U_o is the magnitude of the displacement and $\vec{K}$ is a unit vector in the direction of displacement.

The choice of rupture velocity in a kinematic fault model has always been a difficult one. The results of a model study depend critically

on the value chosen, but there are few real constraints on what the value should be. Modeling studies of surface waves seem to indicate that the rupture velocity, V_r, should be some fraction of the shear wave speed, β. Preferred values range between $.5\beta$ and β. (Kanamori, 1970 a, b; Ben-Menahem and Toksöz, 1962, 1963 a, b.) A somewhat lower value was determined by Fukao (1972) who assumed that component shocks of a multiple event deep earthquake were connected by a smoothly propagating rupture. Fortunately, the theoretical study of the mechanics of shear failure has reached the point where it can verify these observational results. Husseini and Randall (1976) have shown that V_r must be less than β for mode III fracture and must be less than the Rayleigh wave speed C_r, for mode II fracture. Depending on the stress conditions, V_r may be much smaller than C_r or β. For the following calculations, V_r was assumed to be 2.8 km/sec or about $.8\beta$.

One final modification of the theoretical pulse computational procedure which could be made would be to correct for the finite dislocation time of the two sides of the fault. This is usually achieved by convolving the pulse with a boxcar time function whose duration is the average rise time on the fault. This correction is not included in the theoretical pulses presented in the following sections. The effect of convolving in a boxcar function would only be to lengthen the duration of the theoretical pulses and we wish to submit that they are already longer than might be expected. A correction which made the theoretical pulses even longer would not change our arguments.

OBSERVED BODY WAVE PULSES

The Borrego Mountain Earthquake:

The Borrego Mountain earthquake was a magnitude 6.4 shock which occurred on 4/9/68 on the Coyote Creek fault in southern California. It was a strike slip event which had a maximum surface offset of 38 cm (Allen and Nordquist, 1972). The body waves were large enough to be seen at most stations less than 90° but they were especially well recorded in the northeastern U. S. Burdick and Mellman (1976) found an accurate model for the Borrego Mountain source by inverting the long period body wave data (see Appendix 3). This source model will play an important role in this study since it will allow us to understand and account for the interaction of the basic wave pulse with the free surface. The records chosen for deconvolution were from the WWSSN station at Weston Massachusetts (WES). The long and short period records are shown at the top of Figure 1.2. The epicentral range to WES is 36.3°. The small precursory arrivals on both records are the P and pP phases. The large positive arrival after the precursor is the sP phase.

It should be noted that not every short period record can be used to determine the source pulse through the simultaneous deconvolution procedure. This is because some stations are located on very non-uniform structure. The short period waveform becomes contaminated by large amplitude arrivals generated near the receiver. Short period records from poor quality stations tend to have a continuous train of high amplitude arrivals instead of a single clean pulse like WES. The best way to identify records which are uncontaminated by receiver phases is to compare them with other records from nearby stations. If the short period waveform is consistent between stations, it is most probably
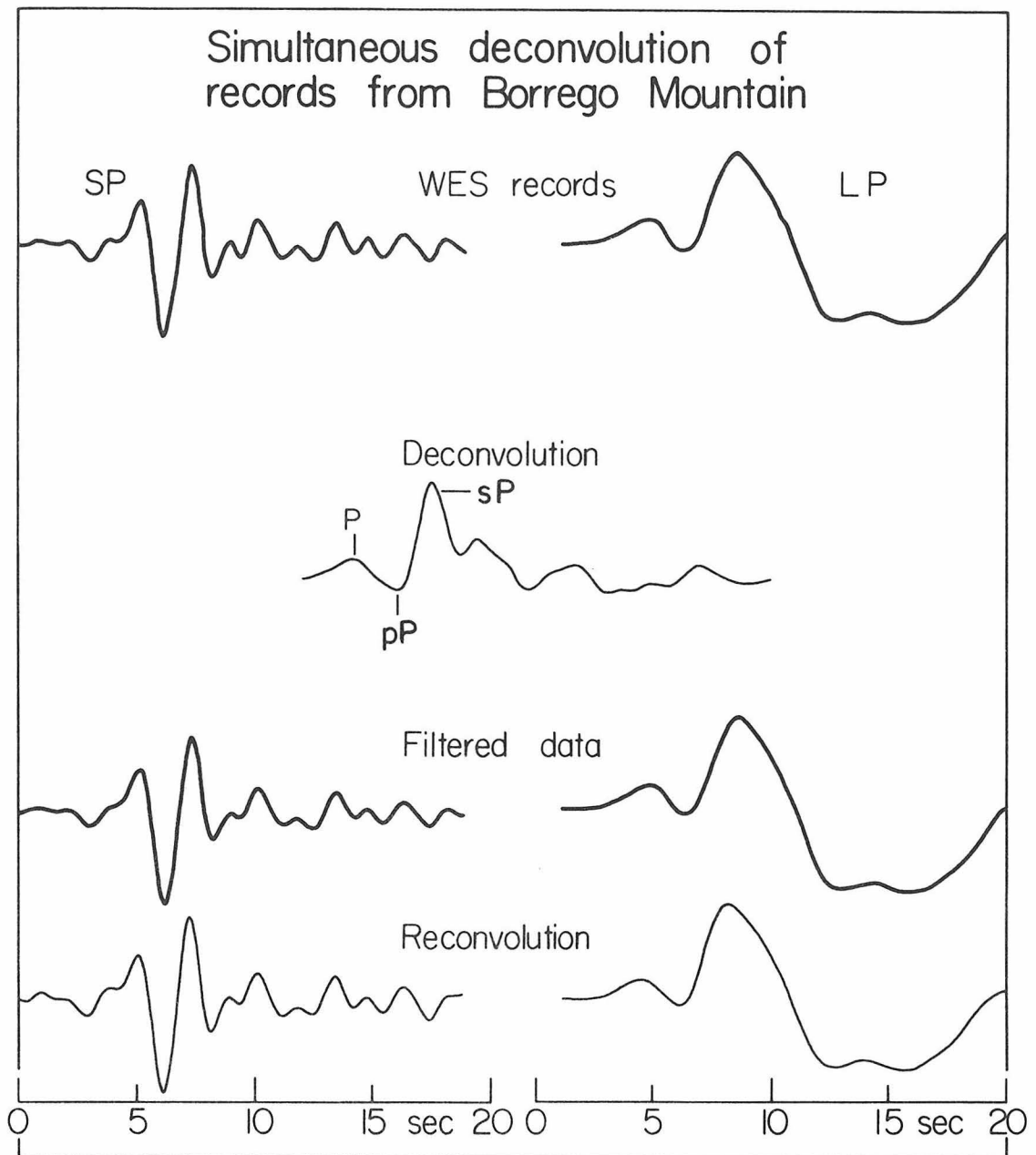
Figure 1.2 The deconvolution result which is shown in the second row is a time function which is compatible with both the long and short period records of the Borrego Mountain earthquake. It was obtained by simultaneously deconvolving the top two traces. The third row shows the data filtered by the deconvolution filter. The bottom traces are the result of reconvolving the deconvolution result with the instruments. If the deconvolution result is sufficiently stable, the bottom two rows should be the same.

a good recording. The short and long period records from Weston are almost identical to those from Ogdensberg, New Jersey (OGD) and State College, Pennsylvania (SCP).

The result of the simultaneous deconvolution is shown in the second row of Figure 1.2 As expected from the source model, the record begins with a small positive arrival which is P followed by a small negative arrival which is pP and a large positive arrival which is sP. The long and short period records have been passed through the gaussian deconvolution filter so they will be exactly comparable with the deconvolution result. They are shown in the third row of Figure 1.2. The result of the deconvolution has been reconvolved with each of the attenuation corrected instrument operators and the results have been shown on the bottom of Figure 1.2. Since both the data and the re-convolution results have been filtered with the deconvolution filter the bottom two rows of the figure should be the same.

At this point, it can be clarified why the choice of functional form for the weighting functions $W_1(\omega)$ and $W_2(\omega)$ in equation 7 does not strongly influence the result of the simultaneous deconvolution. The spectral estimates from the long and short period Weston records in the crossband of .25 to .50 hertz are compared in Figure 1.3. The two spectra are so similar that the results of the averaging do not really depend on how the two component spectra are weighted. This comparison provides some indication that the fundamental process of deconvolving the theoretical instrument response from the records is a stable one. Otherwise, the two records shown at the top of Figure 1.2, which appear very different in the time domain would not have given such similar spectral

15
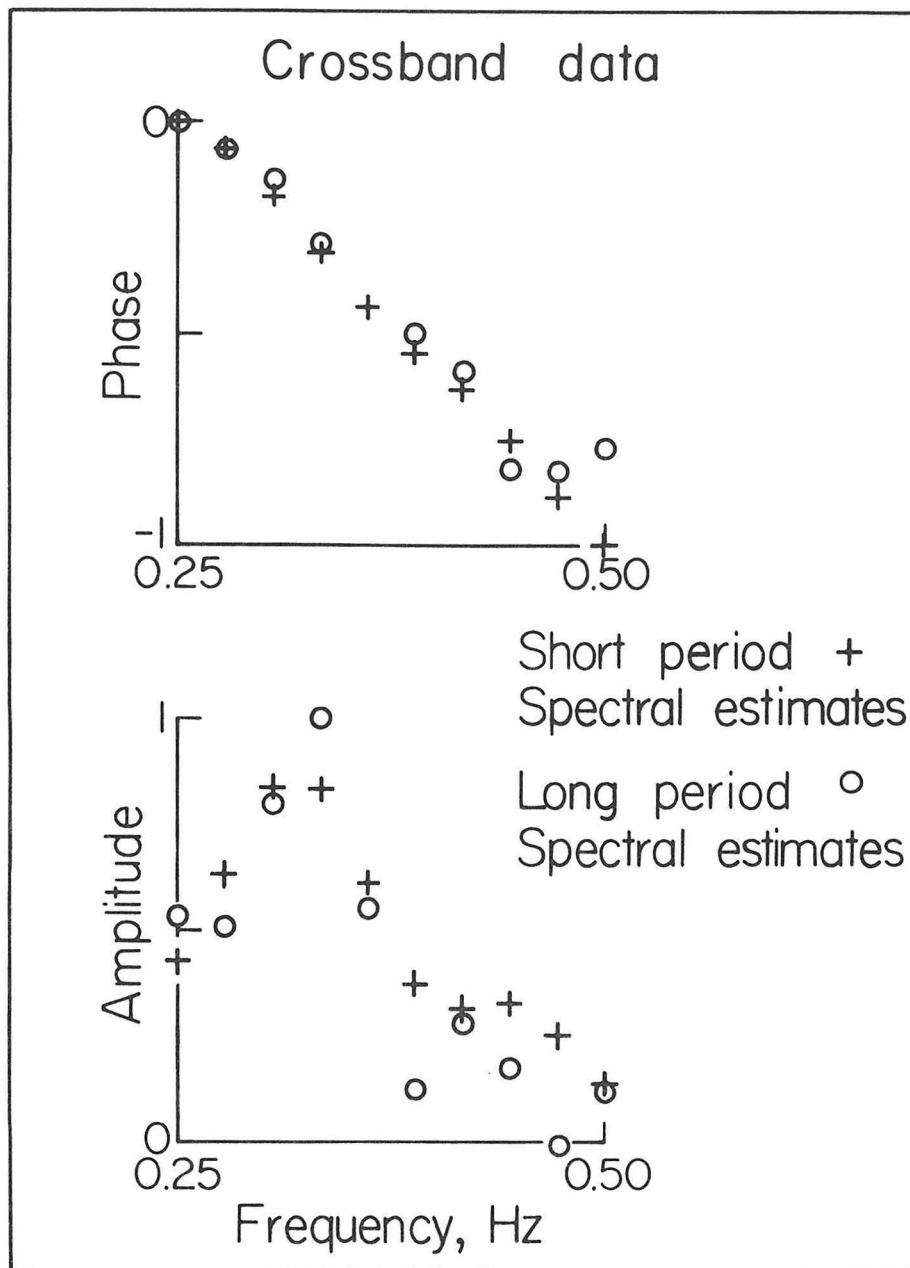
Figure 1.3 The figure shows spectral estimates of the ground motion at WES for Borrego Mountain from both the short period (crosses) and long period (circles) records. The good agreement between the spectra indicates that both instruments are still recording reliably in the crossband.

estimates in the crossband.

The Oroville Earthquake:

The 8/1/75 Oroville earthquake in northern California had a magnitude of 5.7. It was a normal fault with a small component of left lateral motion which occurred at 5.5 km depth. The depth and focal mechanisms were determined by Langston and Butler (1976) from a study of the long period waveforms. The fit of the theoretical model to the observed long period waveforms has been reproduced in Appendix 3. The records from the WWSSN station at Nurmijarvi, Finland (NUR) at a range of 76.6° were selected for deconvolution. The records are shown in Figure 1.4. Very similar long and short period waveforms were observed at Kevo, Finland (KEV) and Kongsberg, Norway (KON). Because the earthquake was only 5.5 km deep, the interaction between the direct arrival and surface reflections is very strong. From the fault plane solution, we know that the P wave has the strongest amplitude and a negative polarity. The pP and sP phases have about half the amplitude of the direct arrival, and they break upward. Since the two surface reflections come in only .7 seconds apart they can't be resolved by the deconvolution. The arrivals are marked on the deconvolution result in Figure 1.4. As shown at the bottom of the figure, the deconvolution procedure appears to have worked well again.

The Truckee Earthquake:

The 9/12/66, magnitude 6 Truckee earthquake was another strike slip event. It occurred at a depth of 10 km in northern California very near the location of the Oroville shock. The focal mechanism was determined from the first motion data by Tsai and Aki (1970). They also demonstrated
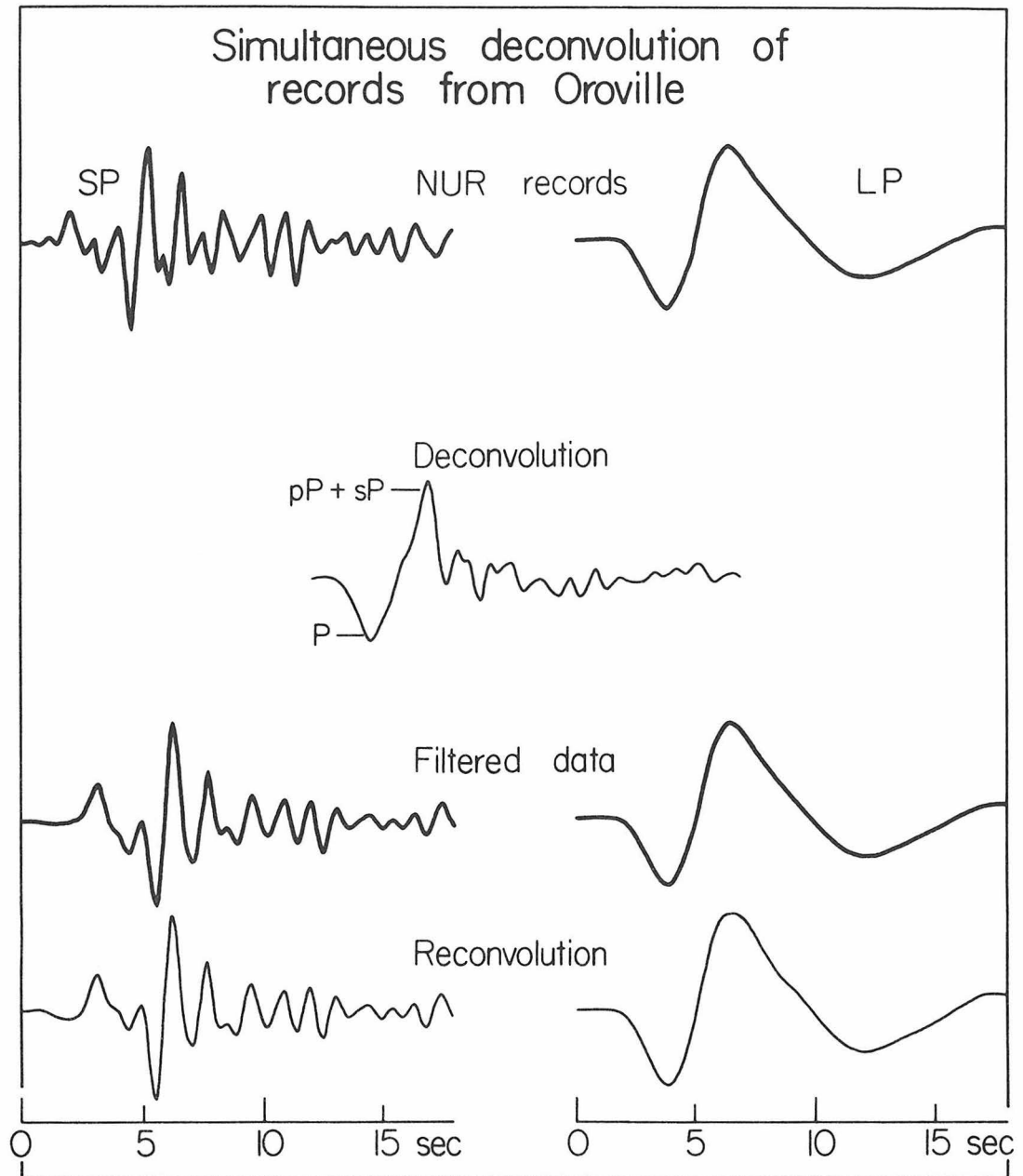
Figure 1.4 The deconvolution result which is shown in the second row is a time function which is compatible with both the long and short period records of the Oroville earthquake. It was obtained by simultaneously deconvolving the top two traces. The third row shows the data filtered by the deconvolution filter. The bottom traces are the result of reconvolving the deconvolution result with the instruments. If the deconvolution result is sufficiently stable, the bottom two rows should be the same.

that the available surface wave data are compatible with this mechanism.
A strike slip radiation pattern tends to radiate much less energy down-
ward than a dip slip pattern. Therefore, the Truckee event produced
many fewer high quality records at teleseismic distances than did the
Oroville shock. Those records which were of acceptable quality have been
shown to fit the focal mechanism of Tsai and Aki in Appendix 3. There
was only one good quality long period P wave from beyond 30°. It was
recorded at Blacksberg, Virginia (BLA) at a range of 31.1°. A good
quality short period record came from the nearby station of Ogdensburg,
New Jersey (OGD). A theoretical calculation from the source model
shows that the source should have radiated nearly identical pulses to
these two stations, so the deconvolution procedure was tried on this
record pair. As shown in Figure 1.5, the results seem to be acceptable
although not as good as in the cases where both records were from the
same station. The interference pattern for Truckee is the same as it
was for the other strike slip event, Borrego Mountain. As shown in
Figure 1.5, the P is small and breaks upward, the pP is also small and
breaks downward, and the sP is large and breaks upward.

TIME FUNCTIONS AND AFTERSHOCK ZONES

We now have estimates of the body wave pulses that were radiated
by the three earthquakes as shown in Figures 1.2, 1.4 and 1.5. The
Savage source models provide the means to calculate theoretical pulses
for a specified region of faulting. Estimates of the sizes of the after-
shock zones of the events can be obtained from various studies which
have been reported in the literature. This enables us to find out whether
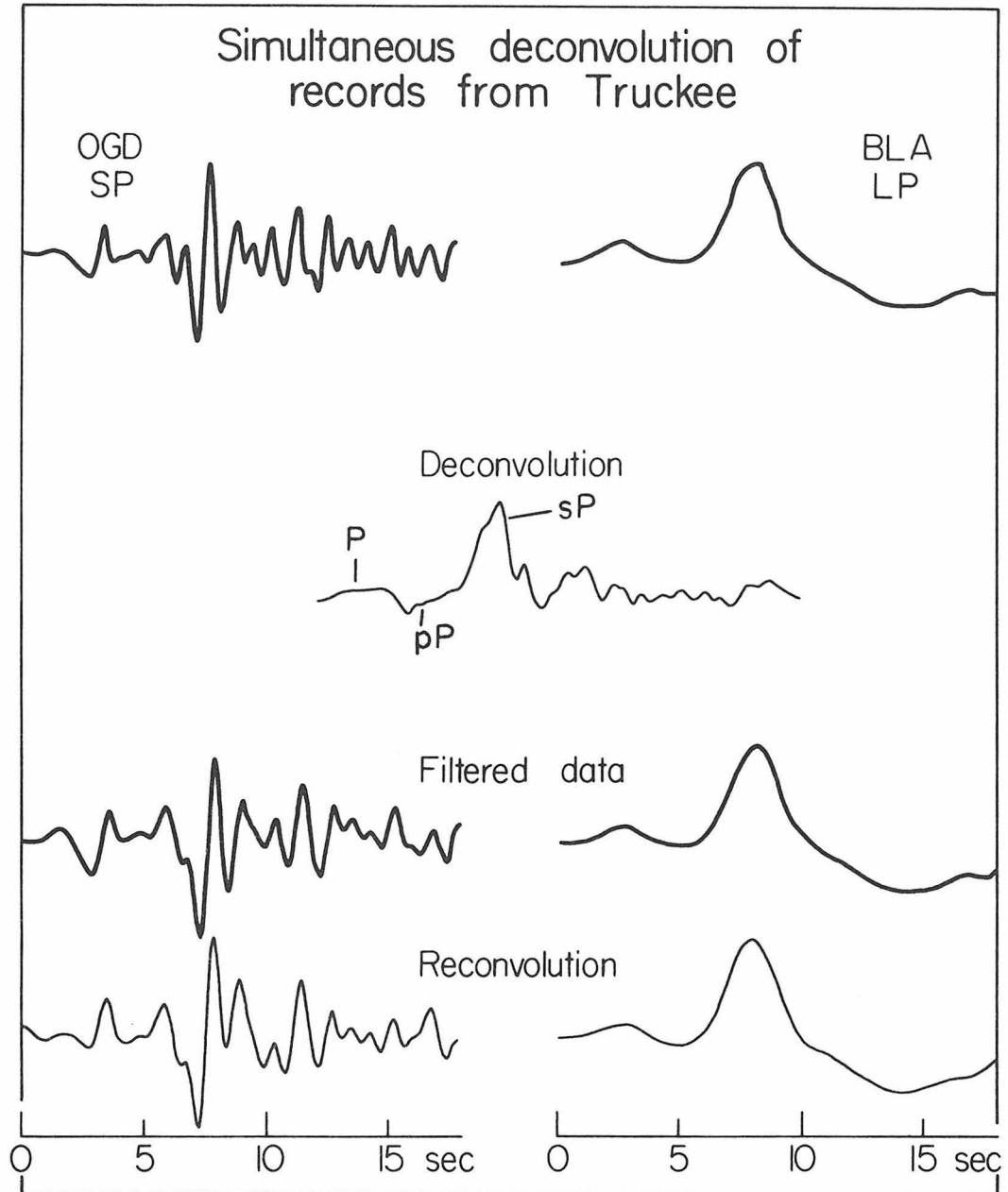
Figure 1.5   The deconvolution result which is shown in the second row
             is a time function which is compatible with both the long
             and short period records of the Truckee earthquake. It was
             obtained by simultaneously deconvolving the top two traces.
             The third row shows the data filtered by the deconvolution
             filter.   The bottom traces are the result of reconvolving
             the deconvolution result with the instruments. If the
             deconvolution result is sufficiently stable, the bottom
             two rows should be the same.

the hypothesis that the area of the first day aftershocking is equal to the area which radiated the body waves is consistent with our current understanding of the faulting process.

The Borrego Mountain Earthquake:

The Borrego Mountain aftershock sequence was studied both by Allen and Nordquist (1972) and by Hamilton (1972). The former authors in particular reported on the extent of aftershocking in the first 22 hours after the main shock. The zone was bounded along the strike direction by a magnitude 4.7 shock on the N.W. end and by a magnitude 4.3 shock fifty kilometers away on the S.E. end. These are among the larger events of the aftershock sequence. The located depths of the first day shocks ranged between 1 and 10 kilometers, but these determinations were not too reliable. Better located shocks later in the sequence occurred at depths as low as 12 km so this will be used as the lower limit of the aftershock zone.

A schematic representation of the aftershock zone and the theoretical fault models to be considered first is shown on the right in Figure 1.6. Points I and II represent the epicentral locations of the two events which bound the aftershock zone. The rectangle is the boundary of the first day aftershock zone on the steeply dipping fault plane. Burdick and Mellman (1976) considered theoretical pulses from fault models of the Borrego Mountain earthquake which extended to depths of 16 km. As shown by Figure 1.6, this is well below the aftershock zone. The first model to be considered here is model A. As shown in Figure 1.6, it is an elliptical failure surface which covers the aftershock zone.
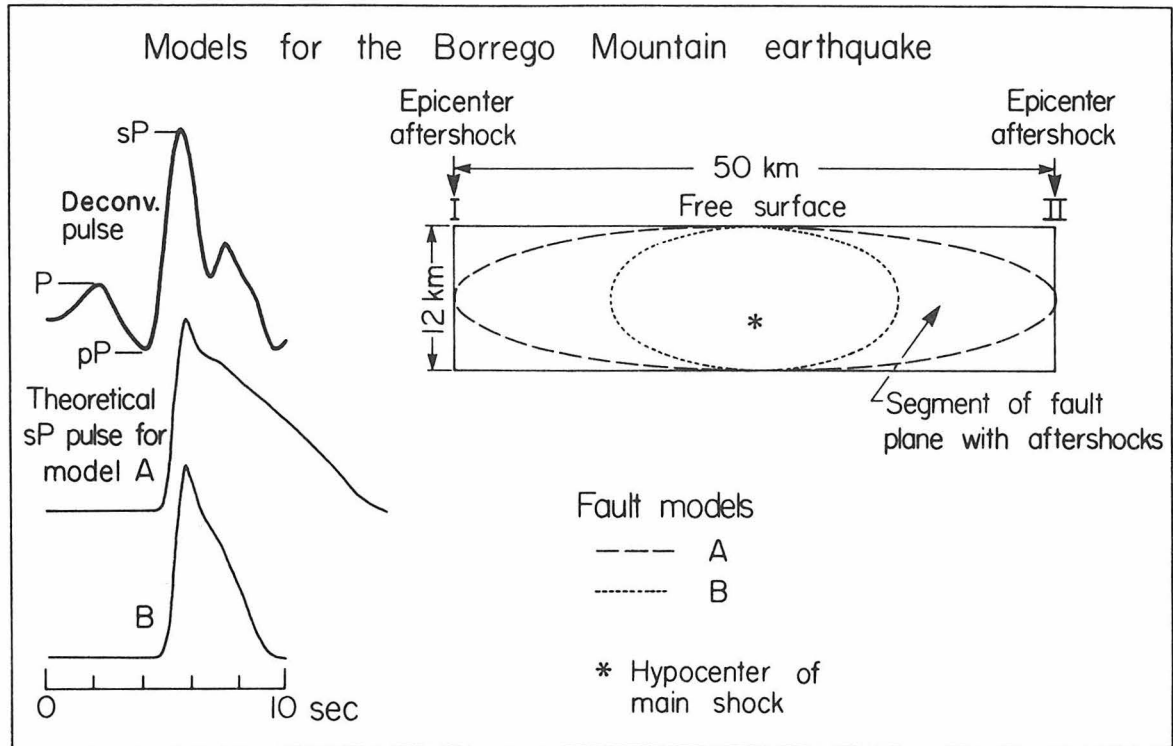
Figure 1.6   The figure compares theoretical pulses for the fault
              models on the right to the observed pulse. The
              rectangle represents the area on the fault plane on
              which the aftershocks occurred. Model A covers the
              entire fault plane but does not match the observed
              pulse. A model like model B which does explain the
              observed pulse **shape** must be smaller than the after-
              shock zone.

The theoretical sP pulse computed from this model is shown under the observed sP pulse on the left of the figure. We assume that since the P and pP pulses are so small, they have a negligible effect on the observed sP pulse. A comparison of the two pulses shows that the theoretical pulse for model A is unquestionably too long in duration.

Model B is an elliptical model which covers only about half of the aftershock zone. The theoretical pulse for this model, which is shown on the bottom left of Figure 1.6, compares much more favorably with the observed. The precise dimensions of the two fault models are given in Table 1.1. The strong implication of this numerical experiment is that the Borrego Mountain earthquake is one case where estimating the body wave fault area from the aftershock zone would not have worked well.

There were two assumptions made in the development of the formalism for computing the theoretical pulses which should be discussed in the light of these results. The first is the choice of the rupture velocity as .8β. If the actual average rupture speed was chosen to be closer to β, it would obviously have caused a shorter time function for a given fault model. However, the theoretical pulse for model A is only 1.5 seconds shorter if the rupture velocity is set equal to β. Therefore, the result of this section would be unchanged. If the rupture velocity were chosen to be less than .8β the evidence that the failure zone was smaller than the aftershock zone would be even stronger. The second detail in the theoretical formalism which bears on these results is the assumption that the effects of the finite dislocation time of the two sides of the fault can be neglected. If it were not neglected, a boxcar pulse of the duration of the average dislocation time would be convolved with the

TABLE 1.1   DIMENSIONS OF FAULT MODELS

Event	Fault Model	Horizontal Axis (Km)	Vertical Axis (Km)	Area Km^2
Borrego	A	25.0	6.0	471
	B	12.0	6.0	226
Oroville	A	5.0	5.0	78.5
	B	3.75	2.0	23.6
	C	7.5	7.5	177.
Truckee	A	5.0	6.0	94.2
	B	4.0	3.0	37.7
	C	7.5	7.5	177.0

theoretical pulses in Figure 1.6. The duration of the pulses would be increased so the pulse for model A would still be too long and model B would have to be even smaller to satisfy the observation. The basic result of this test would again be the same.

A second observation of some interest can be made from this model experiment by computing what the displacement on the fault must have been. The seismic moment of the Borrego Mountain event was determined to be 11.2 X 10^{25} dyne-cm from the body wave amplitudes by Burdick and Mellman (1976). The surface waves indicate a moment of 30. X 10^{25} dyne-cm. (Rhett Butler, personal communication). The seismic moment M_o is given by

$$M_O = \mu \bar{D} \ A \tag{9}$$

where A is the fault area, μ is the rigidity and $\bar{D}$ the average displacement. Using the area of model B and assuming μ is about 3 X 10^{11} dyne/cm^2 means that $\bar{D}$ must have been of the order of 160 cm using the body wave moment or even larger using the surface wave moment. The maximum observed surface displacement was 38 cm and the surface offset was less than that (Clark, 1972). This implies that the displacement at depth must have been even larger than the average displacement and that the displacements actually did become smaller as the fault propagated to the surface. This feature has already been built into the theoretical model through equation 8, but it is very interesting that the phenomenon actually does occur in the earth.

The Oroville Earthquake:

The extent of the aftershock zone of the Oroville shock was determined by both Lahr, et al. (1976) and Morrison, et al. (1976). The best data on the first day shocking came from the latter study. The strike of the fault was directly north and the first day shocks were all located between $30°25'$ and $39°30'$ north latitude. This is a distance of about 10 km. The depth of the shocks ranged between 3 and 9 km, but again the resolution of the depth was not good for the first day. For the vertical extent of the aftershock zone, we will use the range from 0 to 10 kilometers.

The aftershock zone and fault models to be considered are illustrated on the right of Figure 1.7 in the same manner as before. Model A is again the model which covers the aftershock zone. The theoretical pulse is compared to the observed pulse on the left of the figure. In this observed pulse, no single phase is dominant as the sP phase was for the Borrego Mountain waveform. Therefore, it is necessary to compute theoretical pulses for all three of the major phases and to add them up at the right weights and lag times in order to compare the model with the data. In contrast to the Borrego Mountain result, the pulse from the fault model which covers the Oroville aftershock zone appears to be compatible with the observed pulse. The relative peak heights of the P and pP + sP arrivals do not agree by about 25%, but this is not too serious given the uncertainties in reflection coefficients and fault plane solution.

To explore this result further we will consider two other fault models. The choice of the dimensions of the first of these models,
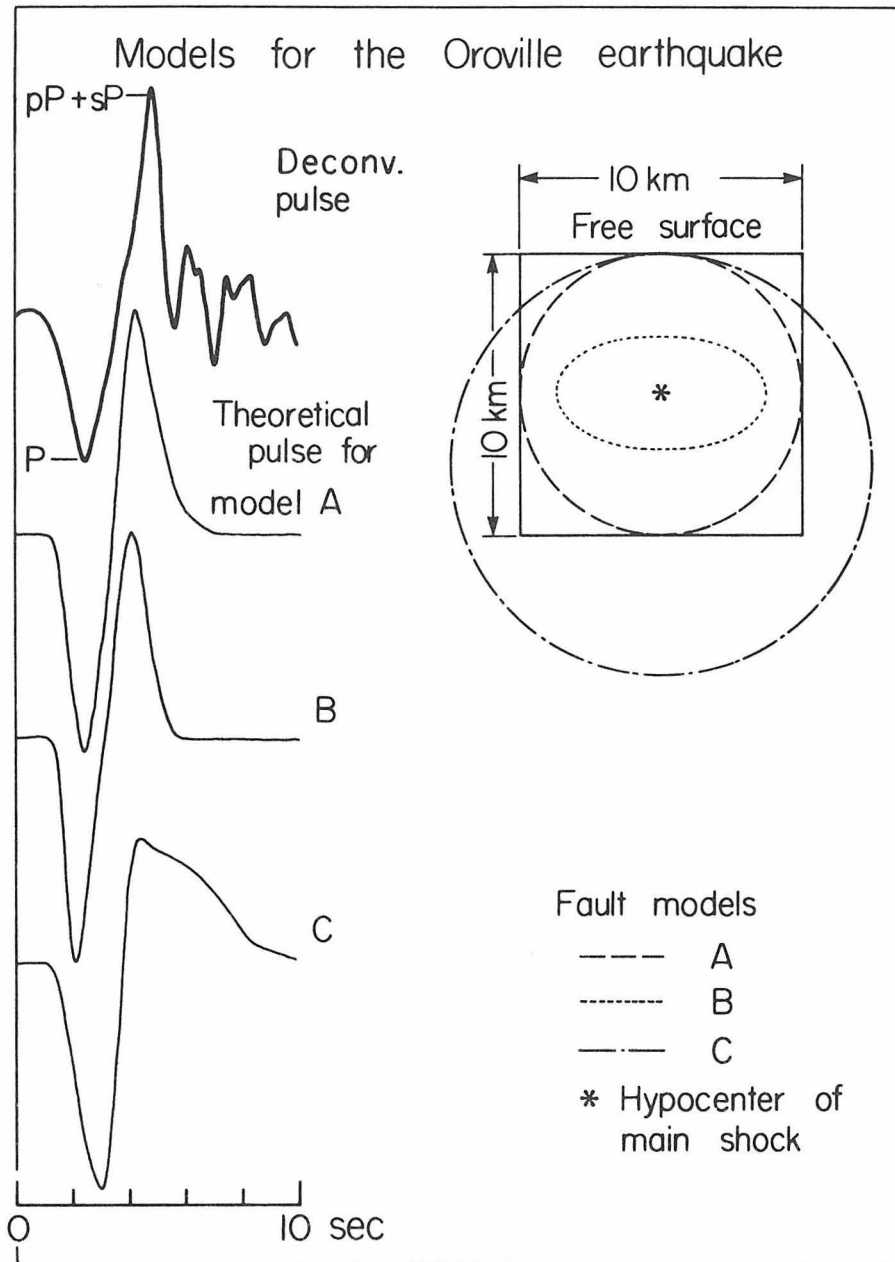
Figure 1.7   The figure compares theoretical pulses for the fault
             models on the right to the observed pulse. The rectangle
             represents the area on the fault plane on which the after-
             shocks occurred. Models A and B have fault areas less
             than or equal to the aftershock area while model C has
             a larger area. Models of the A or B type are acceptable,
             but models of the C type are not.

which is model B in Figure 1.7, is motivated by an observation of Lahr
et al. (1976) that in the middle of the Oroville aftershock zone is a
region which had virtually no aftershocks for the first month. The
size and location are roughly represented by model B. As shown on
the left of the figure, the pulse from model B agrees with the observed
as well as model A. The final fault model to be considered is model C
in Figure 1.7. This model was designed simply to be somewhat larger
than the aftershock zone. The theoretical pulse for model C on the
bottom left of the figure very clearly does not fit the observed. The
dimensions of models A, B and C are given in Table 1.1.

This comparison between theoretical and observed pulses shows that
a group of fault models will satisfy the available data. The acceptable
models range from models of faults significantly smaller than the after-
shock zone to faults as large as the zone. Models of faults which are
larger than the aftershock zone are not acceptable. Some additional
insight into which are the most reasonable fault models may again come
from a comparison of the observed and computed displacements.

The fracture zone observed by Clark et al. (1976) was only 3.8 km
long and the observed slip was only 5.5 cm. This makes it difficult
to believe that the fracture is the surface trace of a fault like model
A in Figure 1.7. The length of the fracture is too short, and the size
of the displacement is difficult to explain in light of the following
calculation. The surface wave moment of the Oroville quake was reported
by Hart, Butler and Kanamori (1977) to be 1.9×10^{25} dyne-cm, and the
body wave moment of the event was reported by Langston and Butler (1976)
to be $.57 \times 10^{25}$ dyne-cm. Some speculations as to why the body and

surface wave moments do not agree were given in each of the two reports.
If the body wave moment was correct and the rupture surface was as large
as the aftershock zone, then from equation 9 and the dimensions of model
A the average displacement $\overline{D}$ must have been 24 cm. If the surface wave
moment is correct, and it should be more accurate for computing static
displacements, the average fault displacement must have been 81 cm. If
model B is assumed, the computed displacements become 81 and 268 cm for
the body and surface wave moments respectively. In all cases, the com-
puted average displacement is much larger than the observed surface
offsets. A geodetic survey reported by Clark et al. (1976) showed 18
cm of vertical movement between benchmarks on opposite sides of the fault.
This value is reasonably close to the computed displacement for model A
if the body wave moment is assumed. However, the geodetic data do
not exclude a B type model where the displacements were longer than 18
cm at some depth in the earth. If model A is a better representation of
what actually happened during the earthquake, then it is a necessary part
of the model that the displacement decrease as the rupture propagates
upward. Otherwise more extensive surface faulting would have been
observed. If model B is a better representation of the fault, then the
rupture stopped at depth and the observed surface faulting was secondary
in nature.

The Truckee Earthquake:

The moment for the Truckee earthquake was determined by Tsai and Aki
(1970) to be .83 X 10^{25} dyne-cm. The body waves give a very similar
value of .6x10^{25} dyne-cm (Appendix 3). The aftershock sequence was
studied by Greensfelder (1968) and the observable surface fractures

by Kachadoorian et al. (1967). The total aftershock zone was about 10
km long and 12 km deep. Since the station coverage was poor until
two days after the event, there is no way to estimate the first day
aftershock zone. Therefore, we must assume that it was not too different
from the total aftershock zone. The surface manifestations of faulting
were a very discontinuous line of pressure ridges, mole tracks and lurch
cracks in unconsolidated alluvium along a line about 10 km long. There
were no measured offsets. The three theoretical models which will be
considered are similar to the ones considered for the Oroville event.
The first model, which is again called model A, covers the entire after-
shock zone. Since the sP phase is the predominant one, as it was for
the Borrego event, it will be the only phase which is computed. As shown
in Figure 1.8, the theoretical sP pulse for model A fits the observed.
Model B was chosen to represent a small region on the fault at depth
which would still be compatible with the observations. As shown in
Figure 1.8, the pulse from model B also appears to fit reasonably well.
Model C was chosen to represent a failure surface which extends some-
what beyond the aftershock zone. A comparison between the observed and
computed pulses shows that a model of this sort is probably not acceptable.
The dimensions of the models are given in Table 1.1. From the observed
moments we compute displacements of 29 cm and 21 cm assuming model A.
The smaller fault model, model B, gives displacements of 73 cm and 53 cm.
When these values are compared with the negligible observed surface
displacements, it appears again that the displacement must have been
greater at depth than at the surface. Just as for the Oroville earth-
quake, a range of models will fit the pulse shape. The fault area may
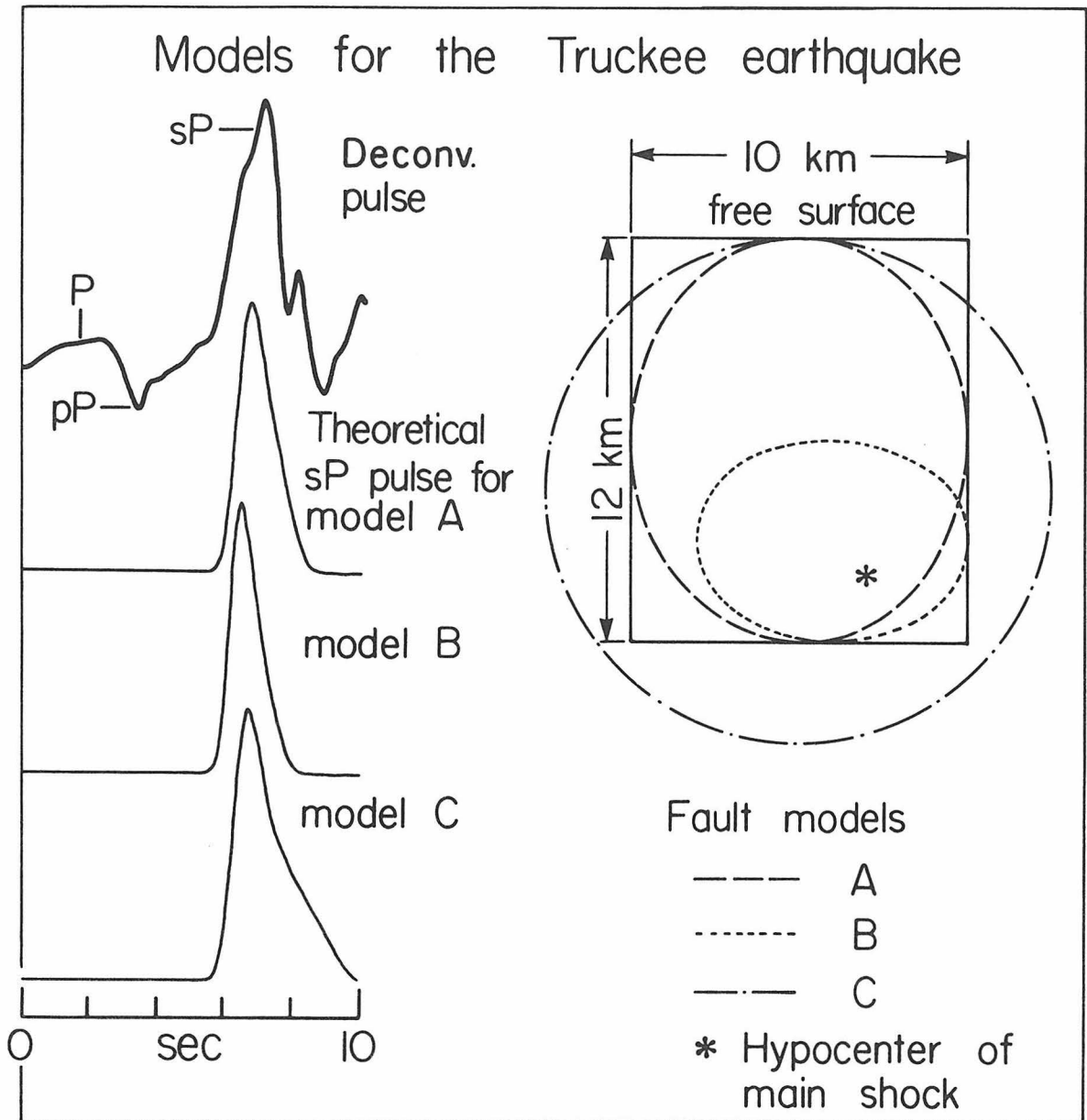
Figure 1.8   The figure compares theoretical pulses for the fault
models on the right to the observed pulse. The rectangle
represents the area on the fault plane on which the after-
shocks occurred. Models A and B have fault areas less
than or equal to the aftershock area while model C has
a larger area. Models of the A or B type are acceptable,
but models of the C type are not.

be less than or equal to the aftershock area. However, if the fault did propagate all the way to the free surface, the displacement must have decreased as it did so.

DISCUSSION

For the 3 seismic events which have been examined, the hypothesis that the aftershock zone and the body wave fault area would be the same proved to be possibly correct in two cases but definitely incorrect in the case of Borrego Mountain. The observed body wave pulses were consistent in all three cases with the fault area being significantly smaller than the aftershock zone. In order to decide whether this latter possibility is reasonable, it is necessary to decide how the termination of a rupture front is related to aftershocking. Unfortunately, since this relationship is poorly understood, only a few general comments can be made.

As a fault expands to its final size the rupture front must terminate in its lateral propagation, its upward propagation and its downward propagation. It may do so for different reasons in each instance. It must be presumed that a fault stops expanding laterally when the rupture front encounters stronger material or when the prestress field decays. Chinnery (1963, 1966 a, b) has shown that the effects of faulting can extend significantly beyond the lateral termination point of the fracture. There are large perturbations in the stress field and very probably secondary fractures past the end of the fault. It is not un-reasonable to assume that these stress changes induce aftershocking for some distance beyond the rupture zone. In the case of the Borrego

Mountain earthquake, it appears that aftershocks occurred at least one half fault length past the rupture terminus (see Figure 1.6). Hamilton (1972) has already suggested that some Borrego Mountain aftershocks were induced by changes in the stress field rather than by the main shock rupture. In the Oroville study, the dimensions of fault model B were chosen to match the no aftershock zone. This amounted to testing the interesting hypothesis that aftershocks occurred exclusively beyond the limits of the failure zone (see Figure 1.7).

The results of this study have shed some interesting new light on the way a fracture behaves as it propagates up to the free surface. The calculated average displacements for all fault models which fit the observed pulses are compared with observed surface offset data in Table 1.2. In every case, the calculated average displacement for the fault is larger than the largest observed surface offset. This implies that the displacements on the fault began to decrease as the rupture propagated upward. The surface offsets associated with the Borrego Mountain earthquake were continuous and relatively large in size. They most probably resulted from the intersection of the main rupture with the free surface. The surface fractures associated with the other two events were much smaller and may have been secondary in nature. The rupture may have actually ended at some depth as suggested by the B models in Figures 1.7 and 1.8.

The observation that in some cases the displacements at depth are larger than the observed surface offsets is not unique to this study. A similar result was found by Alewine (1974) for the San Fernando earthquake, Savage and Hastie (1966) for the 1959 Hebgen lake and 1964 Alaskan earthquakes and Aki (1968) for the Parkfield earthquake. Aki suggested

TABLE 1.2   FAULT DISPLACEMENTS

| Event | Model | M_0 dyne-cm | | Fault Area (km^2) | Displacement (cm) | | |
		Body wave	Surface Wave		Body Wave	Surface Wave	Observed
Borrego	B	11.2×10^{25}	$30. \times 10^{25}$	226	165	442	38
Oroville	A	$.57 \times 10^{25}$	1.9×10^{25}	78.5	24	81	5
	B			23.6	81	268	
Truckee	A	$.6 \times 10^{25}$	$.83 \times 10^{25}$	94.2	21	29	
	B			37.7	53	73	

that the displacement on the fault decreases by as much as an order
of magnitude within 100 meters or so of the surface. A more common
suggestion is that the displacement is absorbed over a greater thickness
of surface layering and sometimes appears as creep movement after the
event. (Burford, 1972; Smith and Wyss, 1968). Scholz, Wyss and Smith
(1969) propose a model in which motion occurs aseismically over a 4 km
thick surface layer.

The assumption that a failure zone propagates down only as low as
the deepest aftershocks is used very commonly. However, this assumption
does not hold up well under careful examination. A very common feature
of mechanical models of faulting is that shocks die off with depth
because the failure properties of the material change from stick slip
to stable sliding. (Scholz, Wyss and Smith, 1969; Rodgers and Chinnery
1963; Lachenbruch and Sass, 1973.) The effective failure zone could
easily penetrate down into the stable sliding zone even though the
aftershocks do not. Unlike the previously discussed mechanisms, this is
a mechanism by which the failure zone could exceed the aftershock zone.
The results of this study tend to rule out smooth propagation of the
ruptures below the aftershock zones. Otherwise, the C models in
Figure 1.7 and 1.8 would have fit the observed pulses better. Hart,
Butler and Kanamori (1976) have suggested that the Oroville fault
propagated below the aftershock zone. They also suggested that the
displacement below 10 km occurred slowly enough, so that it would only
affect the long period surface waves and not the body waves. This
would explain why the moment calculated from the surface waves was three
times larger than the one calculated from the body waves. Slow
deformation off the ends of the fault could explain the similar discrepancy

in the moments for the Borrego Mountain event and also the large lateral extent of the aftershock zone. If these explanations are correct then the physical process of failure must be varying along the fault. The average stress drop calculated for the entire fault would then be a poor indicator of the breaking strength of the rock in the region which radiated the body waves. The average fault displacement for the whole fault would likewise be a poor indicator of the magnitude of the displacements in this high strength region.

The original hypothesis which was the subject of the numerical tests and this discussion has not been strongly supported by the results. The aftershock zone is not always a good indicator of the size of the failure zone. As we have seen, the lack of correlation between the two zones could be explained by a variety of mechanisms. This implies that calculations of such parameters as stress drop using the assumption that the aftershock zone equals the failure zone need careful reevaluation.

One of the most compelling reasons to believe that the stress drop of earthquakes is relatively low comes from the study of the moment-area relationship of very large earthquakes by Kanamori and Anderson (1975). The relationship between these quantities indicates that most great earthquakes have an overall stress drop of about 30 bars. However, it is becoming apparent from studies of the body waves of large events that these earthquakes are often made up of several distinct component events (Kanamori and Stewart, 1976; Stewart, Butler and Kanamori, 1976). These component events are presumed to come from regions of high strength on the fault which are sometimes called asperities. It is not un-reasonable to suggest that a single component shock will be like one of

the intermediate earthquakes studied here. The evidence that those events have large displacements at depth and possibly small fault areas indicates that they may have high stress drops. Thus, the stress drop in the region of a component shock of a large earthquake may be much higher than the overall average for the shock. This has important implications for earthquake prediction. The important thing to look for in an area prone to large earthquakes may be a single asperity of less than 10 km diameter which is at a very high prestress level.

CONCLUSIONS

The simultaneous use of the information from the long and short period records has permitted good broad-band estimates of the source pulses of the three shallow earthquakes. Modeling these pulses has led to two important conclusions. The first is that the size of the aftershock zone is not always a good estimate of the fault area. The second is that offsets observed in surface faulting tend to be significantly smaller than the average fault displacements computed from seismic data. This requires some mechanism which causes the displacement on the fault to decrease as the fracture propagates upward.

CHAPTER 2

t* FOR S WAVES WITH A CONTINENTAL RAYPATH

INTRODUCTION

The attenuation rate of body waves is generally parameterized either by the average quality factor along the raypath, Q_{av}, or by the quantity t*. This is defined as the ratio of the travel time, T, to the average quality factor.

$$t* = T/Q_{av} \qquad (1)$$

t* is given a subscript α for P waves or β for S waves. Since body wave travel times are well known, the two parameterizations are interchangeable. Most previous measurements of $t*_\alpha$ for teleseismic body waves have yielded values around 1. second and those of $t*_\beta$ around 4. seconds (Anderson and Hart, 1977; Marshall et al., 1975). The values appear to be roughly independent of epicentral distance for $20° < \Delta < 80°$, but they do depend on source depth.

A very common method for determining Q_{av} has been to measure the attenuation of successive multiples of the ScS phase on long period records (Kovach and Anderson, 1964; Sato and Espinoza, 1967; Yoshida and Tsujiura, 1975; Jordan and Sipkin, 1977). Other methods have involved measuring the spectral content of direct P and S waves from long period seismometers (Solomon and Toksöz, 1970; Mikumo and Kurita, 1968; Teng, 1968). A few studies have used P waves recorded on short period instruments (Kanamori, 1967a; Frasier and Filson, 1972) and fewer still have used short period S waves (Marshall et al., 1975; Kanamori, 1967b; Choudhury and Dorel, 1973). Marshall et al. (1975) pointed out that the short period teleseismic S waves merited much closer examination because the effect of anelastic attenuation on them

is overwhelming. Since the effect can be easily discerned in the
short period S wave data, it can be reliably measured. The purpose
of this report is to present some new measurements of t^*_β. They have
been determined from teleseismic S waves recorded on both the WWSSN
short period and long period instruments. The short and long period
P waves have been used to constrain the initial source radiation
in the period range spanned by the two instruments. Theoretical
source models and a theoretical relationship between t^*_α and t^*_β
have been used to relate the observed P waves to the observed S waves.

t* FOR A SURFACE FOCUS EVENT

The S waves from the 4/9/68 Borrego Mountain earthquake as
recorded at WWSSN stations in the northeastern U. S. are especially
well suited for determining t^*_β. The records are low noise and the
stations are oriented so the NS component is pure SH. The distance
range is between 30° and 40°, so the effects of the velocity structure
of the mantle on the direct arrivals are negligible. Most importantly,
the effects of attenuation are very dramatic and can be seen easily
in the records.

The Data Set:

Figure 2.1 shows the P and SH waveforms from State College,
Pennsylvania (SCP, Δ= 31.3°). The long period instruments have a
gain of 1.5K. At this setting, the P wave is of moderate size. The
long period S is large but still on scale. The short period in-
struments are set at 50K gain. At this setting, the short period
P is slightly larger than the long period P. However, the short
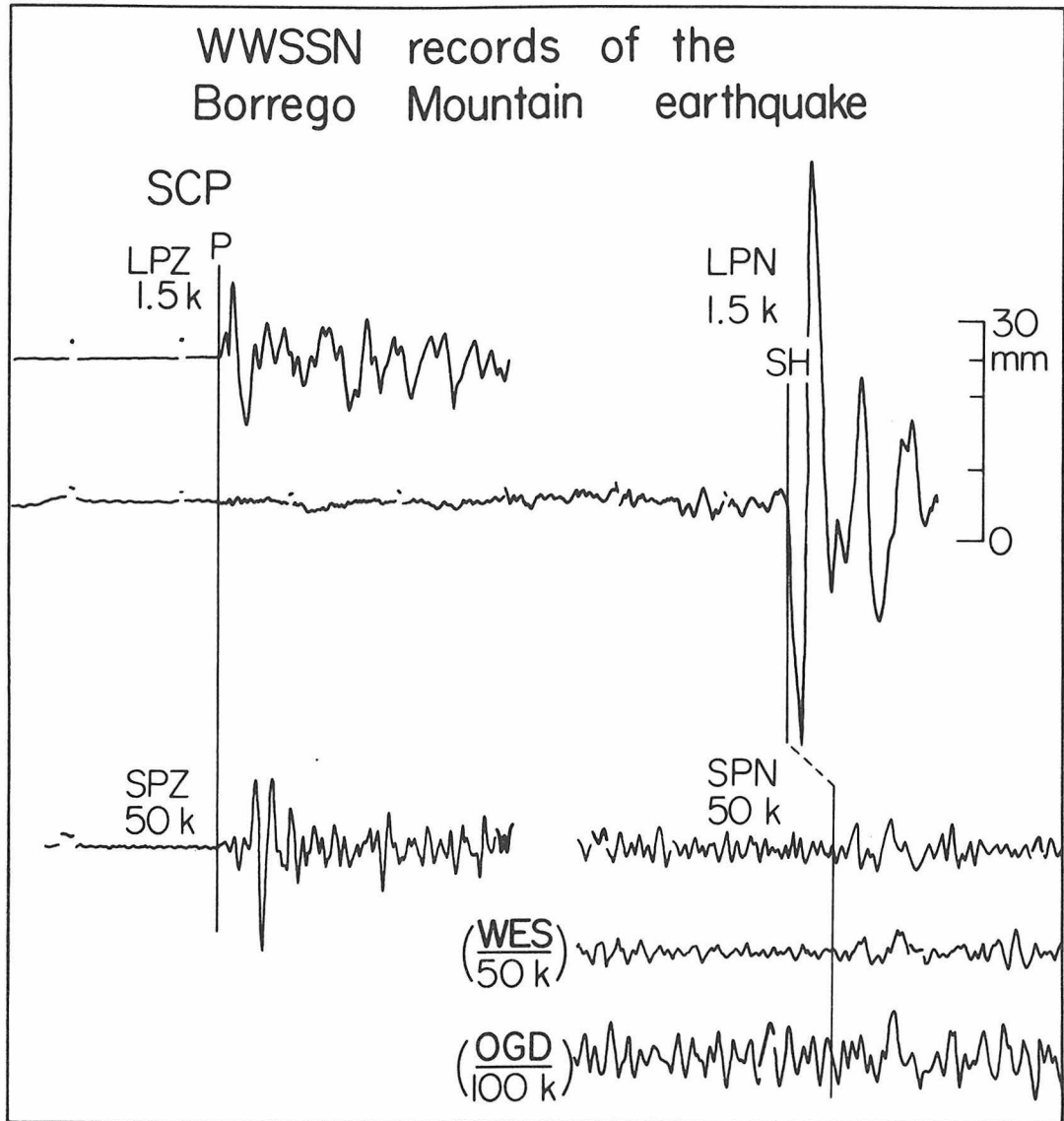
Figure 2.1   The figure shows the long and short period records of the
             Borrego Mountain earthquake at SCP. The P waves are simple
             and clear. The long period N component is very nearly pure
             SH. The short period S waves are very small because they
             have been severely attenuated.

period S barely emerges from the background noise even though the long period S is very much larger than the long period P. This is because the short period S energy has been attenuated much more heavily than the P.

Also shown in Figure 2.1 are the short period SH records from Weston, Massachusetts (WES, $\Delta=36.3°$) and Ogdensburg, New Jersey (OGD, $\Delta=33.4°$). The short and long period records from these stations have also been used in this study. Like the short period SCP S wave, the WES and OGD short period S waves are very small. The signal to noise ratio at SCP and WES is about 2/1 and at OGD only about 1/1. Nonetheless, it is possible to make a meaningful measurement of t^*_β from only a rough estimate of the amplitudes of these short period S waves.

We can be certain at the outset that the evidence for heavy attenuation of the S waves which is illustrated by Figure 2.1 is not a source effect. As we shall show, the P waveform is dominated by the sP arrival and the S waveform by the sS arrival. This means that the strongest arrivals in the P and S wave codas must have had nearly identical radiation from the source. This knowledge of the relative strengths of the surface phases illustrates the final reason for using the S waves from the Borrego Mountain event. The source has been studied extensively and a very accurate source model is available (see Appendix 3). This model makes it possible to separate the effects of attenuation from the effects of the source.

Figure 2.2 shows all of the data to be used in determining t^*_β on an expanded time scale. Synthetics for the long period records are
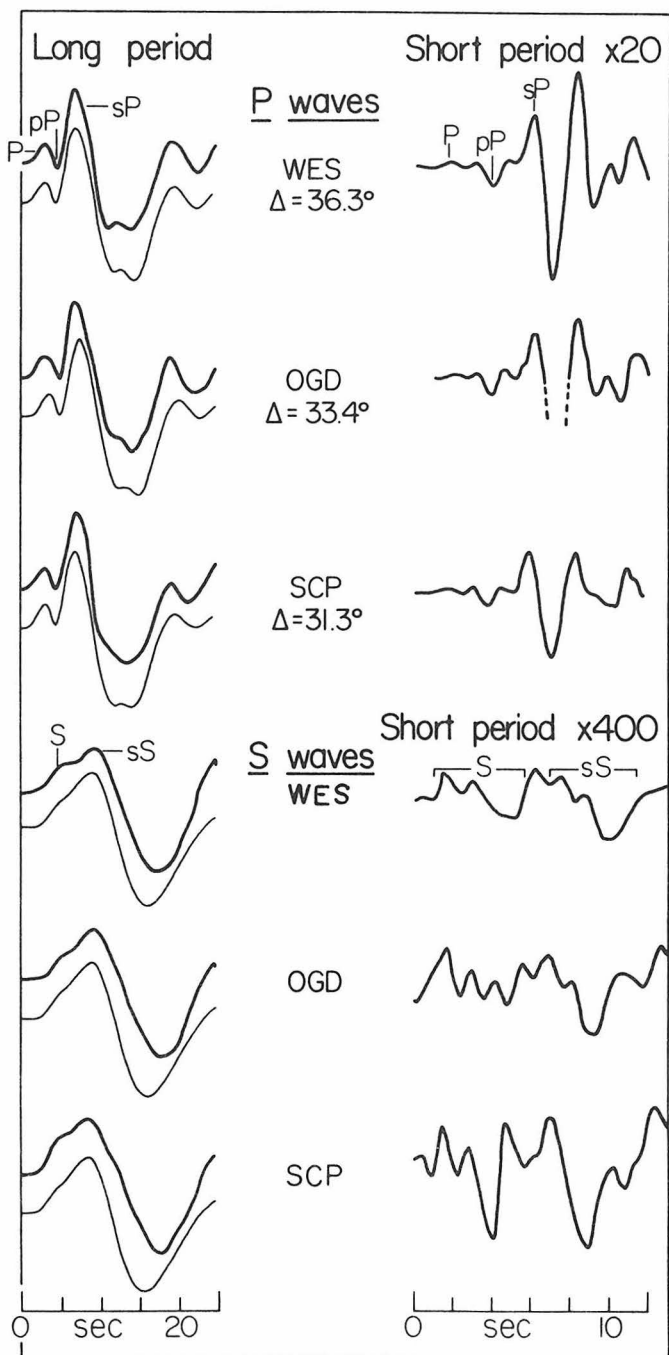
Figure 2.2   The figure shows the long and short period records to be
used in the study. All long period records are normalized
to 1. The corresponding short period P records are
magnified by a factor of 20 with respect to the long, and
the short period S records by a factor of 400. The short
period S waves are much smaller than the P because they
have been more heavily attenuated.

compared with the data to show how well the source model predicts the ground motion at these particular stations. From the theoretical source model, we know that the P and pP appear as small precursors on the long period P waveform. The dominant arrival is the sP phase. The three arrivals are marked on the WES record in Figure 2.2. The sS phase is about twice the size of the S phase. The arrivals are marked on the WES SH waveform in the figure. It is important to note that the synthetic seismograms in Figure 2.2 and in Appendix 3 were computed for a point source. This means that the effects of fault directivity were ignored and a single source pulse was used for all phases. The fact that synthetics computed by neglecting the effects of directivity match all available long period body wave data will play a key role in our determination of t^*_β. All of the long period records have been normalized to unit amplitude. The S waves have been reversed in sign so that all of the records would have the same polarity. The short period P records have been magnified 20 times with respect to the corresponding long period records. The internal consistency between the short period P records indicates that each of the three stations is relatively transparent. The short period S records are magnified 400 times with respect to the long period S records. The waveforms are much less consistent because the signal to noise ratio is so much smaller. In Figure 2.2, the short period sP and sS phases appear to be roughly the same size. Since the short period P waveforms are magnified 20 times and the short period S waveforms 400 times, the short period to long period ratio of the sS phase is at least 20 times smaller than the sP ratio. The sS and sP

phases must have left the source with very nearly the same frequency content. But when the waves arrived at the receiver, the short period energy which traveled in the shear mode was attenuated much more than the short period energy which traveled in the compressional mode. The effects of anelasticity can be easily seen in the records and reliably measured.

It may seem that it would have been preferable to use a larger source event than the Borrego Mountain earthquake in order to increase the amplitude of the short period S waves. However, this is not the case. To measure attenuation as a function of frequency, it is also necessary to have good estimates of the long period S amplitudes. The SCP SH record at 1.5K gain is about half the possible amplitude scale. The WES and OGD SH records are as large as they can be without going off scale. The majority of WWSSN long period instruments are run at either 1.5 or 3.K gain. In those instances where the long period level is reduced, the short period gain is generally also reduced. Therefore, if a larger earthquake were used, either the long period records would be off scale or the short period records would still be very small. Also, the sources of events larger than Borrego Mountain are almost always complex multiple events which are very difficult to model. All in all, the data set to be used here is as good as any which might be found for determining t^*_β from direct S waves.

Data Analysis:

There are two major difficulties involved in extracting the value of t^*_β from the data set. The first is that the interaction of the

direct phase with the surface phases plays a dominant role in determining the shapes of the long period P and S waveforms. This can be most easily compensated for by computing time domain synthetics rather than trying to fit Fourier spectra. The second difficulty with the data is the poor signal to noise ratio of the short period S waves. A simple measurement of the maximum trace amplitude would be an un-reliable indicator of the size of the wave. A more sophisticated measurement of the signal strength is required. The parameter which will be used to quantify the amplitudes of the S records will be designated as r_s or the S wave power ratio. It is defined as

$$r_s = \int_c^T [SP(t) \cdot W(t)]^2 \, dt \Big/ \int_o^T [LP(t) \cdot W(t)]^2 \, dt \qquad (2)$$

SP(t) and LP(t) are the long and short period records normalized to unit gain and W(t) is a trapezoidal time window. T, the total length of the window is 14 seconds. The trapezoid has a two second rise time, a ten second level time and a two second falloff time. The window is positioned so that it begins two seconds before the estimated arrival time. In time domain, r_s is simply the ratio of the average squared amplitudes of the short and long period signals. In frequency domain, the reasons for choosing this particular amplitude measure are more apparent. From Parseval's theorem, we know that the quantity in the numerator of equation two is just the power in the frequency band of the short period instrument, providing that W(t) is much longer than the instrument response time. The quantity in the denominator is the power in the lower frequency band of the long period instrument. The time window is long enough so that it will not have a strong effect. The quantity r_s is then the ratio of the power in the

two frequency bands defined by the two WWSSN instruments. It is a rough but stable estimate of the spectral content of the wave which uses the natural characteristics of the WWSSN recording package to best advantage. r_s depends only on the spectrum of the ground motion. All scaling effects such as the source moment and geometrical spreading are divided out by taking the short to long period power ratio. The values of r_s measured from the three SH records shown in Figure 2.2 were $(.23 \pm .07) \times 10^{-5}$ for WES, $(.25 \pm .14) \times 10^{-5}$ for OGD and $(.38 \pm .17) \times 10^{-5}$ for SCP. The error estimates are just the average power in an equivalent segment of background noise. They were found by measuring the power in the 60 seconds of leakover P coda immediately preceding the SH wave and dividing the value by 5.

Calculated Values of r_s:

Theoretical values for the S wave power ratio can be calculated by computing long and short period seismograms and processing them in the same way as the data. If the theoretical waveforms are computed for a range of t_β^*'s, a smooth curve can be generated in the $t_\beta^* - r_s$ plane. The intersection of this curve with the observed levels of r_s should give the t_β^* value for North America. Unfortunately, there is a major ambiguity still to be dealt with. The value of r_s will depend critically on the initial source spectra of the S and sS phases as well as on t_β^*. It is necessary to obtain accurate estimates of the original shapes of these pulses. As was pointed out previously, the assumption that all phases radiated by the source had identical frequency content worked very well in the long period waveform modeling study. Therefore, the approach which will be used here will begin with a determination

of the pulse shape of the sP phase from the P wave records. This
will be accomplished by using the simultaneous long period-short
period deconvolution technique. The synthetic SH waves will then be
calculated by using the deconvolved sP pulse as a model for the S and
sS pulses. In a separate calculation, some theoretical fault models
will be considered to test the validity of this technique. The
procedure for simultaneously deconvolving the attenuation corrected
instrument responses from the short and long period P records was
outlined in Chapter 1. The result for the WES record from the
Borrego Mountain earthquake is illustrated in Figure 1.2. In order
to correct the instruments for attenuation, it is necessary to know
the value of t_{α}^{*}. A relationship exists between t_{α}^{*} and t_{β}^{*} which
effectively reduces the problem back to a single unknown. Anderson,
Ben Menahem and Archambeau (1965) showed that if there are no losses
in pure compression,

$$\frac{Q_{\beta}}{Q_{\alpha}} = \frac{4}{3} \frac{\beta^2}{\alpha^2} \qquad (3)$$

where β and α are the elastic wave velocities. The results of both
that study and the more recent study of Anderson and Hart (1977)
indicate that the compressional losses in the earth are negligible,
so that equation 3 is approximately true. The lack of attenuation of
pure compressional motion merely indicates that shear mechanisms such
as grain boundary sliding dominate the attenuation process. In the
30° to 80° range, the P and S waves have very similar raypaths. If
it is assumed that $\lambda \approx \mu$ along the path then

$$Q_\alpha = \frac{9}{4} Q_\beta \qquad (4)$$

The ratio of the travel times of the direct P and S waves at 33°
is $T_\beta/T_\alpha = 1.80$. Combining these results gives the familiar expression

$$t^*_\beta = 4. \ t^*_\alpha \qquad (5)$$

If a value of t^*_α is assumed, a corresponding estimate of the sP pulse
can be obtained by deconvolution. The synthetic SH waveforms are
then computed using the sP pulse as the source pulse and the t^*_β dictated
by equation 5. The expression for the synthetic seismogram $S(t)$ is

$$S(t) = I(t) * A(t, t^*) * P(t) \qquad (6)$$

I is the appropriate instrument response, * is the convolution operator,
$A(t, t^*)$ is the Futterman (1962) attenuation operator and $P(t)$ is the
source pulse. The source pulse includes the interaction of the basic
pulse shape with the free surface. It is assumed that the earth's
velocity structure has no other significant effect on the seismogram.

Deconvolved sP pulses for a range of assumed values of t^*_α from
.75 to 1.5 are shown on the left of Figure 2.3. The pulses have been
windowed out of the deconvolution results using a square window. This
method should work reasonably well since the sP phase is by far the
largest arrival in the P wave pulse (see Figure 2.2). The sharp
edges of the square window should cause no difficulty since
the S wave attenuation filter is a strong smoothing operator. The
values of the power ratio, R_s, which were determined by using the de-
convolved pulses are plotted as a function of t^*_β in Figure 2.4 (heavy
line). The measured values of the power ratio are shown as horizontal
lines. The theoretical curve intersects the observed levels when
$t^*_\beta = 5.2 \pm .7$ seconds.

The results of the preceding calculation would not be valid if the S and sS phases had significantly different spectral content than the sP phase. This type of effect might have been caused by directivity or focusing of energy by the rupture process. Since the takeoff angles of the sS and sP phases differ by only about 10°, their frequency content could not have differed by any great amount. However, it is possible that the direct S phase, which also falls inside the time window W, was much different in frequency content. The range of possible effects of directivity can be determined by examining some theoretical fault models.

Theoretical Fault Models:

The fault plane of the Borrego Mountain event is steeply dipping, ($\delta = 81°$) and the observing stations are at roughly right angles to the fault plane (az~110°). Therefore, horizontal rupture propagation will not cause large differences in the sP, S and sS phases. The main differences must arise from the vertical rupture propagation. If the fault propagates unilaterally either upward or downward, high frequency energy will be focused in that direction. If the fault propagates bi-laterally, the effects of focusing will be negligible. We will begin by considering the bilateral case.

In the fault model proposed for the Borrego Mountain earthquake by Burdick and Mellman (1976), the rupture is presumed to begin at 8 km depth and propagate outward at a constant rate of 2.8 km/sec (.8β) to a circular boundary of 8 km radius. This brings it upward to the free surface and downward on the fault plane to 16 km. The displacement

distribution is assumed to be the one given by Eshelby (1957), and the dislocation time is presumed to be very small as in the previous chapter. The model is shown schematically at the bottom right of Figure 2.3 as model I. The three theoretical S phases are shown at the top of the figure. As expected, there is little difference between them. The theoretical $r_s - t_\beta^*$ curve computed using the theoretical S and sS pulses is nearly the same as for the previous calculation. It is shown in Figure 2.4 as a light line. This calculation has shown that if faulting was predominantly bilateral in the vertical direction, then the result that t_β^* is about 5.2 seconds is correct. The same would be true if the rupture velocity was very slow or the fault dimension very small.

Fault models which propagate downward to a greater extent than upward generally predict sP phases which are incompatible with the observed arrivals. Also, since the fault appears to have propagated upward to break the surface, this model does not appear to be too reasonable. It is much more likely that if the vertical fracturing was asymmetric, the fault propagated further upward than downward. A model of this type is the one proposed in the preceding chapter. It is shown at the bottom of Figure 2.3 as model II. The failure propagates upward eight kilometers and downward only four kilometers so that energy is focused into the upgoing phases. This can be seen clearly in the theoretical pulses for the model which are also shown in the figure. The theoretical sP and sS pulses are very sharp and match the observed sP. The theoretical S pulse is much lower in amplitude and longer in duration than the upgoing phases. However, if theoretical waveforms are computed using these pulses, they do not match the data. This is
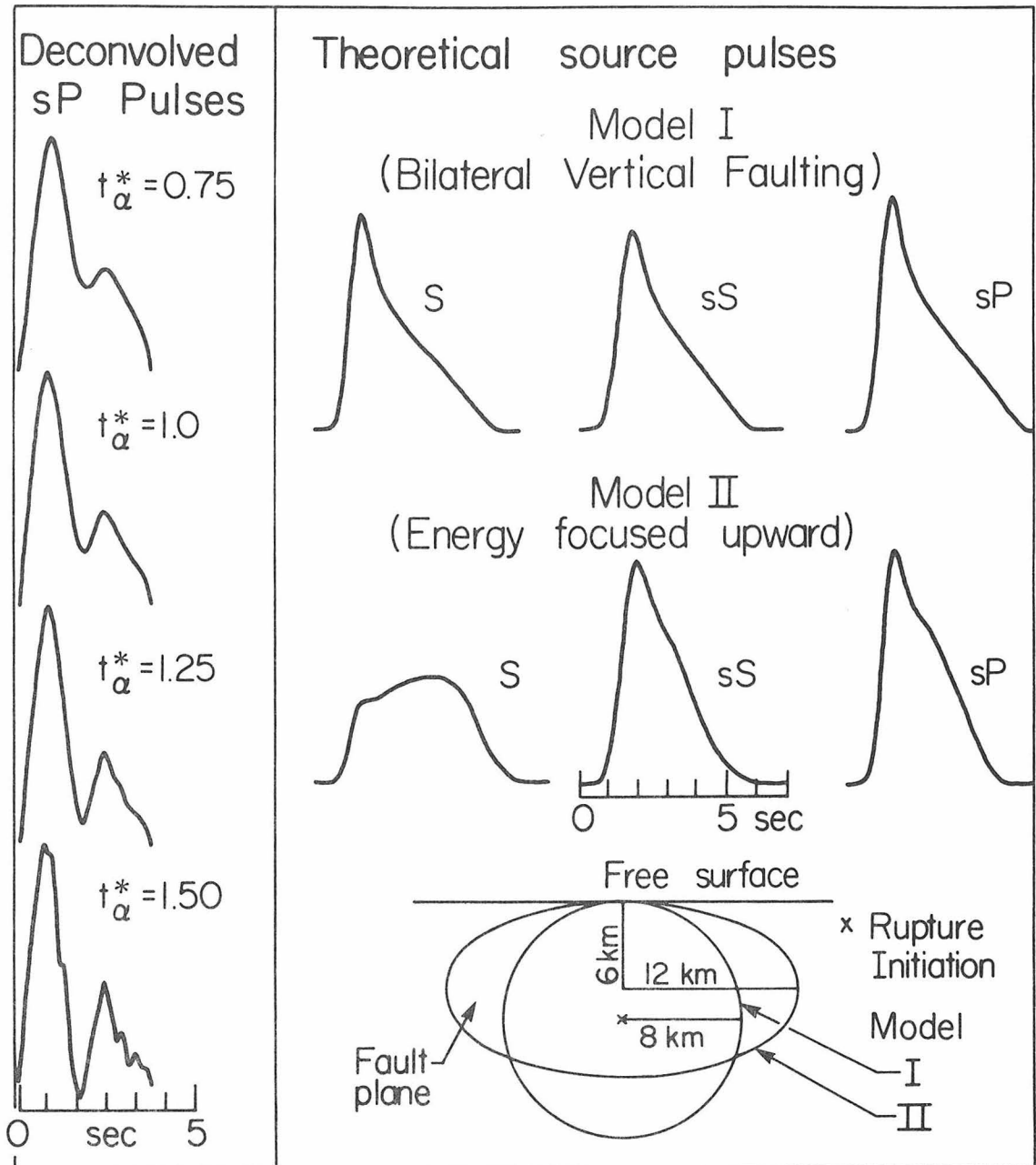
Figure 2.3   The figure shows all of the source pulses used in
computing synthetic S wave seismograms. Those on the
left were deconvolved from the sP phase assuming various
values of t$^*_\alpha$ Those on the right were computed from
the theoretical fault models on the bottom. Either model
fits the observed sP pulse, but model II predicts a very
different shape for the direct S pulse.
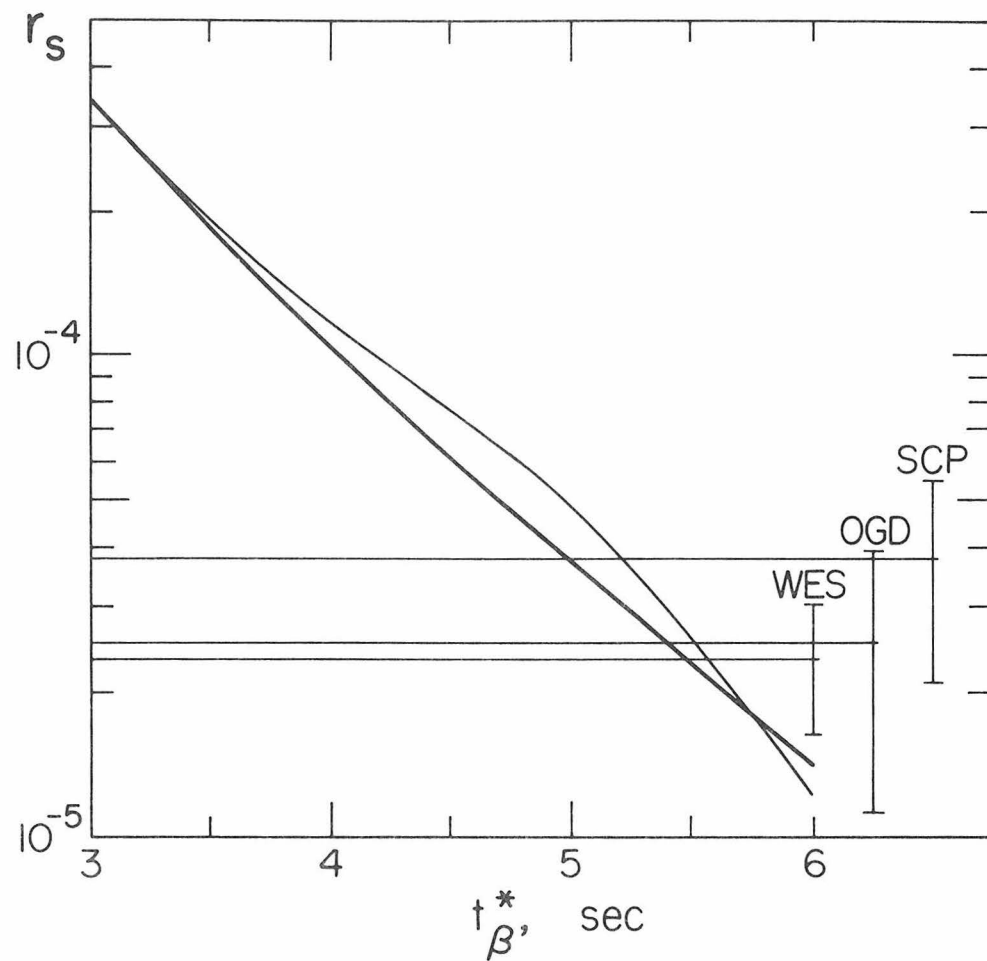
Figure 2.4   The figure shows the intersection of the theoretical
              curves for the S wave power ratio with the observed
              levels. It appears to occur at a $t*_\beta$ value of about
              $5.2 \pm .7$ seconds. The heavy line was computed by using
              the deconvolved sP pulses and the light by using
              theoretical fault model I.

illustrated in Figure 2.5. The seismograms computed using either the
deconvolved sP pulse or the bilateral faulting pulses fit the observed
waveform closely. The correspondence between the observed and computed
S/sS amplitude ratios is very good for the long periods and within
the large uncertainties for the short periods. The seismograms computed
using the theoretical pulses for model II do not.fit the observed S/sS
ratio. The predicted S is too small on both the long and short period records.
The failure of model II to fit the short period S waves is very
significant. Referring back to the short period records in Figure 3.1,
one can see that the upward swing of the S and sS phases emerges clearly
from the noise in the SCP and WES records. The two phases on the short
period record have approximately the relative proportion predicted by
the bilateral faulting model. If vertical directivity does not have
a large effect on the short period SH records, it will not have a measurable
effect on the results. To summarize, the preferred value of t^*_β was
derived using an effective point source approximation. This method should
be acceptable so long as the effects of vertical directivity are
negligible. This could occur either because the vertical fracturing was
bilateral or because the rupture velocity was low. If vertical directivity
was important, it should have affected the short period S records which
it did not. Therefore, the value of t^*_β for a travel path between
southern California and the northeastern U. S. is roughly 5.2 seconds.

t* FOR DEEP FOCUS EVENTS

The short period S waves from deep focus earthquakes generally
appear to be much larger than those from shallow earthquakes. The
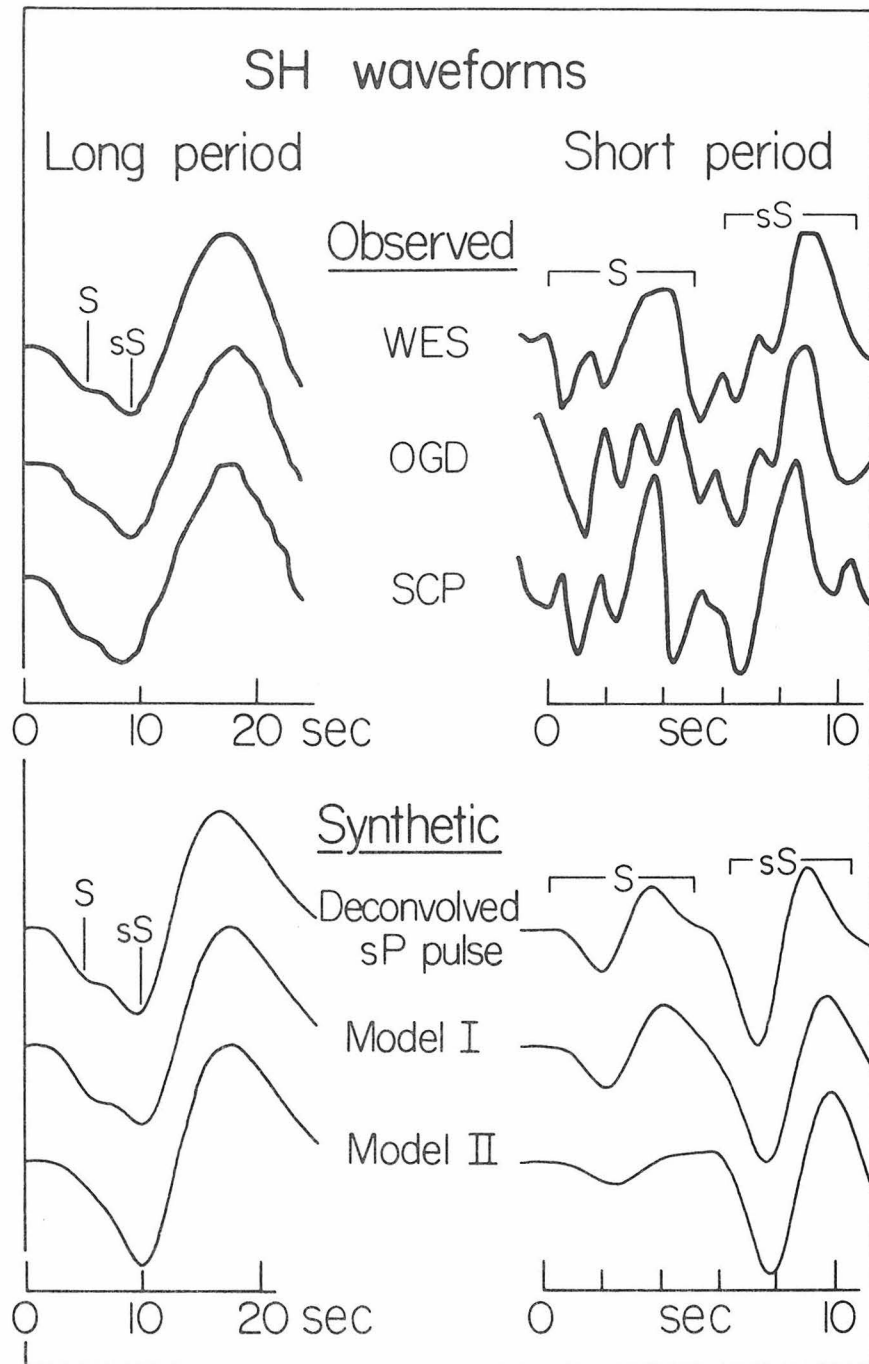
Figure 2.5   The figure compares observed long and short period SH waveforms to synthetics. The theoretical waveforms computed either by using the deconvolved sP pulse and ignoring directivity or by using model I fit the data. Model II does not fit the observed.

most likely reason for this is that body waves from deep events travel through the highly attenuating upper mantle only once while those from shallow earthquakes go through twice. This implies that t* is not only a function of distance Δ but of source depth h as well. If most attenuation does occur near the top of the mantle then for $30°<Δ<80°$ t* will be a much stronger function of h than Δ. The attenuation rate of the body waves from some deep South American events has been determined to test the consistency of the observations with current models of the Q distribution.

It is very interesting to compare the t* values of these deep South American events with the values determined from the Borrego Mountain earthquake because of the source-station geometry for the two events. The body waves for the Borrego Mountain event began at a very shallow depth in the western U. S., penetrated into the lower mantle and emerged in the eastern U. S.   The t^*_β for this path appears to be relatively high. This might possibly reflect the fact that the attenuation is more intense on only the source end of the path. Solomon and Toksöz (1970) found that the western portion of the U. S. was systematically lower Q than the eastern portion. The body waves from the deep South American events can be used to resolve whether or not this is true. These body waves start downward from a depth of nearly six hundred kilometers. This is most probably below any lateral heterogeneity associated with the South American continent. From there, they dive into the lower mantle and make a single passage to the surface either in the eastern U. S. or the western U. S. If the Q distribution along the raypath for the Borrego Mountain body waves is asymmetric it should show up as an azimuthal variation in t* for the body waves of the deep events.

The Data Set:

The four seismic events which were selected for study were moderate sized earthquakes at depths around 600 km. Three of them occurred in Argentina and one of them on the Peru-Brazil border. The locations are given in Table 2.1. The source pulse from each of the events appeared to be sharp and very simple. The long period P and S records both indicate that the source was a single unidirectional spike of short duration. The short period P's were large and very high frequency, but the short period S's were moderately sized, simple and well recorded all accross the continental U. S. Some good examples of the long and short period S waves are shown in Figure 2.6. It is interesting to compare the amplitudes of the S waves in the figure to those of the S waves from Borrego Mountain in Figure 2.1. Even when the difference in gain settings is accounted for, the short period S's from the deep event have much larger amplitudes in relation to the long periods than those from Borrego Mountain. The effects of the reduction in t^*_β for the deep events are very clear. The recordings selected for study begin at ranges of about 45° and are cut off at a range of 80°. S waves from beyond this distance are very sensitive to the structure of the core-mantle boundary. All U. S. stations in the allowed distance range were examined for record quality. The analysis procedure requires good recordings of short and long period P and S waves. This drastically reduces the number of acceptable stations.

Data Analysis:

The value of t^*_β is to be determined from the relative attenuation of P and S waves. The major difficulty with this approach is that the
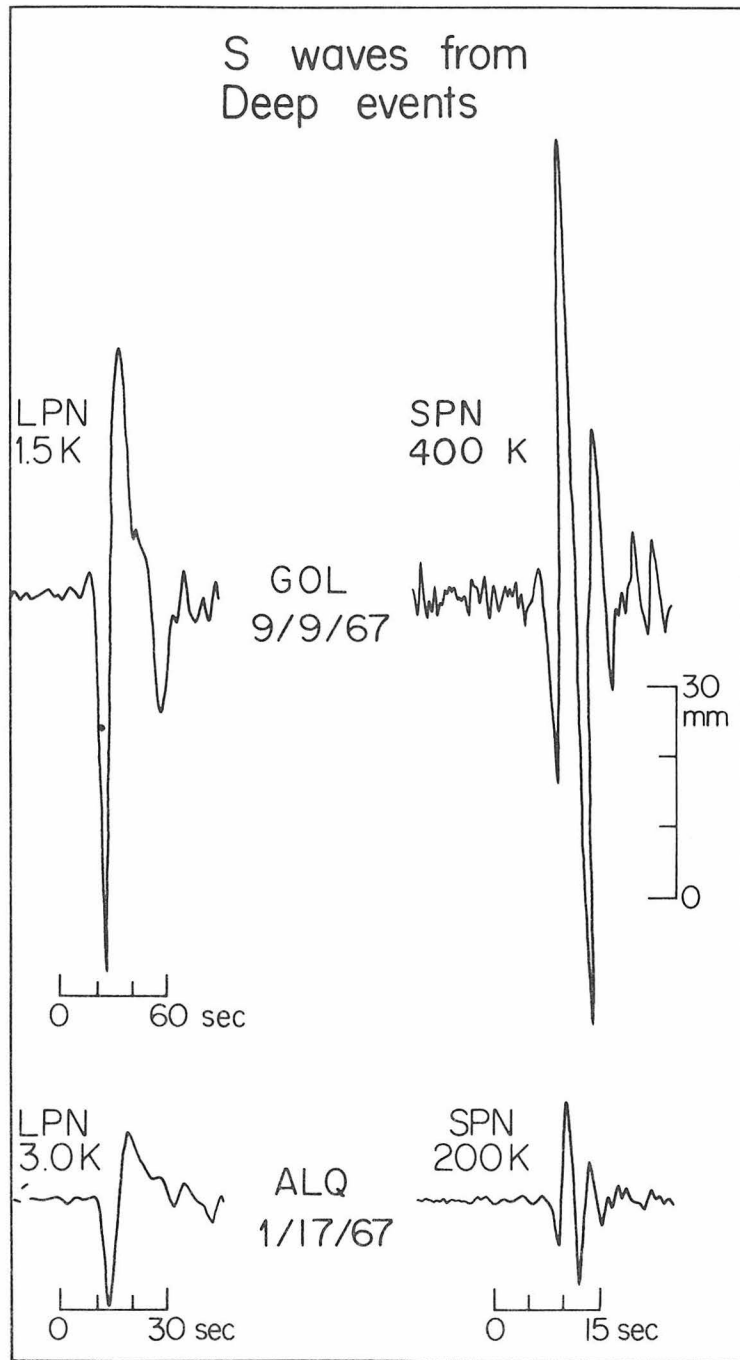
Figure 2.6   These are typical short and long period S wave records of
deep events.   The short period S is relatively large with
respect to the short period S recorded from shallow events.
This is because they have not been as strongly attenuated.

TABLE 2.1   LOCATIONS OF THE DEEP EVENTS

Location	Latitude (S)	Longitude (W)	Date	Time	Depth (km)	Magnitude
Peru-Brazil	9.1	71.3	11/03/65	1:39: 3.1	598.	6.1
Argentina	27.4	63.3	1/17/67	1: 7:54.3	590	5.5
Argentina	22.0	63.5	9/09/67	16:52:01.3	577	5.9
Argentina	27.6	63.2	8/23/68	22:36:51.3	537	5.8

initial frequency content of the P and S pulses is very difficult to
determine. Because of directivity, a source may radiate higher or
lower frequency S pulses than P pulses in some directions. It is
difficult to model the effect since the fault plane solutions of the
deep events are poorly constrained, and the postseismic data are
virtually nonexistent. The problem can be circumvented if observations
from several different earthquakes are averaged together. There should
be no large consistent bias in the frequency content of S with respect
to P.

The deep earthquake data can be rapidly analyzed by using the
following procedure. A simple measure of the frequency content of
both the P and S waves is made for each observation. This is achieved
by taking the trace amplitude ratio of the short and long period
records. Theoretical values of the P and S amplitude ratios are calculated
for a family of source models and several different t* values. The
theoretical and observed ratios are compared to find the correct value
of t*. The short period-long period amplitude ratio is defined as

$$R_{S \text{ or } P} = (A_{sp}/A_{lp})_{S \text{ or } P} \qquad (7)$$

A is the gain corrected, maximum trace amplitude of either the short
period (sp) or long period (lp) record. The values of A are measured
in the first 10 seconds of record after arrival time. As before, all of the
source scaling terms are cancelled by taking the ratio of the long and
short period amplitudes. R should depend only on the amount of energy
in the short period frequency band. The amplitude ratio R is very
similar to the power ratio r defined by equation 2. r is a more
stable measure of the high frequency signal strength, but R can be

much more rapidly determined. When many observations are to be analyzed it is more practical to use the amplitude ratio R.

The observed values of R_S and R_P for the four South American events are given in Table 2.2. The stations are designated as EUS for eastern U. S. or WUS for western. A comparison of the two groups should indicate whether the western U. S. is much more attenuating than the eastern. A separate group of anomalous R determinations is given at the bottom of the table. These measurements will be discussed separately.

Calculated Values of R:

The family of source models to be used in calculating theoretical values of R is simple but realistic. For this set of fault models, rupture is assumed to start at a point and spread radially at constant speed ($.8\beta$) to a circular boundary (Savage, 1966). Model I in Figure 2.3 is a representative member of the family. The set of models has two free variables. One of them is the angle between the ray direction and the normal to the fault plane. This value has been fixed at ninety degrees since this is the most probable value. Several numerical tests have shown that the results of this study do not depend on the value chosen for this angle. The second model variable is the fault radius. Synthetic P and S wave source pulses are computed for a range of values of the source radius. Synthetic short and long period seismograms are then computed by convolving in the instrument responses and the Futterman (1962) attenuation operator evaluated at a given value of t^*_β. It is assumed as before that equation 5 holds. R_S and R_P values are determined by processing the synthetic seismograms in the same way as the data. The pulses become longer period as the assumed value of

TABLE 2.2   MEASURED VALUES OF R

Event	WWSSN STATION	Δ	R_P	R_S	Group
11/03/65	GEO	48°	.068	.0082	EUS
	OGD	50°	.027	.0073	EUS
	SCP	50°	.072	.0066	EUS
	WES	51°	.049	.0096	EUS
	TUC	56°	.10	.011	WUS
	ALQ	55°	.090	.011	WUS
	GSC	62°	.11	.017	WUS
9/09/67	SHA	63°	.43	.019	EUS
	GEO	67°	.12	.011	EUS
	FLO	71°	.125	.016	EUS
	SCP	69°	.16	.010	EUS
	WES	70°	.056	.0065	EUS
	TUC	75°	.073	.0052	WUS
	GSC	80°	.073	.011	WUS
	GOL	78°	.067	.0044	WUS
8/23/68	ATL	59°	.14	.0079	EUS
	BLA	61°	.10	.011	EUS
	OGD	64°	.10	.0077	EUS
	SCP	64°	.13	.0085	EUS
	TUC	70°	.088	.0086	WUS
	ALQ	70°	.059	.0077	WUS
1/17/67	SCP	69°	.15	.0093	EUS
	GEO	67°	.14	.0090	EUS
	FLO	71°	.23	.017	EUS
	BLA	66°	.21	.0096	EUS
	ATL	64°	.18	.0082	EUS
	OGD	69°	.14.	.0075	EUS
	ALQ	74°	.24	.013	WUS
	TUC	75°	.26	.011	WUS
	LUB	71°	.33	.012	WUS
	GOL	77°	.19	.0079	WUS
	GSC	80°	.20	.013	WUS

Anomalous Measurements

Event	WWSSN STATION	Δ	R_P	R_S	Group
11/03/65	ATL	44°	.13	.058	EUS
9/09/67	OXF	67°	.67	.058	EUS
1/17/67	OXF	66°	.58	.081	EUS

the fault radius is increased, and the values of R_S and R_P decrease. Theoretical curves in the R_S-R_P plane for fixed values of t^*_β and a range of fault sizes are shown in Figure 2.7. The theoretical curves begin in the upper right with the smallest values of fault radius and drop to lower values of R_S and R_P as fault radius is increased. The complete curve for a set of models drops rapidly downward to lower values of R_S as the value of t^*_β is increased. The data points in Figure 2.7a are the measured values from the eastern U. S. stations. The data points appear to scatter around the curve predicted for the t^*_β value of 3.0. The four symbols represent the four different seismic events. It appears that in most cases R_P and R_S measurements from the same event tend to cluster together. This implies that the frequency content of the sources did not change significantly across the eastern U. S. The measured R_P and R_S values for stations in the western U. S. are compared with the theoretical curves in Figure 2.7b. The data points again appear to average around the $t^*_\beta = 3.0$ curve although the scatter is greater. The agreement between the observations from the eastern and western U. S. indicates that the average Q is approximately the same in the two regions. This means that the t* value determined from the Borrego Mountain observations is a good average value for the North American continent.

The three observed values of R which were classified as anomalous all gave very high values of R_S. The short period S waveform from Atlanta (ATL) for the 11/3/65 event was very similar to those at the surrounding stations. If it had been attenuated much less than the waves observed at nearby stations, it should have appeared to be shorter period.
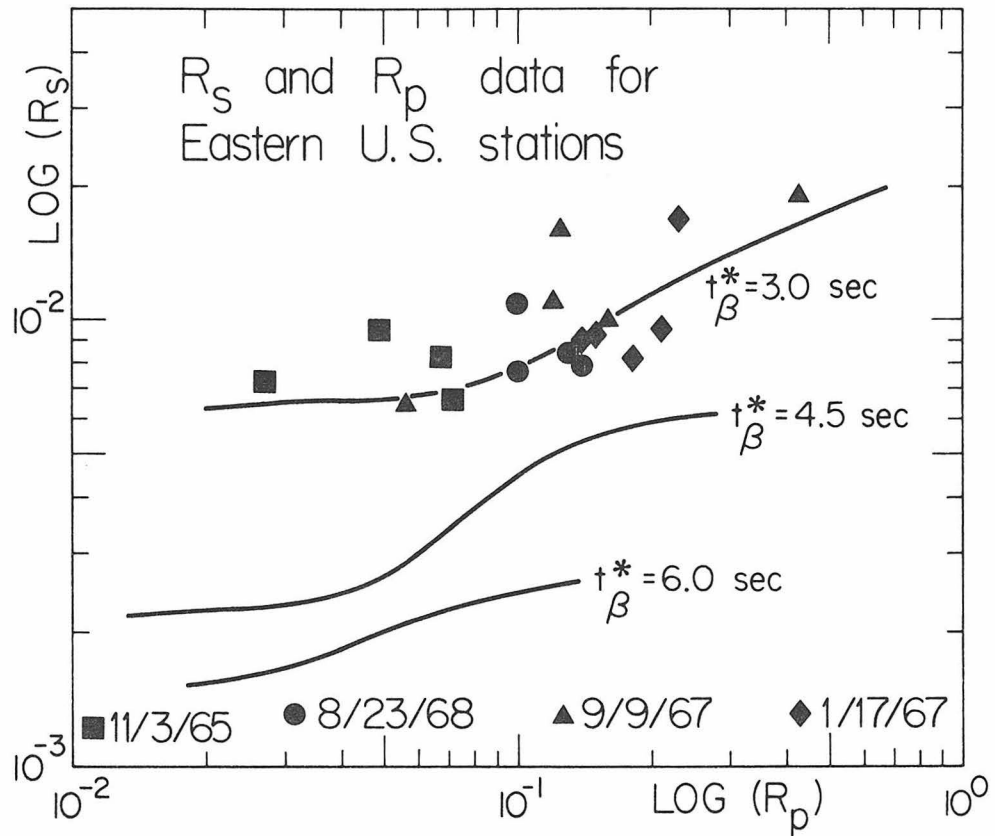
Figure 2.7a The curves represent theoretical values of R_p and R_s for a range of fault models. The data points are measured values from the eastern U. S.
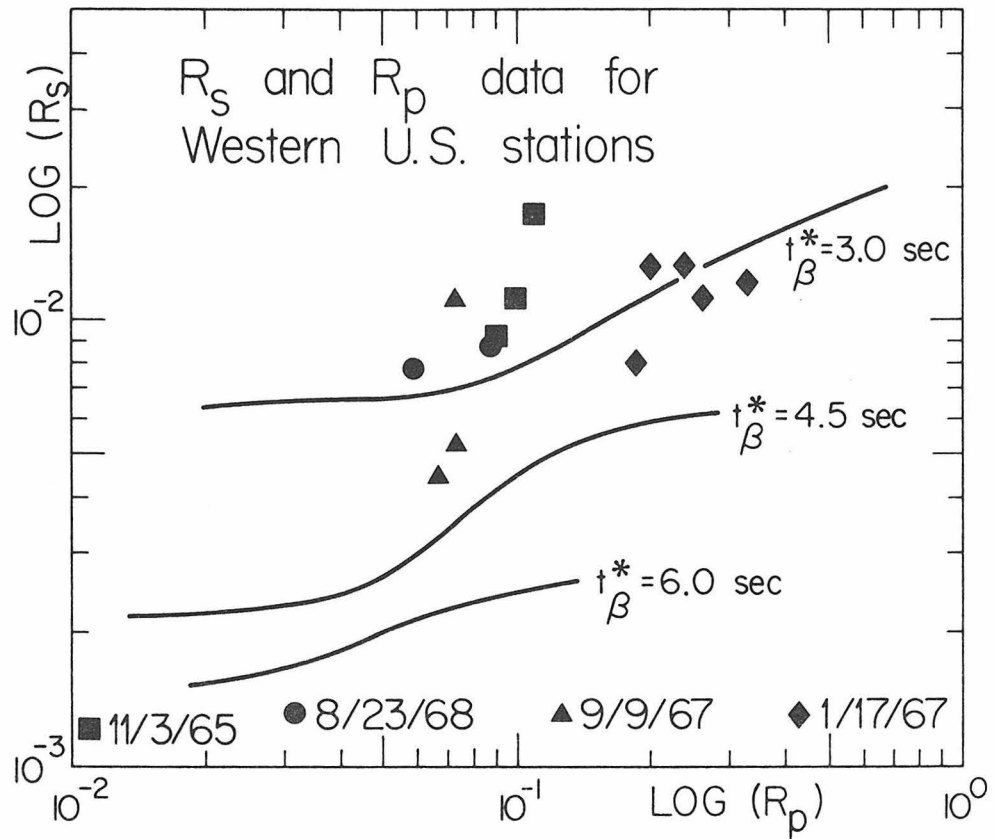
Figure 2.7b The curves represent theoretical values of R_p and R_s for a range of fault models. The data points are measured for the western U. S.

Since it did not, we assume that this was a case of miscalibration of the station. The anomalous observations at Oxford, Mississippi (OXF) of the two Argentina events appear to have been caused by focusing of high frequency energy by lateral heterogeneity along the raypath. The short period S records begin with the commonly observed signal at the usual amplitude. This is followed by a large amplitude, high frequency, ringing signal of long duration. The effect occurred for two different events which were located at virtually the same back azimuth from the station. It was not observed at nearby stations. Therefore, the focusing is probably associated with nonlayered structure under the station.

DISCUSSION

Recent advances have shown that it will be necessary to determine the Q structure of the earth in order to completely determine the velocity structure of the earth. The work of Randall (1976), Liu et al. (1976) and Kanamori and Anderson (1977) has shown that the dispersion associated with attenuation must be accounted for if normal mode data are to be related to body wave data. This implies that good measurements of the effects of attenuation in any period range have an added significance. The effects of attenuation have been shown to be very large and very easy to observe in the short period S wave data. The values of t* determined from these data should be fairly accurate, and they should supply some reliable constraints on the Q distribution of the earth. A recent model of this distribution which satisfies a wide range of observations is model SL1 of Anderson and Hart (1977). t* is an integral property, so it provides little information regarding the detailed

structure of the distribution. It should constrain the bulk properties of the model. The t^*_β value for a surface focus event at 40° for SL1 is 4.0 seconds. This is significantly lower than the $t^*_\beta = 5.2$ seconds value determined for the U. S. The SL1 t^*_β value for a 600 km deep event is 3.4 seconds. This is marginally higher than the measured value of 3.0 seconds, but the resolution of this may not be as good. Taken at face value, the two observations imply that the average Q value of SL1 for the mantle should be lower overall and that a larger portion of the net body wave attenuation should occur above 600 km.

CONCLUSIONS

The Borrego Mountain earthquake body wave data have permitted a measurement of t^*_β for a raypath from the surface of the southwestern U. S. to the northeastern U. S. t^*_β at a distance of about 35° is 5.2 ± .7 seconds. This value is significantly higher than the commonly accepted one. The deep South American earthquake data allowed a determination of t^*_β for a raypath beginning beneath the laterally heterogeneous upper mantle, going downward and emerging either in the eastern or western U. S. The t^*_β value is about 3 seconds. This is slightly lower than the value predicted by the recent Q distribution model SL1. The data place some constraint on the bulk properties of the Q distribution which should be taken into account in future Q models.

Chapter 3

A MODEL OF THE UPPER MANTLE P VELOCITY STRUCTURE

INTRODUCTION

The determination of seismic source time functions and upper mantle Q values were two problems in which the information from the WWSSN long period records had been used to good advantage, but the information from the short period records had not. The problem to be considered in the final portion of this thesis is the determination of upper mantle velocity structure. In this case, the short period information from the LRSM network has already been studied, but the long period information has not. Since the LRSM short period instrument is very similar to the WWSSN short period, the period range spanned by the LRSM short period and WWSSN long period instruments is about the same as the period range considered in the previous chapters. The purpose of this final section will be to correlate the waveform information from these two instruments and to use it to find an upper mantle P velocity profile.

Helmberger and Wiggins (1971), Wiggins and Helmberger (1973), and Dey-Sarkar and Wiggins (1976a) have developed and applied a very sensitive technique for determining upper mantle compressional velocity structure. The method involves fitting the relative times and amplitudes of secondary arrivals in short period P waveforms from bombs and earthquakes. A crucial step in the technique is to make a careful determination of the source pulses of the seismic events which are used in the study. This allows the effects of upper mantle structure on the waveform to be separated from those of the seismic source. Recent advances have made it possible to make accurate determinations of the

source pulses of earthquakes in a period range appropriate for the WWSSN long period instrument (Fukao, 1971; Helmberger, 1974; and Langston and Helmberger, 1975). This in turn has made it possible to carry out an upper mantle study which is similar in form to the previous short period studies but based on the long period records. Short period P waveform data, $dT/d\Delta$ observations and travel time measurements have also been included in the data set to make it as complete as possible.

The fundamental step of determining the source pulses of several moderately sized earthquakes has been accomplished in a series of related works. The events were the Borrego Mountain earthquake (Burdick and Mellman, 1976), the Oroville earthquake (Langston and Butler, 1976), and the Truckee earthquake (see Chapter 1). The source determinations were made using records from the epicentral ranges between 30° and 90° where the effects of mantle structure could be neglected. The source models turned out to be accurate enough to fit almost every detail of the records from these ranges. These high quality source models were the real key to the success of the upper mantle study. The waveforms used in the mantle study came from the epicentral ranges of 10° to 30° where the effects of upper mantle structure are strong. The source models made it possible to match these waveforms almost as closely as those from greater distances.

The basic technique of the mantle study was to presume that the ground motion at an observing station could be represented as a convolution of the known source pulse with the response of the unknown velocity

structure. The upper mantle velocity model was determined by computing synthetic seismograms for an assumed starting model using a generalized ray algorithm. The model was perturbed by trial and error until a compressional velocity profile was found which predicted the shape of the observed waveforms. This method has already been used for the problem of determining shear velocity structure by Helmberger and Engen (1974). However, because their data set was limited, they were only able to identify a second arrival from one of the two upper mantle discontinuities. Also, they were unable to use short period data because attenuation of shear waves is so intense. In this study, strong second arrivals from both discontinuities have been specifically identified in the long period P waveforms. The final model accurately predicts not only the long period data but the short period, travel time, and dT/dΔ data as well.

The final model which will be designated as model T7 differs from previous models in several important ways. One of the most interesting of these is that even though it fits a larger body of data, it is basically simpler than the earlier models. Most of the velocity gradients are purely linear and the discontinuities are first order. The two major discontinuities have been reduced in size in the new model and the velocity gradients between them have been made stronger to compensate. Also, the third discontinuity which has appeared in many recent models at a depth of about 500 km has not been included in this model since there is no justification for it. The sizes and locations of the two remaining discontinuities are well justified by the data.

THE REGION OF STUDY

Most of the short period waveform studies which have occurred to date have concentrated on determining the upper mantle structure of the western and central portions of the North American continent. This region was selected because the Nevada test site and nearby active fault zones provided a large number of seismic sources and because the LRSM, WWSSN, and Canadian networks provided dense station coverage. Western North America has also been extensively studied by the more conventional methods of modeling travel times and apparent velocity data (Massé, Landisman, and Jenkins, 1972; Julian, 1970; Julian and Anderson, 1968; Archambeau, Flinn, and Lambert, 1969; Lehmann, 1962, 1964, 1967; Niazi and Anderson, 1965; Johnson, 1967). All of these previous studies make western North America an excellent testing ground for a new method such as modeling long period and short period waveforms simultaneously.

An important result of these studies is that there are significant lateral variations in the upper mantle structure even within western and central North America. The region must be subdivided even further to avoid them. Wiggins and Helmberger (1973) found that the United States had to be divided into the regions NE of Nevada test site and NW or SE of Nevada test site. They called the model for the NE region HWB and the model for the NW-SE region HWA. Dey-Sarkar and Wiggins (1976a) divided western Canada into three regions with associated models WCA, WCB, and WCC. All of this means that unless the source and station locations are chosen with care body waves will not sample a homogeneous section of mantle.

The location of the three earthquakes with known source pulses make the region modeled by Wiggins and Helmberger (1973) with HWA a natural choice as the region for the long period waveform study. The area is shaded in Figure 3.1. Massé, Landisman, and Jenkins (1972), Lehmann (1967) and Julian (1970) studied travel time profiles and Niazi and Anderson (1965) and Johnson (1967) studied apparent velocities within the region. The area is the most tectonically active portion of the continent and geologically speaking includes portions of the Great Basin, Southern Basin and Ranges, Southern Rockies, Klamath Wallows, Colombia Plateau, and the Colorado Plateau. More importantly, it can be characterized seismically as a region where the lid of the low velocity zone is very thin or absent altogether. Beneath the low velocity zone, there is a strong velocity gradient which causes strong first arrivals from 14° to 16°. This can be contrasted with the HWB region which has a thick lid and a very weak gradient under the low velocity zone. The velocities are faster overall in the HWB region, so seismograms between 14° and 20° have weak, relatively early first arrivals. Wiggins and Helmberger (1973) found that records from beyond 20° did not differ as drastically with location as those from shorter ranges. This simply means that the mantle is more homogeneous below a depth of about 400 km. We will follow their example and restrict the data set to records of body waves with travel paths within the HWA region for distances less than 20°. At greater ranges, we will include records from all azimuths.
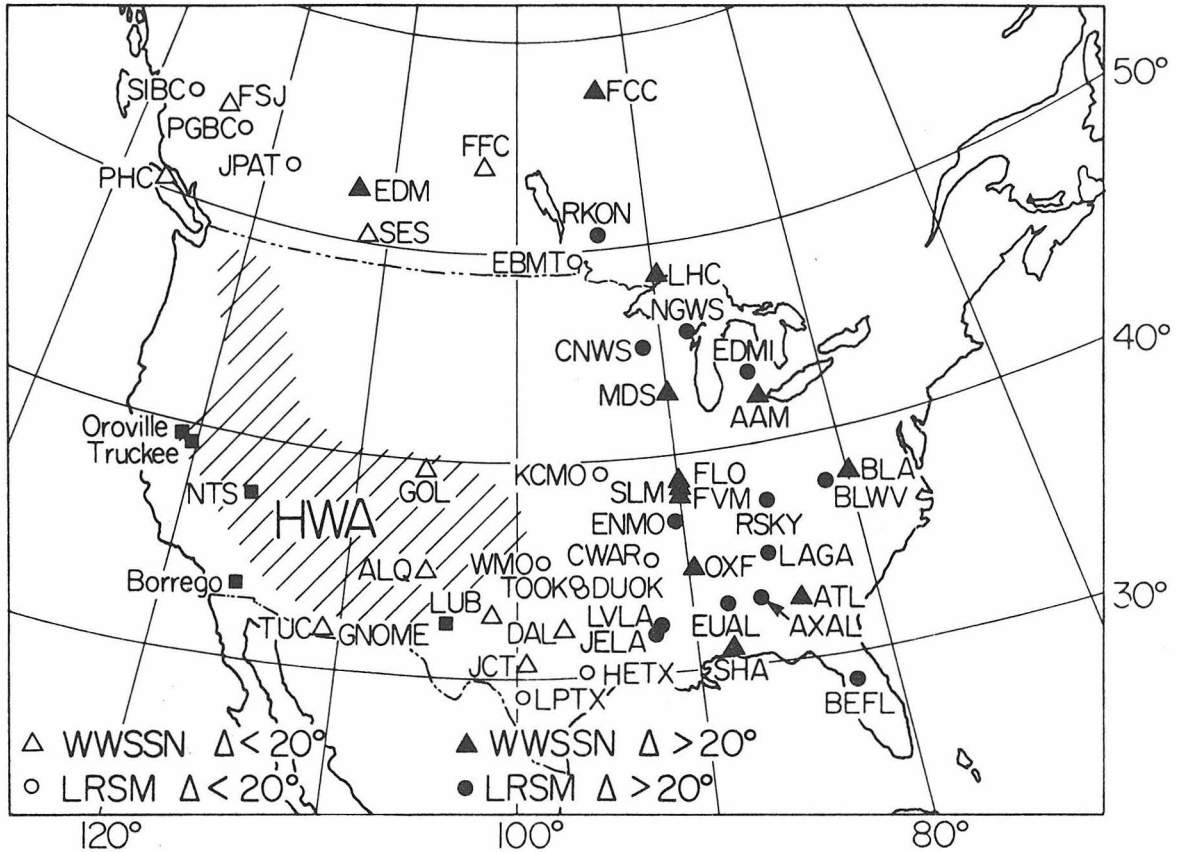
Figure 3.1   The map shows the location of the seismic events and
recording stations with respect to the region of study
(shaded) which is marked HWA.

COMPUTATIONAL TECHNIQUE

The fundamental technique for computing synthetic seismograms is to represent each of the different factors which affect the waveshape by a linear, time dependent operator. The synthetic is then just a successive convolution of all of the operators. So if Y(t) is the synthetic seismogram, it can be written as

$$Y(t) = S(t) * M(t) * O(t) * A(t) * I(t) \qquad (1)$$

The operator S represents the seismic source, M the mantle response, O the receiver response, A the Futterman (1962) attenuation operator, and I the instrument operator. Wiggins and Helmberger (1974) have presented a very detailed discussion of the techniques for computing the mantle response M(t) using the generalized ray formalism. Langston and Helmberger (1975), Fukao (1971), and Helmberger (1974) have reviewed all of the methods necessary to compute S(t) for shallow double couple sources and have discussed the attenuation and instrument operators as well. Helmberger and Engen (1974) have combined the techniques to model the upper mantle shear structure. Therefore, only a few additional comments are required here.

Decomposition of the Earth and Source Operators:

First, it is necessary to explain more carefully how the double couple source has been inserted into the generalized ray formalism. If the earth response to an earthquake source was computed exactly, then each generalized ray would include a unique source term which would be a function of time. The earth and source operators would have to be combined into a single composite operator E(t). However, since the

rays travel nearly vertically when they are close to the source or receiver, they behave very much like geometric rays and the time dependence of the source is very weak. The earth response can be approximately written as

$$E(t) = S(t) * M(t) * O(t) \tag{2}$$

$S(t)$ should be understood to represent the downgoing compressional pulse leaving the source region. For a double couple point source, it is computed using the first motion approximation as described in Langston and Helmberger (1975). The source terms, which in the exact formulation would be functions of the Cagniard de Hoop transform variable p, are all evaluated at p_0, the ray parameter of the direct ray. $M(t)$ is then the response at the base of the crust under the observation point due to a downgoing delta function compressional wave from the source, and $O(t)$ is the response at the free surface due to a compressional wave at the base of the crust under the observation point. The advantage of using this approximate form is that it is only necessary to compute $M(t)$ once for a given range. When this has been done, synthetic seismograms can be computed for that range using any seismic source $S(t)$. This significantly reduces the cost of the computational procedure.

The Attenuation Operator $A(t)$:

A second approximation has been used to write $A(t)$ as a separate term in equation 1. The approximation used is very similar to the one used to separate $E(t)$ into its component parts. The Futterman

attenuation operator is a function of t*. This parameter is defined
as T/Q, the ratio of the travel time of a given ray to the average
quality factor along the raypath. But the mantle response M is a sum
over many rays and each has a different raypath with a different travel
time and a different Q. The operators M(t) and A(t) should actually
be combined into a composite operator F(t) where for a given range

$$F(t) = \sum_i R_i * A_i \qquad (3)$$

R_i is a generalized ray, A_i is the attenuation operator evaluated at
the correct value of T* and the sum extends over all generalized rays.
If the variation of A_i's within the set of rays is small then it is
true that

$$F(t) \approx A(t) * \sum_i R_i = A(t) * M(t) \qquad (4)$$

where A(t) is the attenuation operator evaluated at an average value
of t*. The approximate form has been used quite frequently with good
success, (Helmberger (1973), Helberger and Engen (1974)) and ordinarily
would deserve no further comment. But recently Kennett (1975) has
questioned the validity of this technique. He suggested that for
reasonable models of Q and velocity structure the different rates of
attenuation of two arrivals on a seismogram would significantly change
their relative amplitudes. This in turn might cause a misinterpretation
of the size or sharpness of a discontinuity in the upper mantle.

To test the approximate method, synthetic seismograms were computed
for two different Q models at distance ranges 15°, 16° and 17°. Each
ray was convolved with the appropriate Q operator, A_i, as expressed in
equation (3). At these important ranges the direct arrival turns

around just under the low velocity zone while the second arrival travels all the way down to the first major discontinuity at 400 km depth. If the approximation breaks down anywhere it should do so in this case. The first Q model is the one proposed by Helmberger (1973). In this model, all of the losses occur in the heavily attenuating low velocity zone. The second model is model SL1 of Anderson and Hart (1977). In this model the attenuation of the rays occurs more uniformly throughout the upper mantle. The assumed velocity structure was model T7, the source for the short period records was a bomb source and the source for the long period records was a theoretical dip slip fault source. The synthetics for the Helmberger model are shown in the column on the left in Figure 3.2, those for SL1 are in the center and those computed from the approximate method are shown on the right. A comparison of the 15° records shows that some differences can be seen between the synthetics for the Helmberger model and the synthetics for the other two models. The differences become much smaller at 16° and 17°. This means that if the Helmberger model is correct and most attenuation occurs in a small region of very low Q, it could have some effect on the relative amplitudes of arrivals. However, the scatter in the waveform data is large enough so that variations like those shown in Figure 3.2 generally are not too significant. Therefore, the synthetics in this study were computed using the approximate method expressed in equation (4). If it becomes apparent that there are concentrated regions of low Q in the upper mantle, then the final velocity structure, model T7, may have to be modified accordingly.
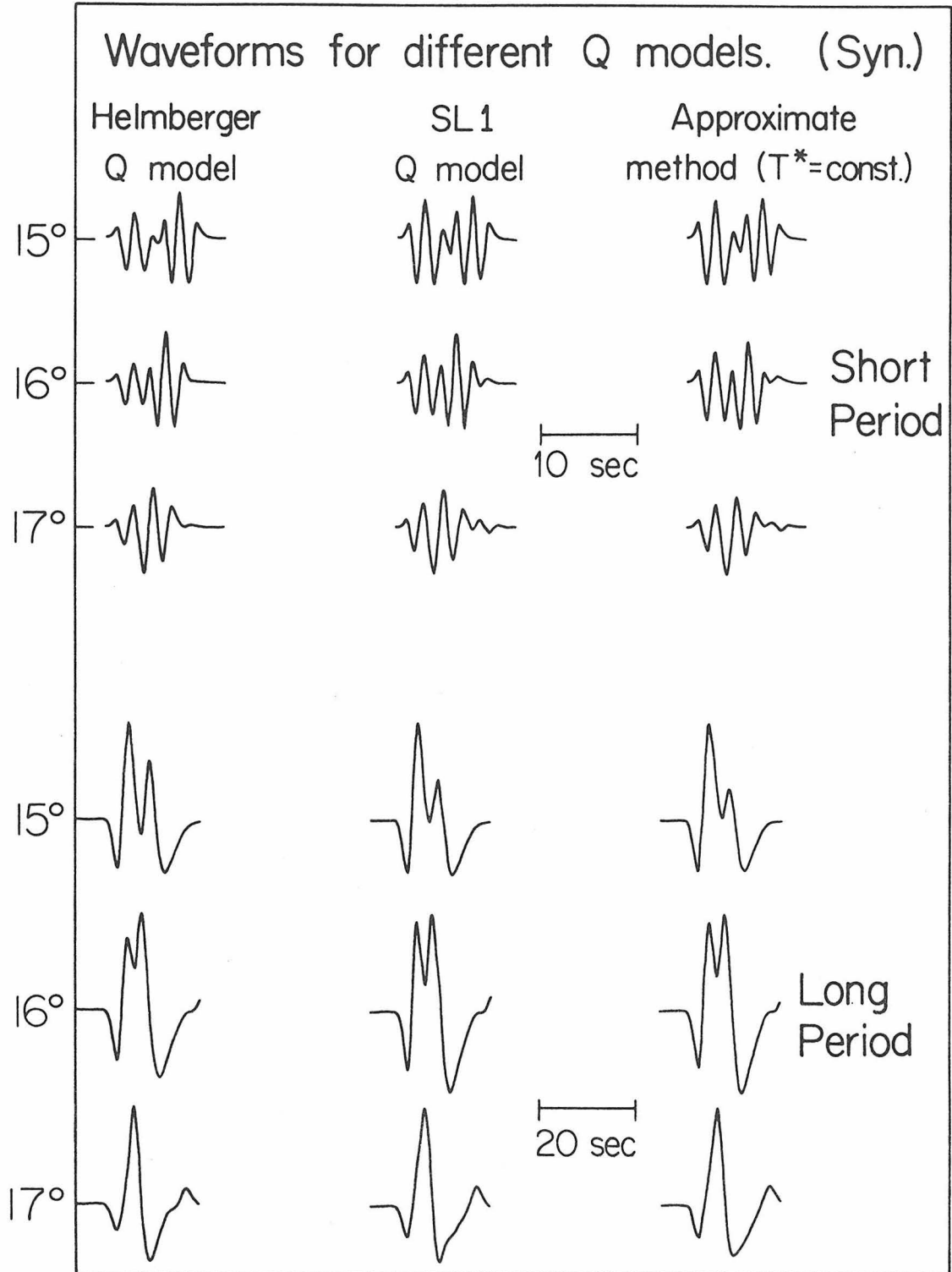
Figure 3.2   These are synthetic waveforms computed either by convolving
each ray with its own Q operator (left two columns) or
by convolving all the rays with a single average Q operator.
Some differences appear at 15° for the Helmberger Q model,
but differences of this order are not significant.

The Source Operator S(t):

The two groups of source operators S(t) which were used in this study were already illustrated in Figure 3.2. The first group contained NTS bomb sources which were for short period records and the second group contained theoretical earthquake sources which were for long period records. Helmberger and Wiggins (1971) and Dey-Sarkar and Wiggins (1976a) have already discussed a simple method for modeling NTS bomb sources. A high quality short period record from the ranges between 30° and 50° is assumed to represent the composite response of all the operators except the upper mantle response M(t). Thus, if this master record is called R(t), then the short period synthetics Y_{sp} can be written

$$Y_{sp}(t) = R(t) * M(t) \qquad (5)$$

The master record used for all short period synthetics in this study was the one from NTS event Greeley recorded at BEFL ($\Delta=30^\circ$). This method is very straightforward but does not account for a very significant effect. All bomb source functions contain two predominant rays. These are P and pP. The formalism does not take into account the fact that the relative amplitudes of these rays changes significantly in the range of interest. This means that the synthetics can only be expected to roughly match the relative amplitudes and relative times of secondary arrivals. Since the source pulse S(t) is of limited accuracy, they cannot exactly match the short period waveshapes.

The second group of source functions consisted of theoretical earthquake sources which were used for long period records. The source models were models for the 8/1/75 Oroville earthquake, the 9/12/66

Truckee earthquake and the 4/9/68 Borrego Mountain earthquake. A detailed description of the source models is given in appendix 3. It should be reemphasized that the upper mantle modeling study would not have been possible without these accurate source models. Appendix 3 shows that there are very few details of the 30° to 90° seismograms which these source models do not predict. This made it possible to predict with some confidence the pulse $S'(t)$ which entered the upper mantle for a given ray parameter and azimuth. The distortion of $S(t)$ by the mantle response $M(t)$ into the observed pulse could then be modeled by trial and error.

The completely theoretical long period source models have one additional advantage over the empirical short period models. The distance dependance and source dependance of the three phases P, sP and pP can be included explicitly. This permits much more accurate fits of the long period waveforms than of the short.

The Receiver Operator O(t):

It may have seemed unnecessary to have written $O(t)$ in expression 1 as a separate operator from $M(t)$, particularly since it is generally an unknown function. In practice, in studies of both long and short period waveforms, it is usually approximated as a delta function. However, the function $O(t)$ requires very careful consideration since breakdown of this approximation is one of the greatest difficulties in waveform studies. Any record must be examined carefully for contamination by near receiver crustal phases before it is included in the data set.

The difficulties are most **pronounced** in the case of short period records. Helmberger and Wiggins (1971), in using those records, attempted to circumvent the problem by using only those stations which appeared to be transparent. These stations were defined as being those which gave simple signatures for small events at ranges between 30° and 90°. However, because this definition is only qualitative, there are still some difficult decisions to make about which are important features in a record and which are not.

To illustrate this point, two records of NTS blasts from the neighboring stations Jena, Louisiana (JELA) and Liddieville, Louisiana (LVLA) are shown in Figure 3.3a. The most obvious second arrival is the distinct phase about 7 seconds back in the LVLA record. However, at this range, the secondary arrivals from the upper mantle should all be crowded into the front of the record. The large secondary arrival is probably a crustal phase. However, making this decision on an **a´priori basis would have** been very difficult. It is also interesting that LVLA indicates that the arrival at about 20.5^o should begin with a small precursor and JELA does not. The choice of which record to fit must be based on still other records from nearly the same range. With this type of noise in the data, it is clear there must always be some feedback between what is predicted by the acceptable upper mantle models and which records **are** chosen for the data set.

The problem of contamination of long period records by structure under the receiving station is less severe than it is for short period records. This is because the longer period waves average over the

The effects of receiver structure

LVLA SP Z
$\Delta = 20.4°$
NTS – Bilby

JELA SP Z
$\Delta = 20.8°$
↓ Anomalous secondary arrival
NTS – Greeley

10 sec

(a)

FFC LP Z
Strong P to S converted arrivals
Truckee 9/12/66

LPE

LPN

10 sec

(b)
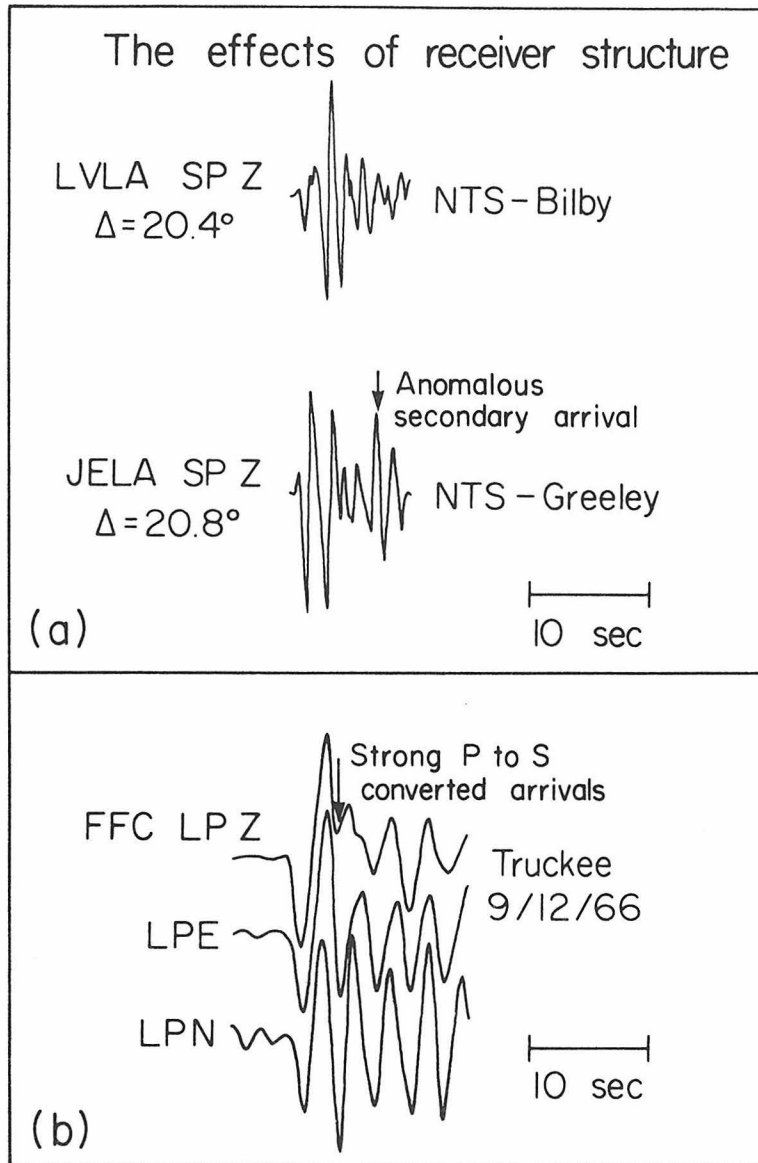
Figure 3.3   The figure shows that complex velocity structure under the recording station can badly contaminate either long period or short period records. The short period bomb records in Part A are from neighboring stations. They should be identical, but the JELA record contains a large anomalous arrival generated near the station. Part B shows horizontal and vertical long period records of a P wave.   If there were no S energy present, the components would be identical. The arrow marks the onset of strong P to S converted arrivals. It must be presumed that reflected P arrivals are also present.

small scale features. However, the long period records can still be strongly influenced by receiver structure. Burdick and Langston (1977) have shown that the amount of signal contamination of near receiver crustal phases can be determined in a relatively quantitative way. When **sharp** velocity contrasts are present under a station, they produce strong phases of the P to S converted type. These phases can be easily identified by comparing records of the vertical component of P wave motion to the horizontal. At a transparent station the horizontal component will look like the vertical. At nontransparent stations there will be strong differences between the two. At many stations the near receiver crustal complications can be modeled with a plane layered geometry. At **still others** it is necessary to use dipping structure (Langston, 1976).

An example of severe contamination of long period records **is shown** in Figure 3.3b. The records shown are the three components of motion from the Canadian network station at Flin Flon, Manitoba for the 9/12/66 Truckee event. The horizontal components of motion begin to diverge markedly from the verticals at the point indicated by the arrow. This means the P waveform contains some significant SV arrivals. It is also apparent that since the two horizontal components of motion do not match, the SV phases are emerging at a skewed angle. Records from stations like FFC were included in the data set used in this study, but they were assigned a greatly reduced significance. In the following presentation, the horizontal components of P wave motion will be shown along with the vertical waveform whenever the horizontals are of acceptable quality. The degree of contamination of the records by

receiver structure can then be assessed by comparison of the two components.

THE DATA SET

The data set for this study was chosen to be as comprehensive as possible both in terms of the number of observations and in terms of the different kinds of observations. Every available long period WWSSN record from each of the three earthquakes was included in the set making a total of 33 long period P observations. The short period data set contained all the NTS event LRSM records used in the short period waveform study which resulted in HWA. But the short period earthquake records were excluded. This was because the more recent studies of long period earthquake sources have indicated that it is essential to include the azimuthal and distance dependence of the source in the theoretical waveform calculations. Because of this, the technique of using a master short period record from the 30° to 50° range will not work for earthquake sources. The theoretical earthquake source models used for the long period records are not sufficiently accurate in the short period range. Dey-Sarkar and Wiggins (1976a) have had some success in using short period records from earthquakes, but they had to process the data heavily with an unstable deconvolution scheme. Also, they required data from a very abbreviated azimuth range and an extended distance range. The short period data from the original HWA study did not satisfy these tight restrictions. The distance and azimuth data for the observing stations have been given in Table 3.1, and the station and source locations are shown in Figure 3.1. The

TABLE 3.1   STATION DATA

Event	Station	Distance (°)	Azimuth (°)
Truckee	GOL	11.4	83.8
	ALQ	11.8	108.0
	PHC	12.4	337.8
	FSJ	15.3	350.8
	JCT	18.8	112.0
	DAL	19.9	101.9
	FFC	19.6	32.6
	FLO	23.0	82.0
	MDS	23.0	70.2
	YKC	23.4	6.6
	OXF	24.9	91.6
Oroville	TUC	11.3	125.9
	GOL	12.5	83.7
	SES	13.2	30.7
	FSJ	15.1	353.9
	LUB	16.8	104.2
	JCT	19.9	110.0
	FFC	201.6	34.3
	YKC	23.5	8.2
	DAL	21.0	100.5
	SLM	24.3	81.9
	FVM	24.3	83.5
	FFC	20.2	34.3
	LHC	24.8	58.1
	SHA	28.6	97.4
	BLC	29.1	22.7
	INU	29.6	351.0
Borrego	EDM	20.2	4.8
	SHA	23.8	88.2
	ATL	26.5	80.5
	AAM	27.1	60.8
	BLA	29.4	71.8
NTSA	LPTX	15.8	115.2
	TOOK	16.0	93.9
	CWAR	19.5	88.5
	CNWS	20.4	58.8
	NGWS	22.6	58.6

TABLE 3.1   STATION DATA - continued

Event	Station	Distance (°)	Azimuth (°)
NTSB	DUOK	16.4	94.7
	HETX	17.9	106.6
	EBMT	19.4	43.2
	LVLA	20.5	96.8
	BLWV	27.5	77.8
NTS	RKON	21.1	42.9
NTSC	JPAT	15.8	355.5
	BGBC	17.4	347.2
	SIBC	19.2	240.3
	ENMD	20.3	83.1
	RKON	21.0	42.3
	AXAL	24.8	91.0
	RSKY	24.8	80.4
	EDMI	24.8	65.9
	LAGA	24.8	86.1
NTSF	RKON	20.0	43.1
NTSG	PGBC	17.2	347.7
	WMO	14.5	93.5
	KCMO	17.2	76.5
	JELA	20.8	98.2
	RKON	21.1	42.9
	EUAL	23.8	92.4
	SHA	24.3	97.4
	AXAL	25.2	91.3
	WHYK	26.2	339.2
NTSJ	RKON	21.1	43.0

source data are in Table 3.2. The four letter station codes are for LRSM stations and the three letter codes are for WWSSN stations. The open symbols in Figure 3.1 are for stations at ranges less than 20°. The records from these stations should be unique to the HWA region. The closed symbols are for stations at greater distances. These should produce records more characteristic of the earth as a whole.

Like the short period waveform data, the travel time data set was limited to readings of nuclear blasts. Since a full range of data was available from these high quality sources, it seemed superfluous to include travel time readings from earthquakes. Readings from the NTS blasts were either made directly from the WWSSN records or taken from the AFTAC reports on the blasts. Data from the Gnome blast in eastern New Mexico to stations in the western U. S. were taken from Romney et al. (1962). The apparent velocity data set was the one reported by Johnson (1967) of measurements made at TFSO.

MODEL T7

The velocity model HWA was derived from much of the same data that were used in this study to derive the final model T7. The only difference was that the older study was based exclusively on short period waveforms and the newer was based on both short and long period data. Yet the two models are markedly different. HWA was used as a starting model in this study and was perturbed by trial and error into T7. In this section, we will carefully review how and why each alteration of the starting model was made. We will also attempt to show precisely which part of the data set constrains which features of the new upper

TABLE 3.2   SOURCE LOCATIONS

Event	Lat (N)	Long (W)	Date	Time (GMT)
Truckee (Tru.)	39.44	120.16	9/12/66	16:41:02.6
Oroville (Oro.)	39.44	121.53	8/01/75	20:20:12.8
Borrego (Borr.)	33.19	116.13	4/09/68	02:28:59.1
Aardvark (NTSA)	37.07	116.03	5/12/66	19:00:00
Bilby (NTSB)	37.06	116.02	9/13/63	17:00:00
Boxcar (NTS)	37.30	116.46	4/26/68	15:00:00
Corduroy (NTSC)	37.16	116.05	12/03/65	15:13:02
Faultless (NTSF)	38.63	116.22	1/19/68	18:15:00
Greeley (NTSG)	37.30	116.41	12/20/66	15:30:00
Jorum (NTSJ)	37.31	116.46	9/16/69	14:30:00

mantle compressional velocity profile.

TRAVEL TIMES AND dT/dΔ DATA

Theoretical travel time curves for models T7 and HWA are compared
with the data in Figure 3.4. The solid line shows the complete,
critical ray travel time curve for model T7. The broken line indicates
the travel time curve for the first arrivals for model HWA. HWA
is conspicuously early at ranges between 17° and 30°. As the starting
model was being altered to fit the waveform and dT/dΔ data, it was
also slowed down to achieve the good fit to the travel time data shown
here. Total travel time is a broad integral property of a model while
the theoretical waveforms of a model depend more strongly on its fine
structure. In the trial and error modeling procedure it became apparent
that the two types of data could be fit more or less independently of
each other. HWA could have been easily adjusted to give a better fit
to the travel time data, but this was not the only difficulty with the
starting model.

Theoretical curves for models HWA and T7 are compared with the
dT/dΔ data set in Figure 3.5. It must be conceded that model HWA fits
the data better overall. This is because Wiggins and Helmberger (1973)
generated all of their models by drawing curves through the dT/dΔ data
and inverting with a Wiechert-Herglotz algorithm. Model T7 was
generated by trial and error perturbation in the velocity depth plane.
There is an important difference of interpretation of the data for
the two models at high values of dT/dΔ. At the point where the HWA
curve goes through the data with a branch from above the low velocity
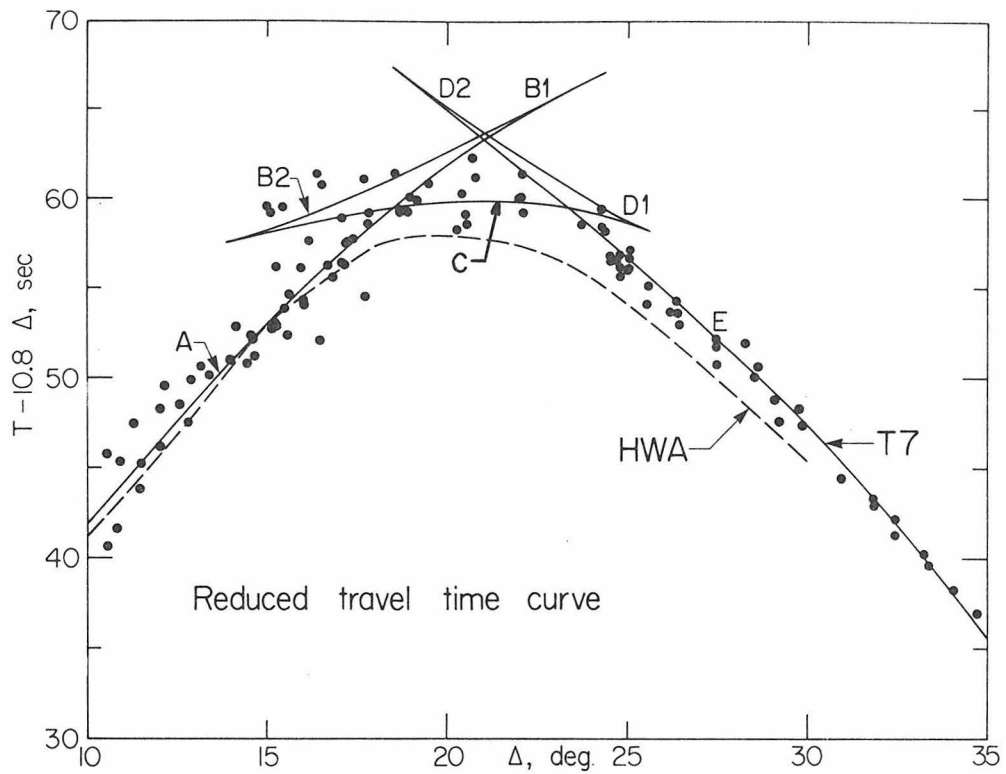
Figure 3.4   The figure compares the theoretically reduced travel time
curves for HWA and T7 to the observed data. All the
observations and the HWA curve are for first arrivals only.
The T7 curve is for all critically reflected arrivals.
HWA appears to be too fast in the ranges 17° to 30°.
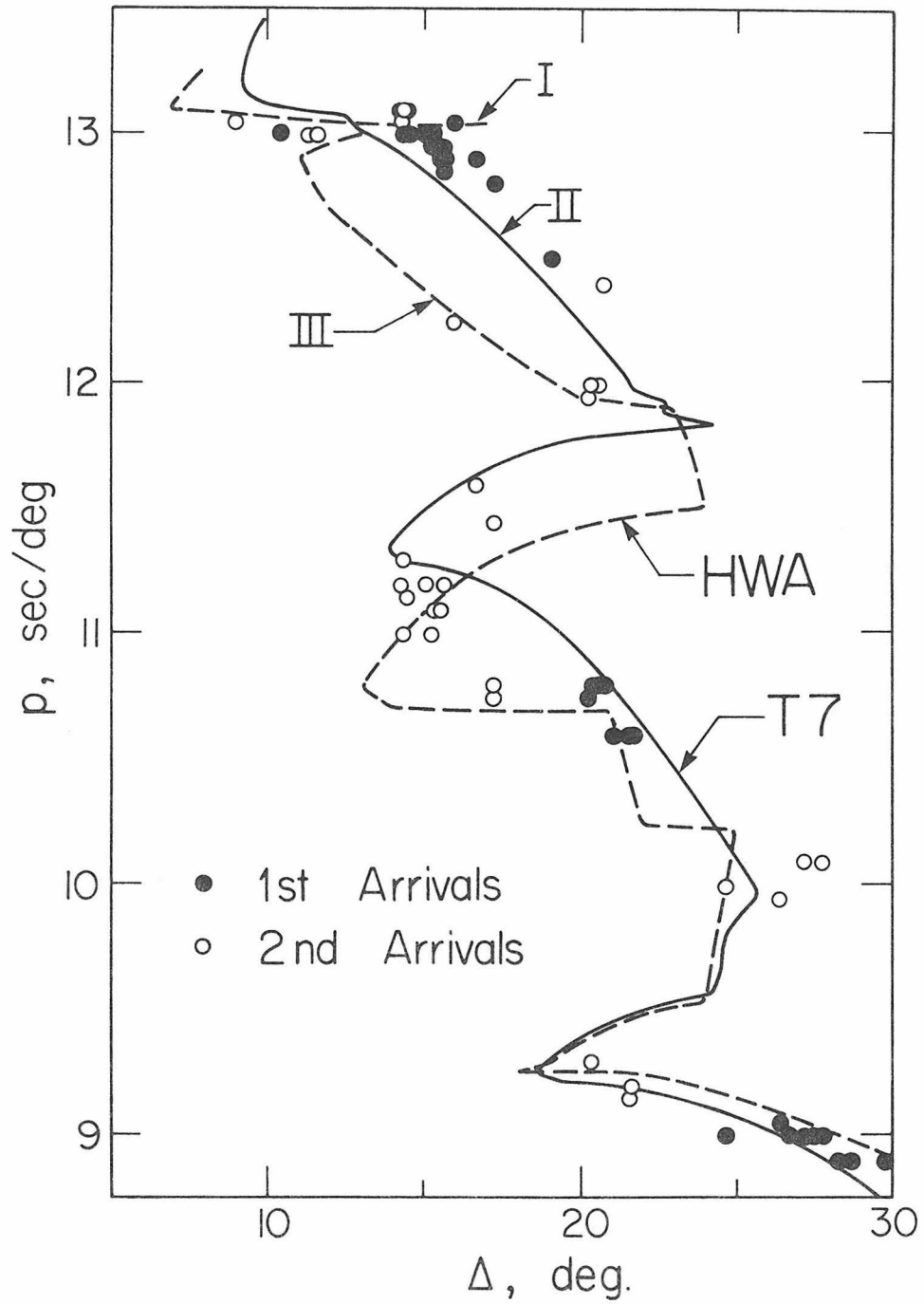
Figure 3.5   The figure shows the apparent velocity data set and the
theoretical curves predicted by models HWA and T7.   The
branches of the HWA curve marked I and III come from
above and below the LVZ respectively.   Branch II of the
T7 curve comes from below the shallower LVZ of model T7.

zone (branch I), model T7 has a branch from beneath the low velocity zone (branch II). This single difference of interpretation leads to many other major differences between the two models. The way in which these differences arise will be discussed in the following sections.

THE LITHOSPHERE AND ASTHENOSPHERE

The western portion of the United States is an area characterized by widespread variation in the seismic properties of the crust and lid. (Pakiser, 1963), Pakiser and Zietz (1965), Prodehl (1970), Herrin (1969). Since no single model can be appropriate for the entire region, a good average model can do no more than have approximately the right average distribution of delay times between the crust, lid and low velocity zone. The crust of model T7 was constructed so as to satisfy the observation of Carder et al. (1966) that the direct arrivals from nuclear blasts at ranges less than 13° scattered about the curve

$$T = \Delta/7.9 \text{ km/sec} + 7.0 \text{ sec} \qquad (6)$$

in the western U. S. The choice of lid thickness and lid velocity had to be made much more arbitrarily than the choice of crustal thickness and velocity. Observed Pn velocities have generally ranged between 7.6 km/sec and 8.2 km/sec. The average lid velocity of model T7 was set at 8.0 km/sec which appears to be a rough average value for the whole region. (Carder et al. 1966) The upper parts of models HWA and T7 are compared in Figure 3.6. It is apparent that there are some significant differences between the two models.
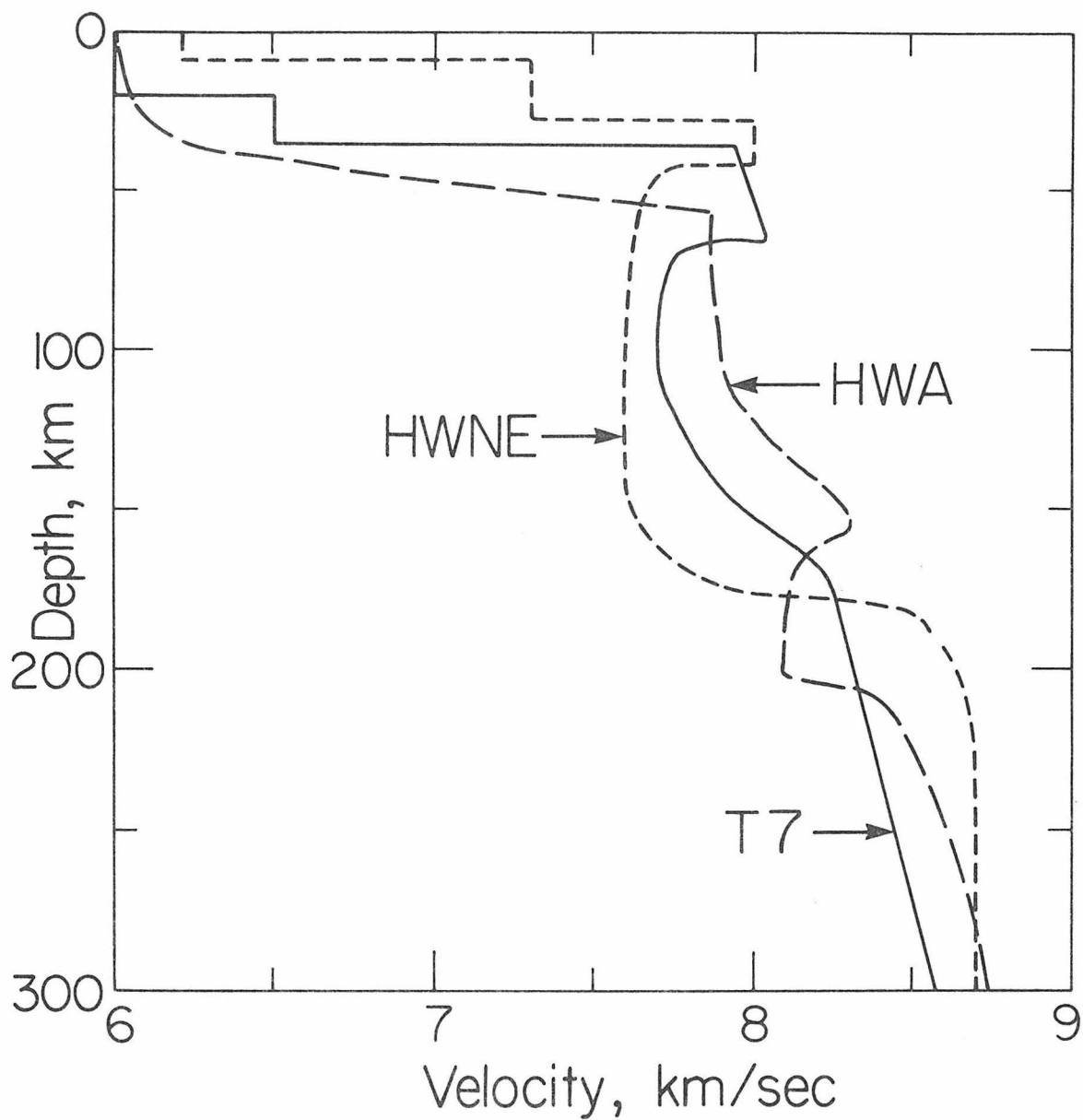
Figure 3.6   The figure compares the top of the velocity profile T7
             to two other profiles which have been proposed. The HWA
             low velocity zone does not adequately account for the
             dT/dΔ data.   The HWNE profile does not satisfy the long
             period waveform data.

The most important difference between the two is in the depth and size of the low velocity zone. This difference originates in the two different interpretations of the dT/dΔ measurements of the first arrivals in the range 14° to 17°. The observation that the first arrival in this range should have a slowness of about 13 sec/deg. is probably one of the best in the dT/dΔ data set. At these ranges the small to moderate sized earthquakes used by Johnson (1967) should still have given strong signals, and since the phase of interest is the first arrival, there should have been no ambiguity in picking the times. HWA was constructed by assuming that these arrivals came from the branch marked I in Figure 3.5. Branch I is before the discontinuous jump in the HWA dT/dΔ curve. This jump is caused by the low velocity zone. In other words, the first arrival in the 14° to 17° range for HWA is still coming from the lid. There is a second critical arrival in HWA at these ranges which is marked as branch III in Figure 3.5. It is coming from below the low velocity zone. Since branch III goes through only one data point it is presumably very difficult to observe. The flaw in this method of interpreting the data can be seen through the use of this general rule. When the slope of the dT/dΔ curve is low, as it is for branch I in Figure 3.5, then the amplitude of the arrival is small. When the slope is high, as it is for branch III, the amplitude is large. The situation is illustrated more fully in Figure 3.7. The two synthetic seismograms in the figure were computed using a bomb source and the earth responses of HWA and T7 at $\Delta=14^{\circ}$. As shown in the figure, I is much smaller than arrival III. If the HWA interpretation is correct,
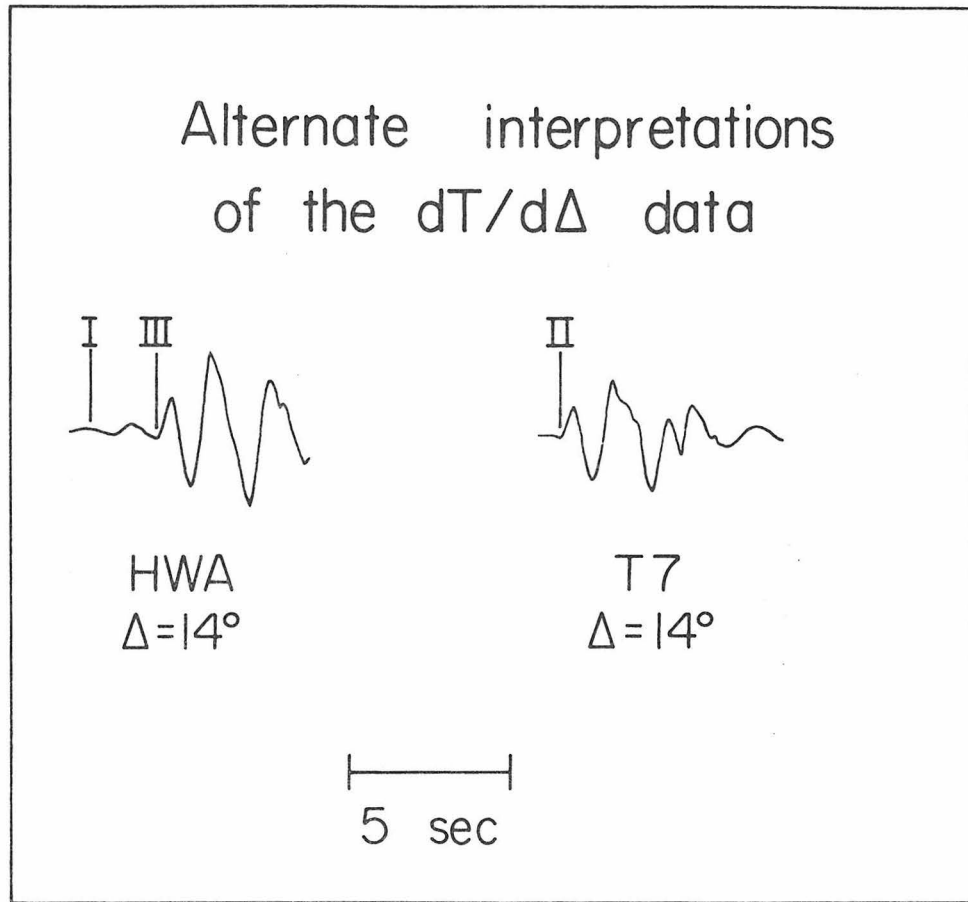
Figure 3.7   The synthetic short period waveforms illustrate the
             difference of interpretation of the dT/dΔ data used
             in constructing models HWA and T7.   The HWA inter-
             pretation supposes that the velocity of arrival I
             was consistently measured, but arrival III was very
             rarely seen even after arrival III crossed over to
             become the first arrival.   The T7 interpretation
             supposes that the strong arrival II was consistently
             observed at ranges between 14° and 17°.

then Johnson correctly picked arrival I as the first arrival at 14° but missed the much larger III as a second arrival. The two arrivals cross over at 14.5^O. So to produce this observed data, Johnson would have had to completely miss the large first arrival and consistently have measured the velocity of the much smaller second arrival in all records between 15° and 17°. If the T7 interpretation is correct, then he was observing the strong arrival marked II in Figure 3.7, as the first arrival throughout these ranges. The latter seems to be a much more reasonable explanation of the data.

The records which are most sensitive to the structure around the low velocity zone are those from the ranges 10° to 15°. Unfortunately these records are also still sensitive to the highly variable lid structure. Also, the effects of receiver structure become very strong at these ranges so P waveform data become relatively unreliable. The records of acceptable quality from these distance ranges for the Truckee and Oroville earthquakes are shown in Figure 3.8.

The vertical component of P wave motion is shown in dark line at the top right of each group of records. In the second row are the component parts of the synthetic waveform and the synthetic itself. At the left is the effective source pulse which contains all component responses except the delta function response of the upper mantle, $M(t)$. The lightly filtered delta function response of the earth is next and finally on the right, directly under the data is the synthetic. Synthetics for other models of interest are shown in successive rows. The horizontal components of P wave motion are shown in the last row in

Long period records from 10° to 15°
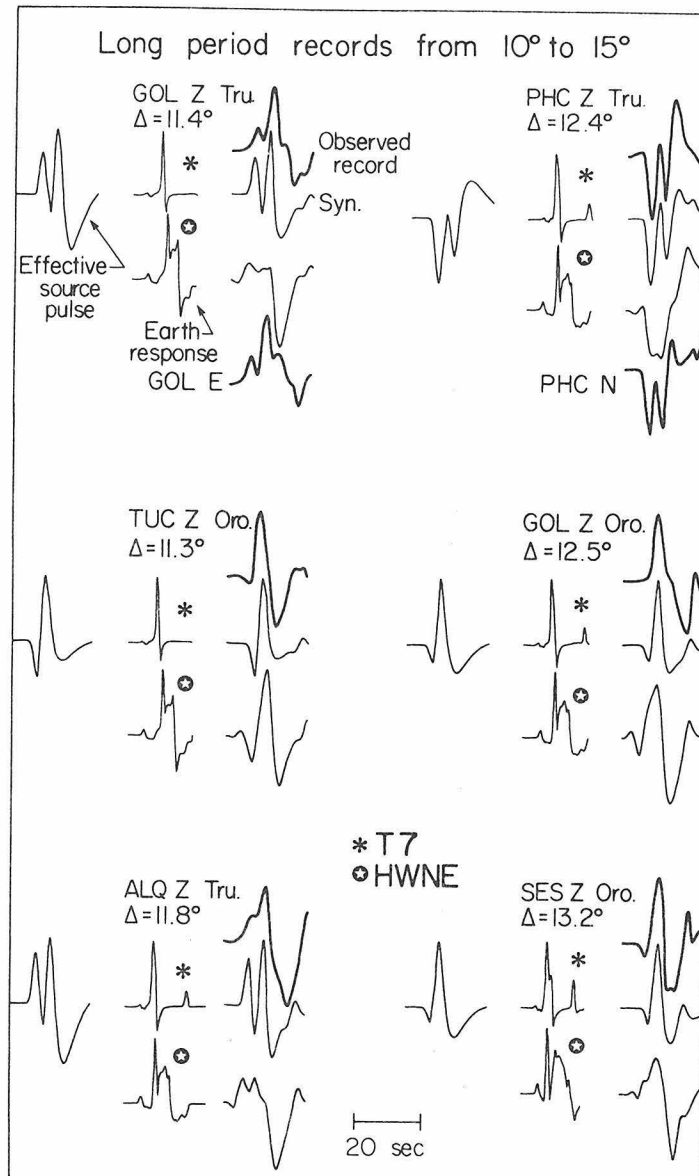
Figure 3.8 The Figure compares long period data and synthetics for the ranges 10° to 15°. The effective source pulse is shown at the left for each station. The delta function responses for models HWNE and T7 are in the center column. The data is shown in the last column in dark line with the synthetics underneath in light line. Model T7 appears to be acceptable, but HWNE is not. The observed horizontal components are also shown in the last column for some stations. They do not match the observed vertical components very closely indicating that receiver structure is important at those ranges.

dark line when they are of acceptable quality. They should be compared with the observed vertical components of motion as a test for anomalous particle motion. This basic format will be used to display the data and synthetics in many of the following figures.

The synthetics for model T7 fit the observations adequately, but there are still many details in the observed waveforms that are unaccounted for. The horizontal components at GOL and PHC indicate that, as expected, receiver structure is distorting the signals. Also, the laterally varying lid structure is probably affecting the waveforms. Because low velocity zones do not generally have a strong effect on waveforms, a large class of models would fit the data as well as T7. HWA is among them. Any model for the lithosphere and asthenosphere which fits the observed apparent velocities and travel times and which predicts a relatively simple pulse in the 10° to 15° ranges would be as acceptable as T7. Models of this type have been suggested by Johnson (1967), Helmberger (1973) and Archambeau et al. (1969).

There is one type of model which is definitely not compatible with the data in Figure 3.8. This is the type in which the velocity increase under the low velocity zone is taken in a single large jump. To conserve travel time there can be only a small velocity gradient under that. This means that only a small direct arrival is turned up by the weak gradient while a strong second arrival is reflected by the velocity jump. One low velocity zone model of this type was proposed by Helmberger and Wiggins (1971) for the portion of the U. S. to the northeast of Nevada test site. The model is called HWNE. It is shown in dotted line in Figure 3.6, and the corresponding synthetics are shown

in Figure 3.8. The predicted waveforms definitely do not fit the observed at GOL, ALQ and SES. Models with strong reflectors beneath the low velocity zone have been proposed by Masse et al. (1972), Niazi (1969) and Lehmann (1962) for the western U. S. and by Fukao (1977) for the Japan-Kurile area.

The details of the structure of the compressional wave low velocity zone are constrained only very weakly by the available data. Johnson (1967) argued for a prominent low velocity zone on the basis of travel time residuals for the entire mantle. Helmberger and Wiggins (1971) also argued for a substantial zone on the basis of a combination of travel time and amplitude data. Neither argument was particularly strong. Dowling and Nuttli (1964) proposed a model with a comparatively small low velocity zone on the basis of the travel time data from nuclear blasts.

THE TRANSITION REGION

The remaining portions of the HWA and T7 velocity profiles are shown in Figure 3.9. HWA has the first major discontinuity at 425 km, an inflection in velocity slope near 525 km and a second major discontinuity at 650 km. Model T7 has the first discontinuity at 395 km, no inflection in velocity slope and the second discontinuity at 670 km. T7 has been made slower than HWA throughout the transition region so that it would provide a better fit to the travel time data in Figure 3.4.

The long period data which constrain the location and size of the upper discontinuity in model T7 are shown in Figures 3.10 and 3.11. The second arrival from branch B2 in Figure 3.4 can be most clearly identified in the two records from 15° at the top of Figure 3.10. The arrival is marked by an arrow. The arrival from B1 is clearest in the records
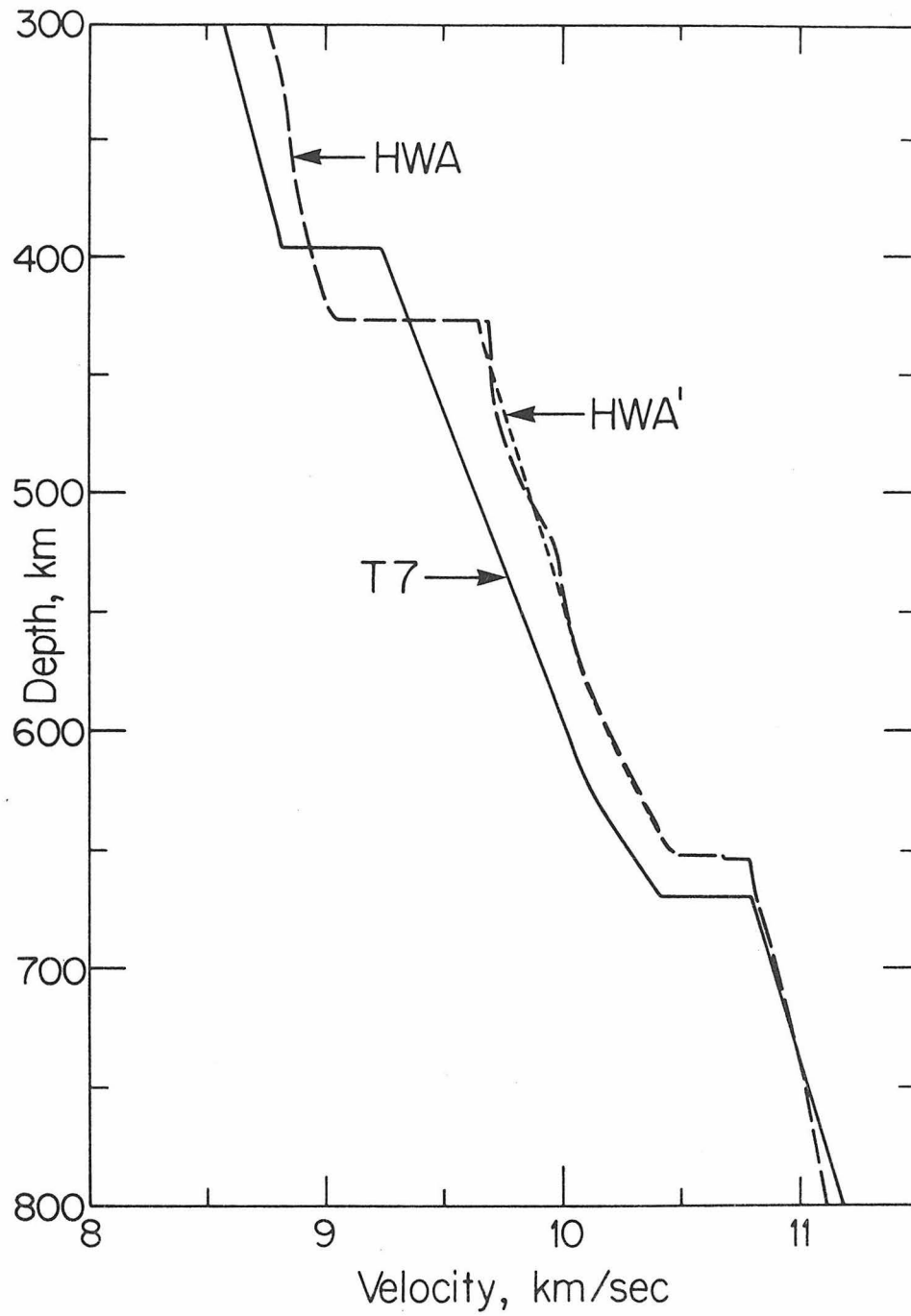
Figure 3.9   The figure compares the lower portion of the velocity
models HWA, HWA' and T7. Model T7 is slower than the
other models and has the discontinuities at different
depths. Model HWA' is just model HWA without the 525
km discontinuity.
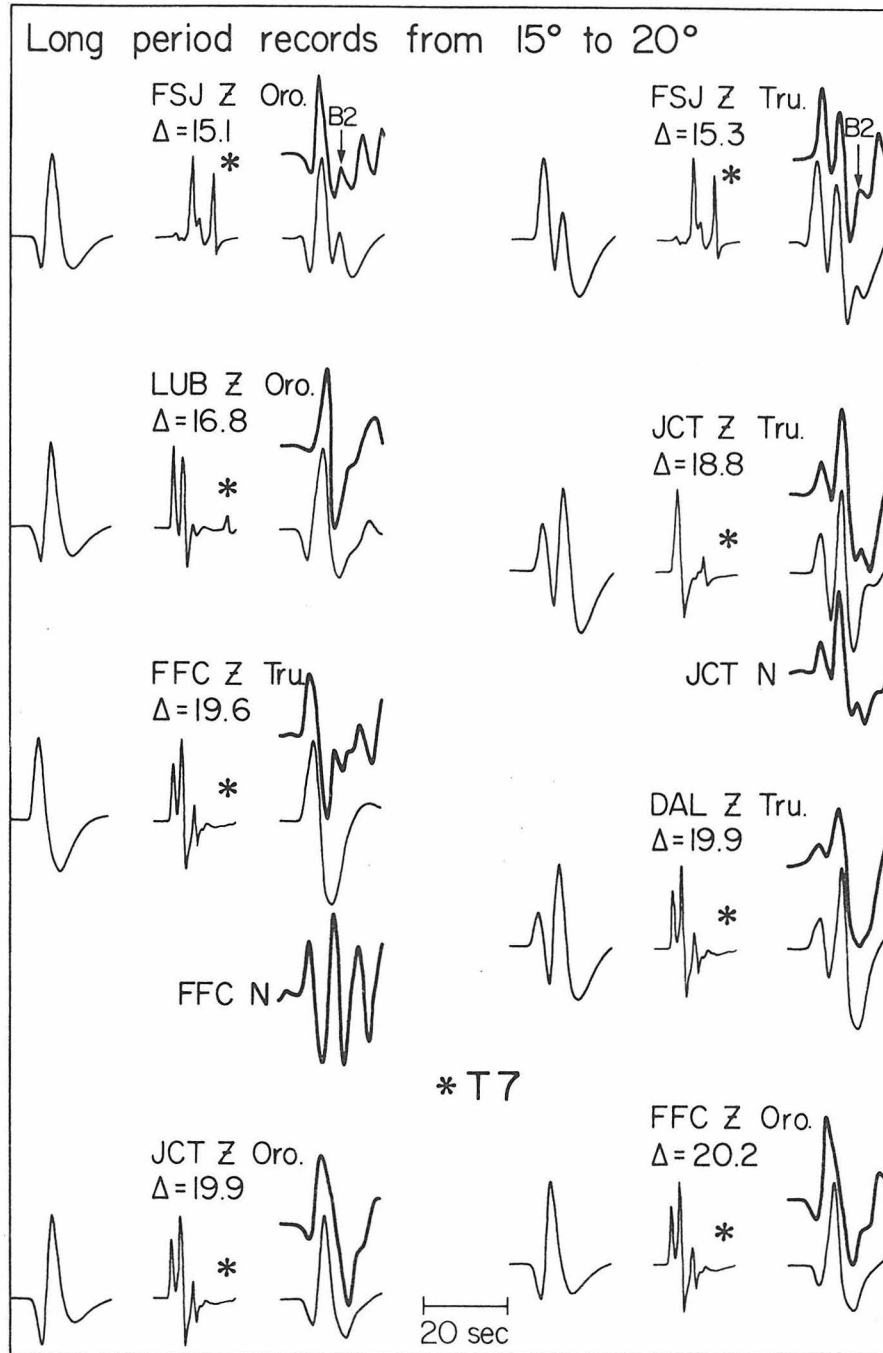
Figure 3.10 The long period records shown in the figure contain two arrivals. The second arrival which is marked as B2 is a reflection from the 400 km discontinuity (see Figure 3.4). The effective source function is shown on the left for each station. The filtered delta function response for T7 is next and the synthetic seismogram is on the right in light line. The observed record is on the right in dark line.
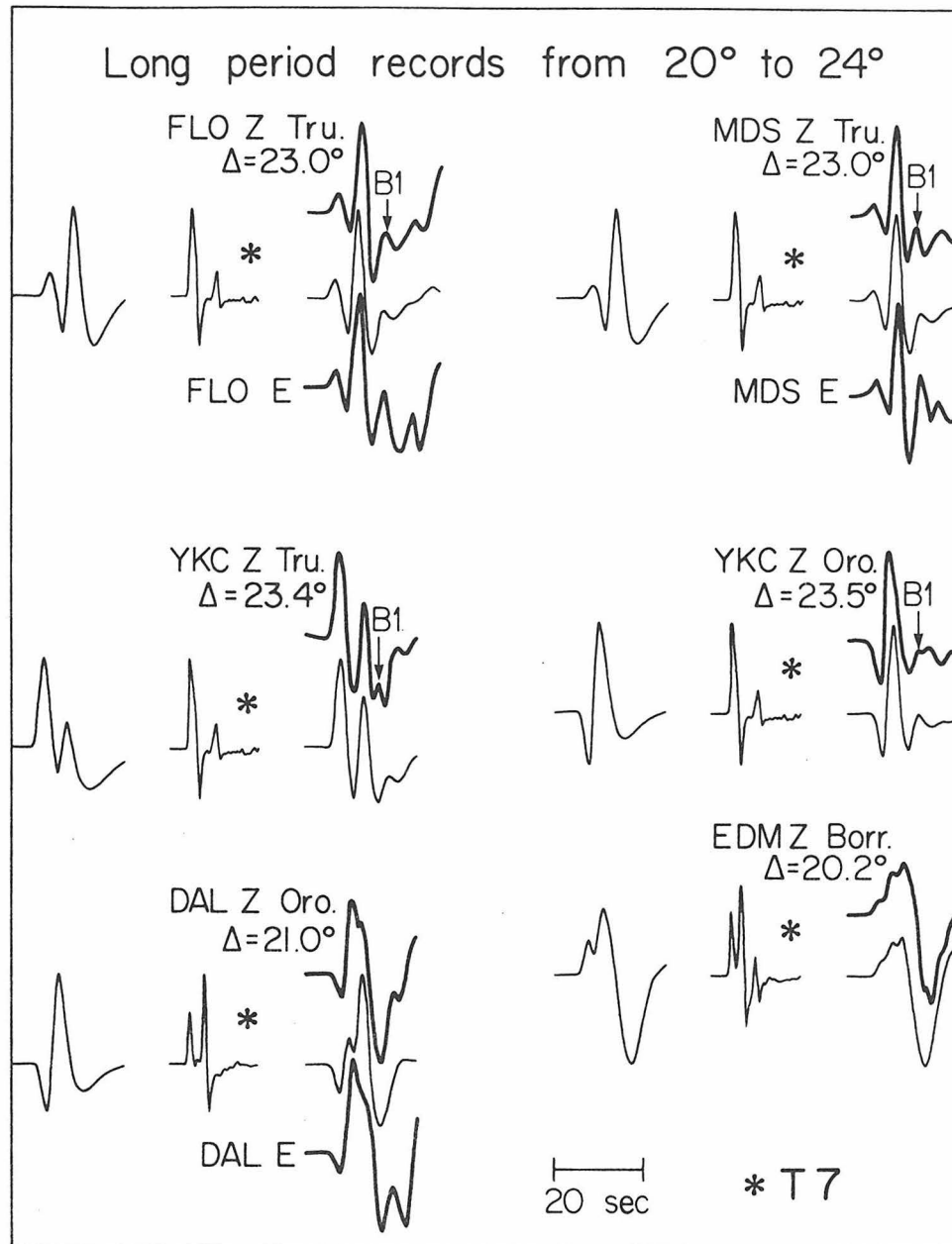
Figure 3.11   The long period records shown in the figure contain three arrivals.   The arrival marked B1 is a reflection from the 400 km. discontinuity (see Figure 3.4).   An arrival from the 670 km discontinuity arrives at the same time as the direct arrival at about 23° and at the same time as the 400 km discontinuity arrival at 21°.   It appears in the delta function response as a small third arrival at 20.2°. The organization of the figure is the same as for Figure 3.10.

from near 23° shown in Figure 3.11. For ease of comparison, some of the records from Figures 3.10 and 3.11 have been changed in sign so that the dominant arrival would consistently break upward. The high quality observations of both the B2 and B1 branches of the triplication serve to constrain the depth and size of the discontinuity very closely. When data from only one branch are available, it is usually possible to trade off the depth against the size to a much greater extent.

The short period records which contain second arrivals from branch B2 in Figure 3.4 have been compared with synthetics computed for T7 and HWA in Figure 3.12. The relative times and amplitudes of the second arrivals are compared with theoretical curves in Figure 3.13. Even though HWA has a deeper discontinuity than T7, the synthetics for the two models in Figure 3.12 appear to be very similar. The reason is that the first arrival in HWA bottoms much deeper than it does in T7. Therefore, the arrival from the discontinuity must come from a greater depth as well. The bottoming depth of the first arrival in T7 was set at a shallower level because of the reinterpretation of the $dT/d\Delta$ data at 15°. The bottoming depth for the ray from the discontinuity was correspondingly elevated to 395 km. In order to match the relative amplitudes, the size of the discontinuity was reduced from a jump of 7.2% in HWA to a jump of 4.8% in T7.

Attempting to find a single upper mantle model for all of the HWA region is an ambitious undertaking. The region has arms stretching both N to NW and E to SE from the source regions. It would have been surprising if there had been no evidence at all of variation between the two arms. In fact, records from the northern arm as well as a few from the eastern
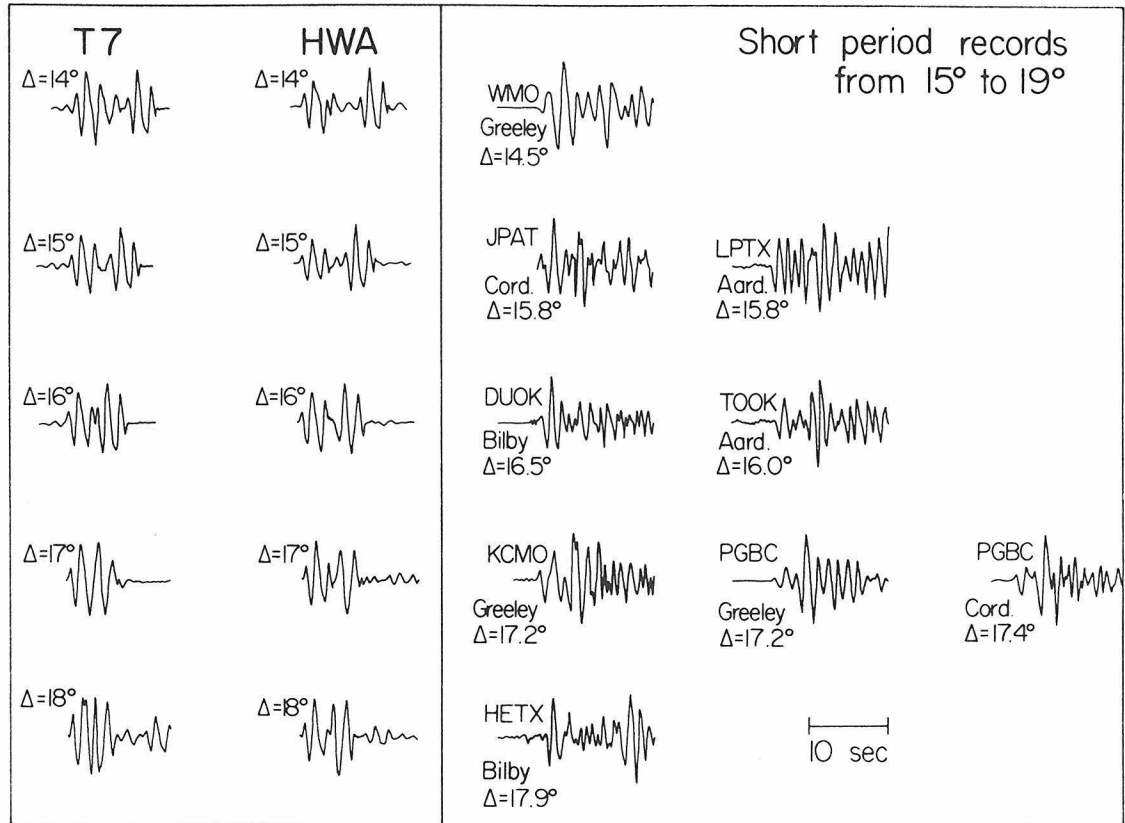
Figure 3.12 The figure compares synthetic and observed short period
records of nuclear blasts. The second arrival at these
ranges is a reflection from the 400 km discontinuity.
The synthetic waveforms for T7 and HWA are very similar
and both appear to be consistent with the data.
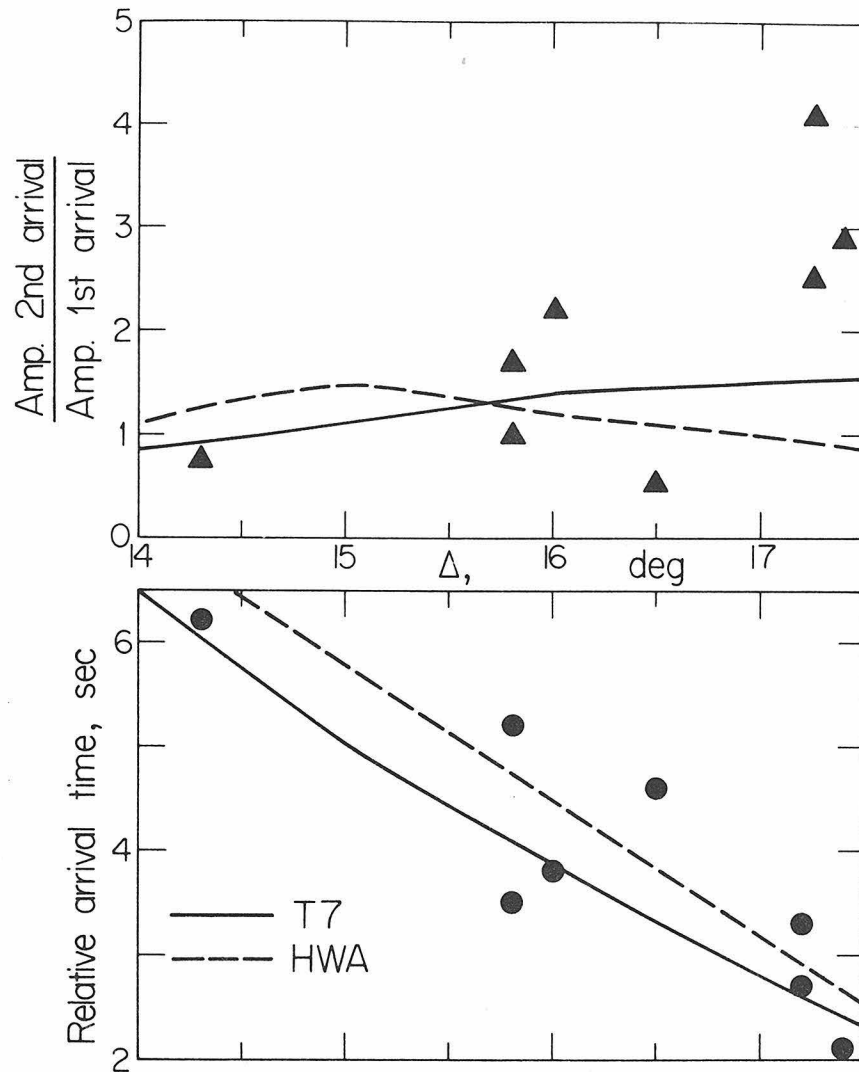
Figure 3.13   The data points in the top graph are observed values of
the amplitude ratio of the reflection from the 400 km
discontinuity to the direct arrival.   Those in the lower
graph are the observed relative arrival times.   The
curves are the theoretical values predicted by models
T7 and HWA.

arm indicate that the relative arrival time between the direct and secondary arrivals in the 15° to 20° range should be of the order of a half second longer. This could be caused by either a faster direct arrival or a slower second arrival. Model T7´ is a perturbation of model T7 in which the discontinuity has been moved down 10 km to 405 km. The second arrival is about .6 sec slower at 17°. Synthetics for the model are compared with some representative observed waveforms in Figure 3.14. Model T7´ fits the long period record from Fort St. James in Canada and the short period record from Kansas City, Missouri even better than T7. However, it definitely does not fit the long period record from Lubbock, Texas. Model T7 was chosen over T7´ since it gave a better average fit. It is probable that model T7 averages over many lateral variations of this order or perhaps even larger within the study region.

The inflection in the velocity curve in HWA at a depth of 525 km is a relatively subtle feature but a very significant one nonetheless. Simpson, Mereu and King (1974) and Fukao (1977) have confirmed its existence in other parts of the world and Burdick and Anderson (1975) have provided a petrologic interpretation. Therefore, a careful statement of why the feature was not included in model T7 is required. According to Wiggins and Helmberger (1973), the small velocity inflection was included in HWA in order to fit the short period observations near 21°. A reexamination of this same data shows that the reasons for including the inflection in HWA were tenuous at best. Furthermore, model T7 adequately fits the data without the velocity inflection.

In order to establish the precise reasons why HWA included the discontinuity, a model was constructed which was exactly the same as
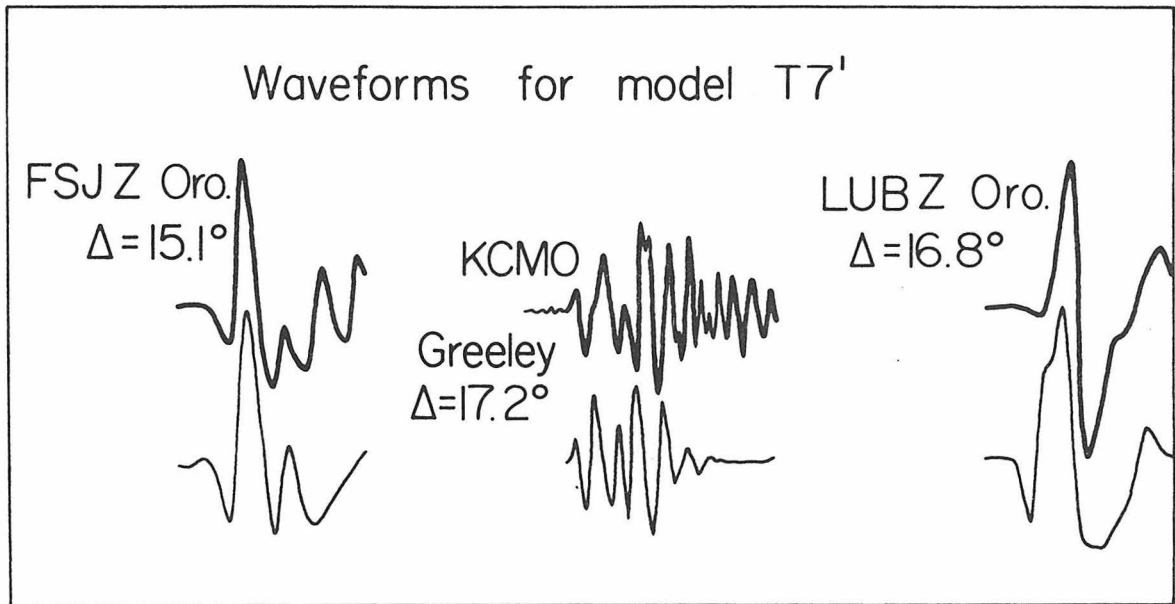
Figure 3.14 Synthetic waveforms for model T7' appear to fit some
             records like the long period waveform from FSJ or the
             short period record from KCMO even better than T7.
             It does not explain some records from the southeastern
             portion of the western U.S. such as LUB. Model T7 gives
             a better average fit to all the data.

HWA with one exception. The velocity gradient under the 425 km discontinuity was completely linear. The model was called HWA´ and is shown by the dotted line in Figure 3.9. A side by side comparison of the synthetics from HWA and HWA´ for the ranges from 18° to 23° has been made in Figure 3.15. Although there is a small difference at 21° the two sets of seismograms are for all practical purposes indistinguishable. The available short period bomb data are shown in Figure 3.16. At the most important range of 21°, model T7 **appears to fit the records from** RKON of Jorum, Greeley and Boxcar somewhat better than does HWA. Neither model can explain the anomalous record at RKON for Corduroy. Since model T7 already fits the short period data at 21°, there is no reason to add the extra complication of a discontinuity in velocity slope between the 2 major discontinuities.

The details of the second major discontinuity in the upper mantle have proved to be the most difficult to resolve. This is evidenced by the variation in its size and location from model to model. As shown in Figure 3.9, the lower discontinuity in T7 is located at a depth of 670 km, which is 20 km lower than the corresponding feature in HWA. A moderate velocity gradient is maintained under the 670 km discontinuity down to 1000 km. At this point the gradient decreases to a low value which is appropriate for the lower mantle. The lowest portion of the T7 velocity profile compares well with the model C2 (Anderson and Hart, 1976) and the model CIT 208 (Johnson, 1969).

The records which are most strongly influenced by the 670 km discontinuity are those from the ranges 24° to 28°. In this range,
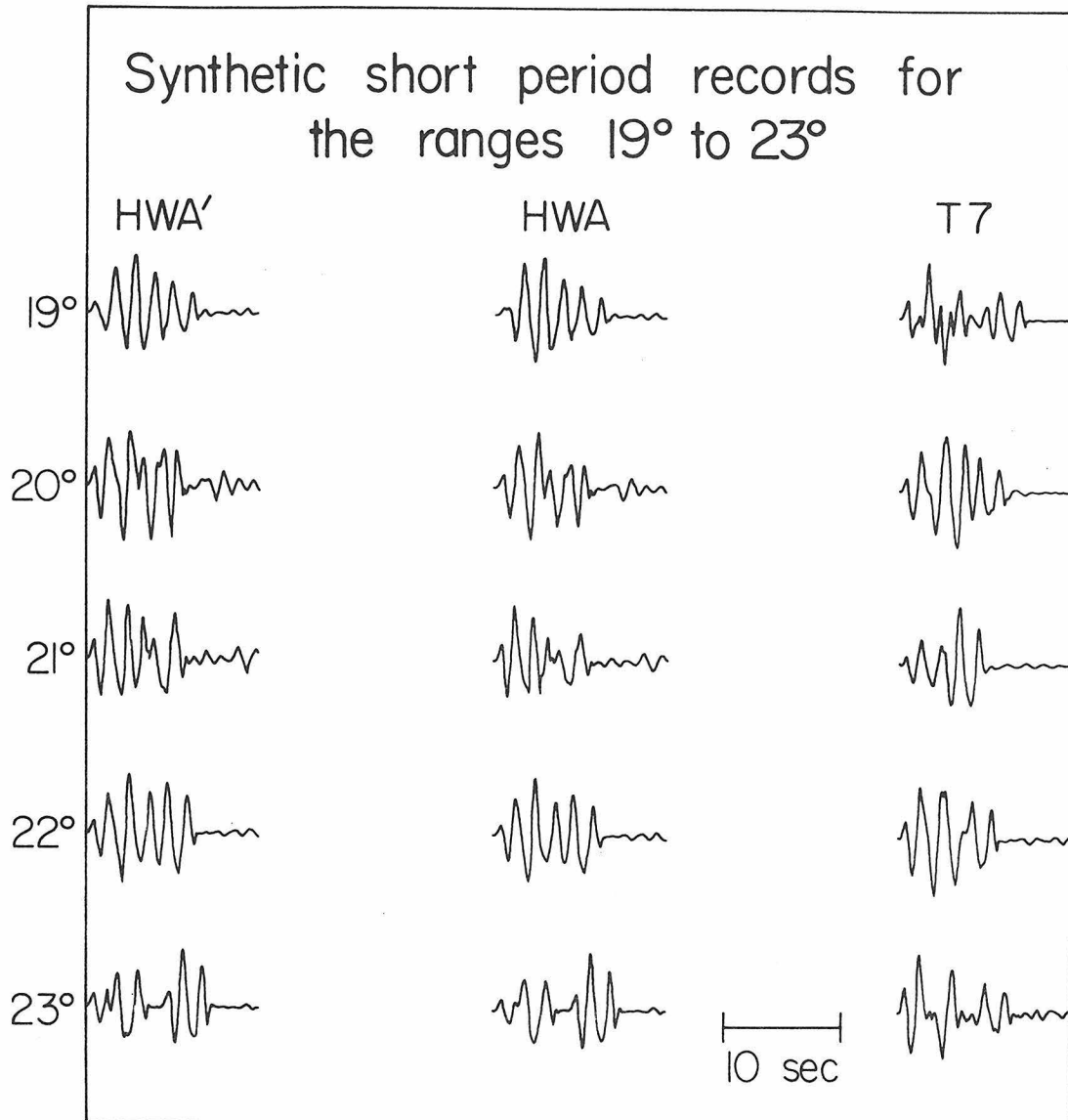
Figure 3.15 The figure compares synthetic record sections for three
different models. HWA and HWA' are different only in
that HWA has a discontinuity in velocity slope at 525
km and HWA' does not. The synthetic records for the two
models are so similar that it is impossible to say which
fits the data in the following figure better. Model T7
predicts synthetics which are different than those from
the HWA models. The T7 synthetics appear to fit more of
the data.
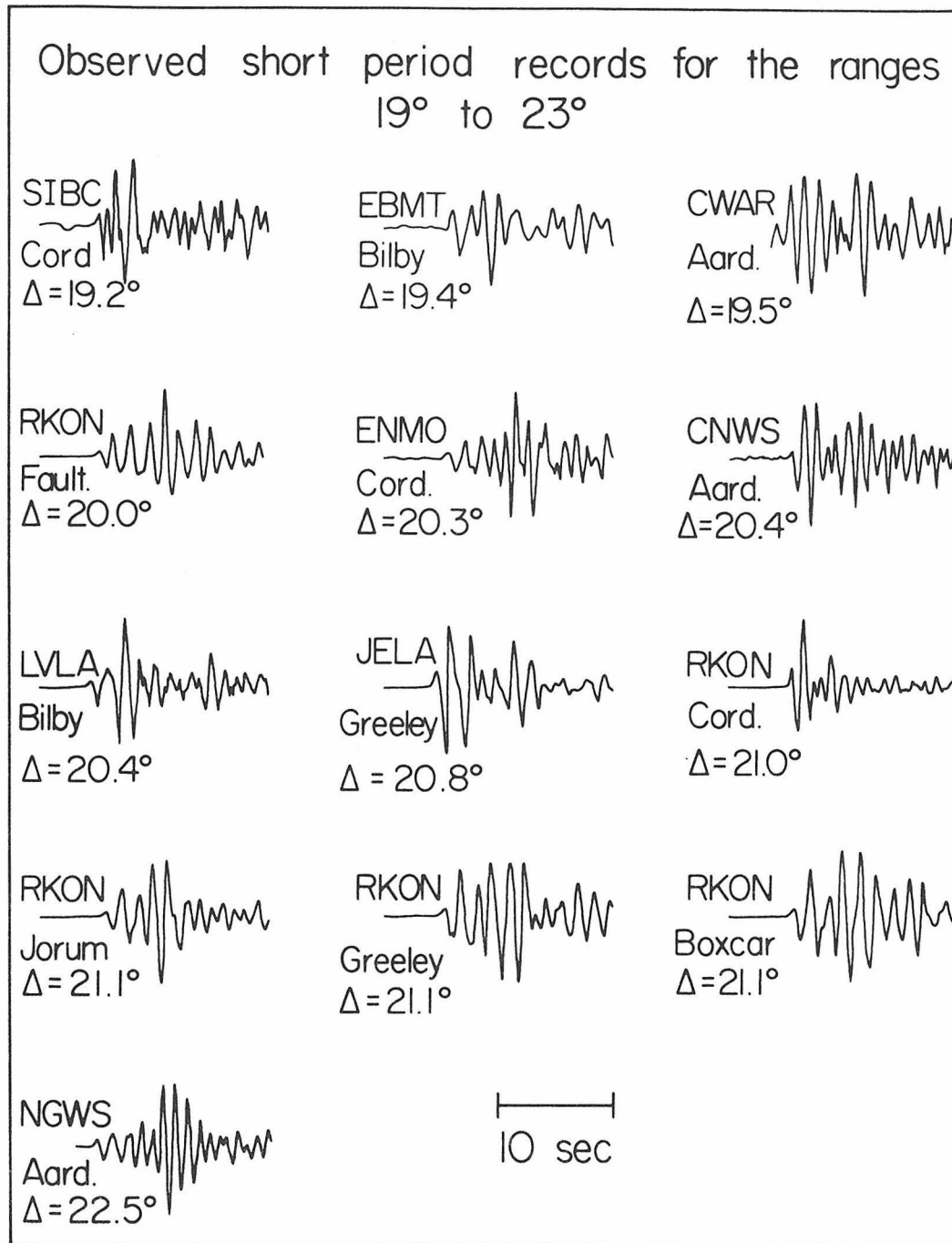
Figure 3.16   The figure shows the observed short period waveforms of bombs from ranges between 19° and 23°. The records contain reflected arrivals from both the 400 km and 670 km discontinuity. The synthetics from model T7 in the previous figure appear to fit many of these records better than the synthetics for HWA.

the first arrival comes from either the C or E branch of the travel time curve and the second arrival from the Dl branch. (See Figure 3.4.) The long period records from the 24° to 26° portion of this range are shown in Figure 17. The secondary arrival from the 670 km discontinuity is coming in just behind the direct arrival in these records. It causes the first arrival in the mantle response to appear as a two-sided function. This in turn has a strong effect on the relative amplitudes of the first and second swings of the synthetics. It is unquestionable that the 670 km discontinuity does have some effect on the waveforms at these ranges. The synthetic seismograms are significantly different from the effective source functions and at the same time very similar in form to the data. Yet these fits to the data may still not be totally convincing. No particular feature in the data can be singled out as being predominantly caused by the discontinuity. Fortunately, such features begin to emerge at succeeding ranges.

In Figure 3.18 are the long period records from the range 26° to 30°. The record from Atlanta, Georgia (ATL) at 26.5° and from Ann Arbor, Michigan (AAM) at 27.1° both clearly show the secondary arrival as a shoulder on the sP phase. Both records are from the Borrego Mountain event. The theoretical model for this event generally predicts the waveforms at stations on the east coast of North America very accurately (see Appendix 3). None of the records of Borrego Mountain from nearby stations such as Blacksberg, Virginia (BLA), State College, Pennsylvania (SCP) or Ogdensburg, New Jersey (OGP) contain an arrival like the one indicated by the arrow in Figure 3.18. Furthermore, the second arrival appears further back in the record at 27.1° than it does in the record
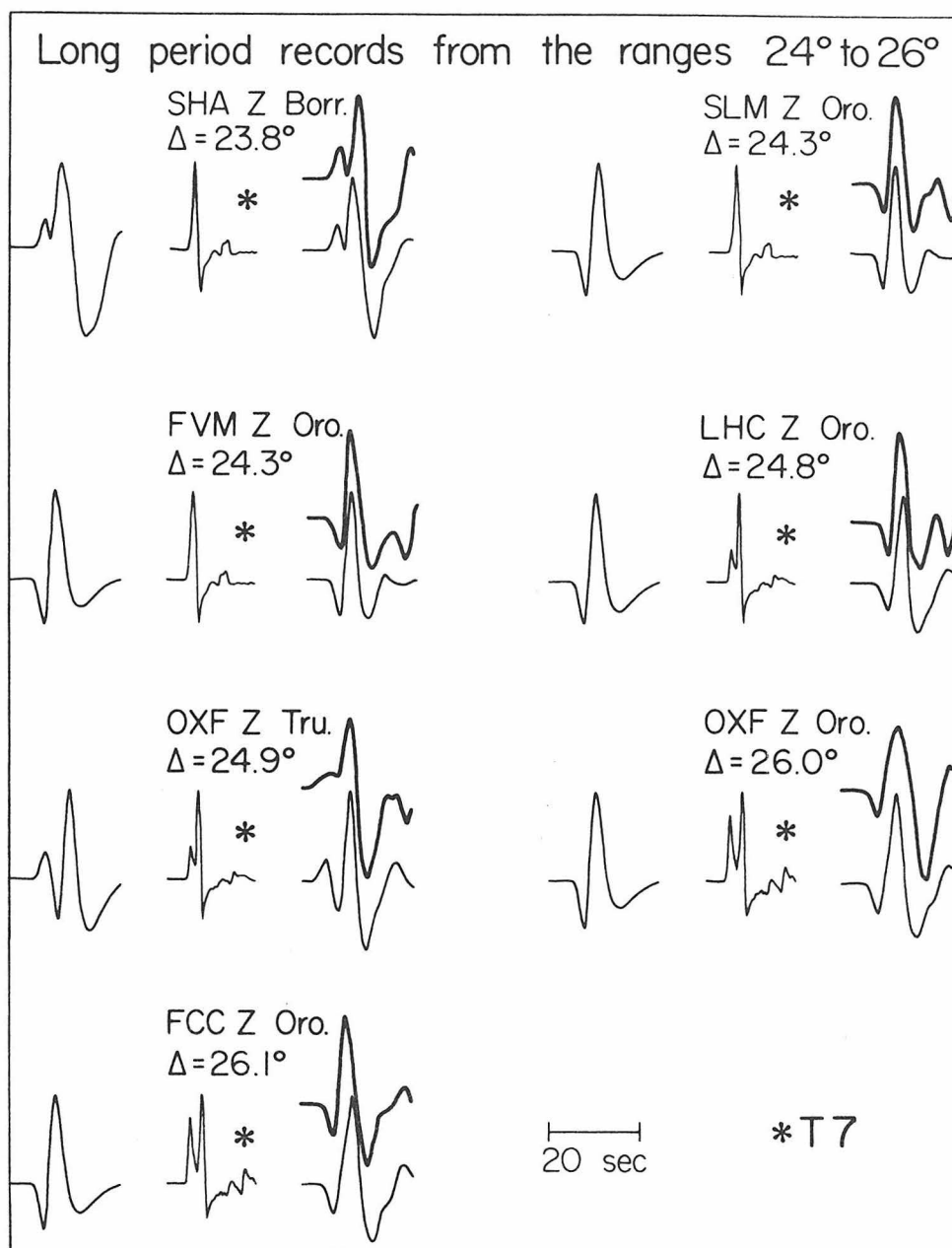
Figure 3.17 The figure compares synthetic waveforms for model T7 to the observations. The long period records contain two arrivals. The second arrival is a reflection from the 670 km discontinuity. It arrives too close to the direct arrival to appear as a separate feature, but it does affect the waveform. This can be seen by comparing the effective source pulses to the final synthetics. The organization of the figure is the same as for figure 3.10.

at 26.5°. This means that it is moving with a substantial velocity, with respect to the direct arrival. It is almost certainly a reflection from an upper mantle discontinuity. Synthetics are shown in Figure 3.18 for both HWA and T7. In the HWA synthetics, the second arrival is a few seconds too early, but the T7 synthetics match these important observations quite closely.

The observed records from greater ranges show that the D1 arrival should die out almost completely by 29°. This effect is somewhat difficult to achieve without making the arrival too small to fit the observations at 26.5° and 27.1°. Since the arrival is from the forward branch of the triplication, it is most sensitive to the structure just above the 670 km discontinuity. In model T7, the velocity just over the discontinuity has been inflected slightly upward. This has made the forward branch of the D triplication appear somewhat stunted in Figure 4. It is interesting to note from the travel time curve that no secondary critical arrival occurs past 26.0°. Therefore, all the second arrivals in Figure 3.18 are caused by long period energy refracting for long distances along the discontinuity. The records from SHA for Oroville and BLA for Borrego indicate that the decay of the D1 arrival with distance is approximately correct for T7. The record from BLC on the other hand indicates that the arrival does not quite die off quickly enough. In any case, the mantle responses in Figure 3.18 show that the secondary arrival has decayed almost completely by 29° even if it is not quite small enough.

The short period data from these ranges are poorly distributed and unstable. They are shown along with synthetics for HWA and T7 in Figure 3.19.
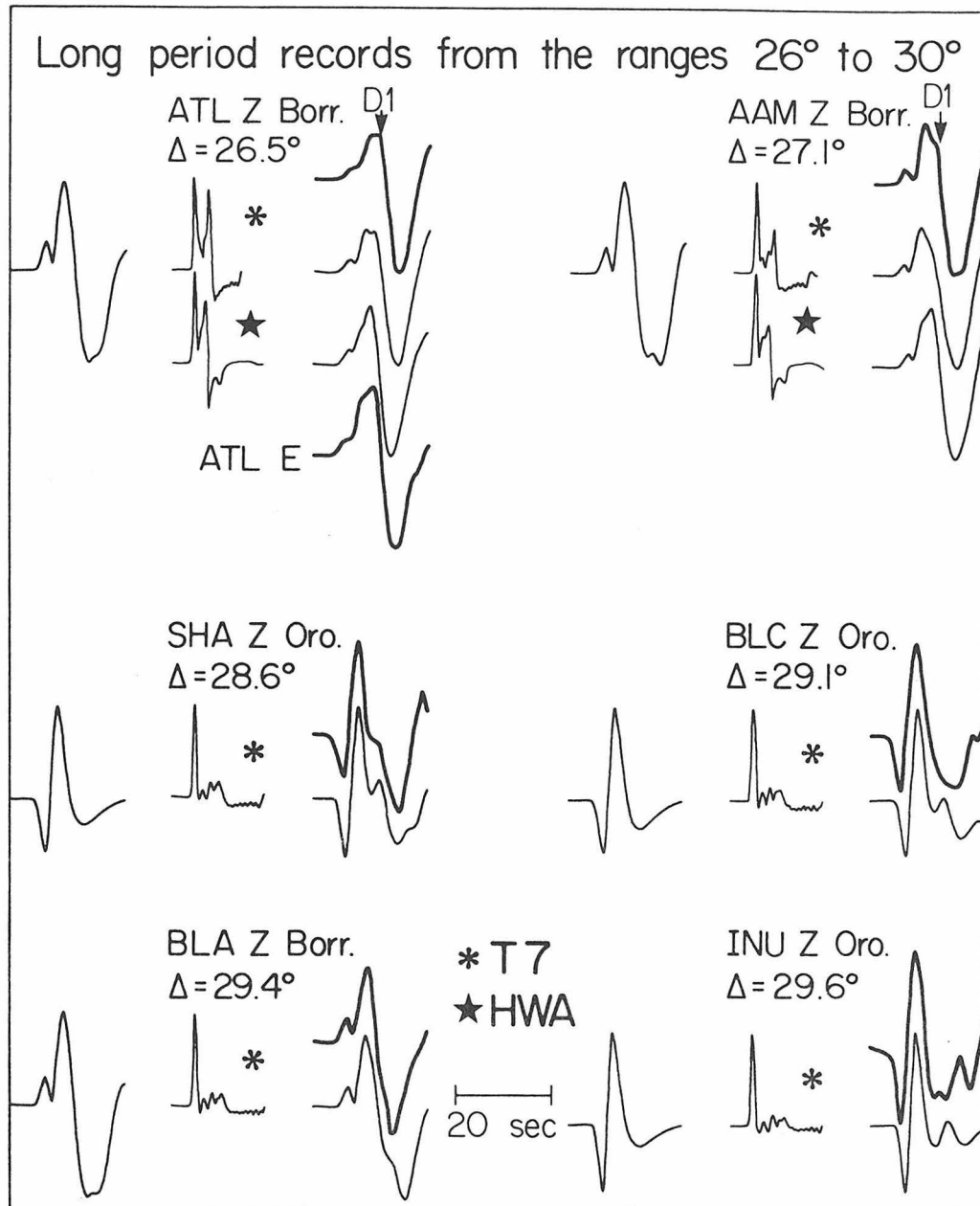
Figure 3.18 The long period records shown in the figure contain two
arrivals. The second arrival which is marked as D1 is
a reflection from the 670 km discontinuity (see Figure
3.4). The effective source function is shown on the left
for each station. The filtered delta function response
is next and, the synthetic seismogram is on the right in
light line. The observed record is on the right in dark
line. Model T7 appears to correctly predict the behavior
of the reflection, but HWA does not.
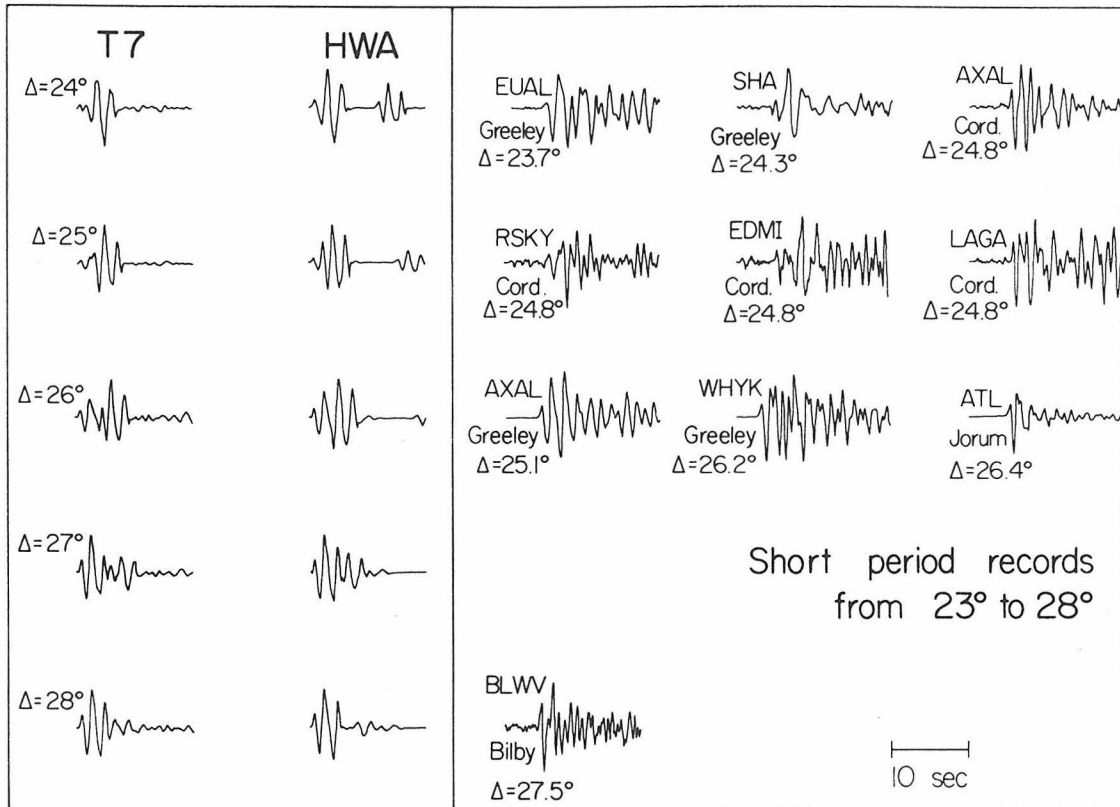
Figure 3.19 The figure compares synthetic and observed short period
records of nuclear blasts. The second arrival at these
ranges is a reflection from the 670 km discontinuity.
The synthetic waveforms for T7 and HWA are very similar
and both appear to be consistent with the data. The
arrival moving off the back of the synthetic for HWA
at 24° is a reflection from the 400 km discontinuity.

The two sets of synthetics are again so similar that it is difficult to say which resembles the data more. Both records predict that the records should have a small precursor of two or three seconds duration in the ranges 24° to 26°. The records at SHA, RSKY and EDMI tend to support this while some of the other records do not. It is difficult to draw any strong conclusions. This makes the new long period data which has been presented here even more important.

COMPARISON OF WAVEFORM ANALYSIS WITH OTHER METHODS

The process of determining upper mantle structure by waveform analysis is tedious, time-consuming and expensive. It is therefore important to establish that the method has some advantages over the more conventional methods. The western U. S. is an ideal region for a comparison of the various methods of structure determination since studies of all different types have been carried out there. For particular examples, we will choose model SDL-UT-BR1 of Masse, Landisman and Jenkins (1972) which was determined by conventional travel time analysis, CIT 204 (Johnson, 1967) which came from Wiechert Herglotz inversion of $dT/d\Delta$ data, and C2 (Anderson and Hart, 1976) which comes from inversion of travel time and free oscillation data. Synthetics have been computed for these three models and are compared with some key observed waveforms in Figure 3.20. These waveforms were selected because they show the secondary arrivals clearly. Model T7 has been shown to satisfy these observations in Figures 3.10, 3.11 and 3.18. Model SDL-UT-BR1 does not extend much below the first discontinuity, so a synthetic could only be computed for the closest range of 15.1°. As shown, the model does very poorly for this
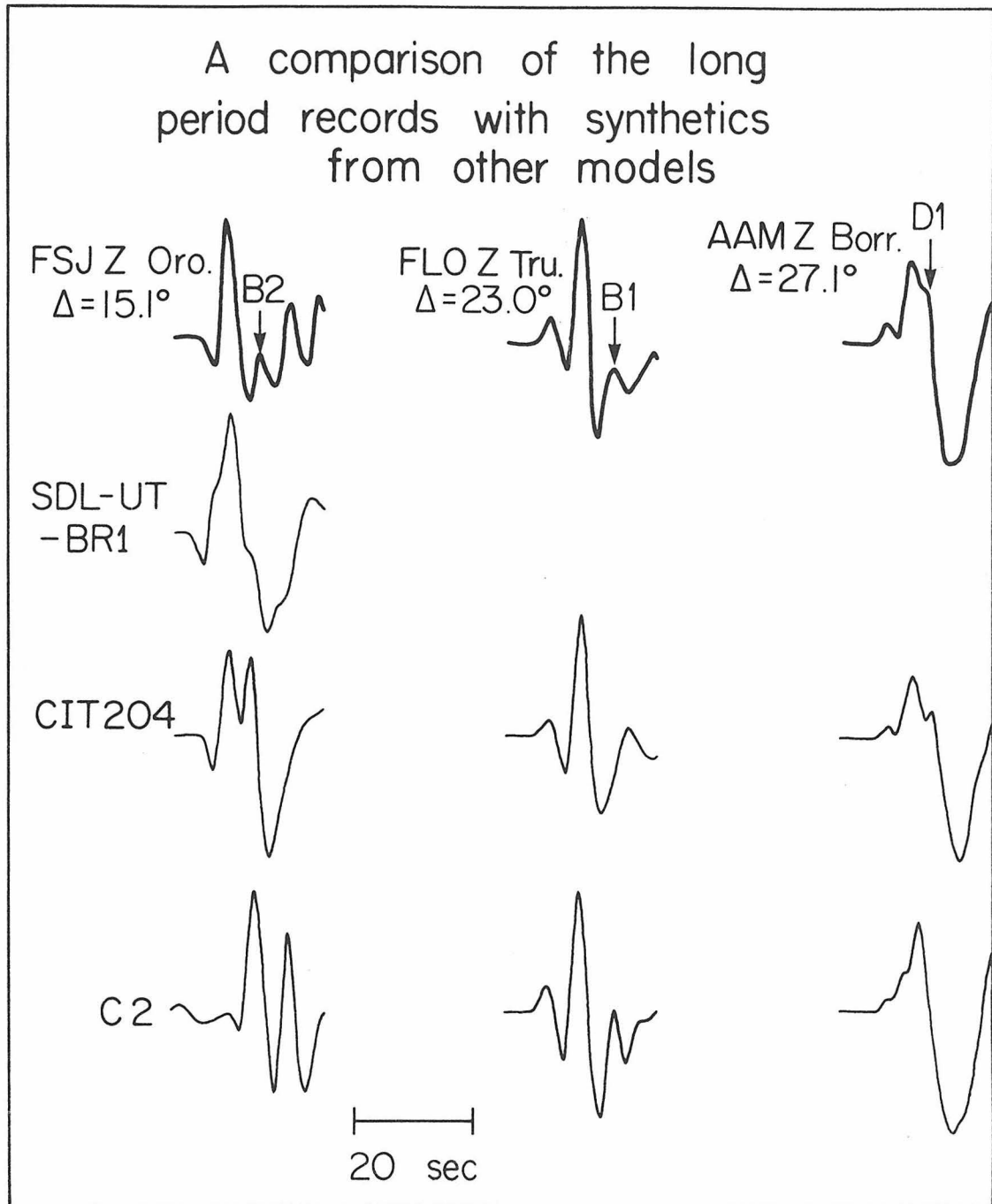
Figure 3.20 The figure compares data to synthetics for other proposed
P velocity profiles. None of them appear to fit as well
as T7. The reflected arrivals B2 and B1 are from the 400
km discontinuity and D1 is from the 670 km discontinuity
(see Figure 3.4).

record. Model CIT 204 also does poorly at 15.1^{O} and at 23.0^{O} as well. It is acceptable at 27.1^{O}. Model C2 does not fit at 15.1^{O} or at 27.1^{O} but does appear to almost fit at 23.0^{O}. In each of these cases, it is clear that the waveform data could have been used to significantly improve the model. Although conventional methods of inverting travel time, apparent velocity and mode data have been useful in controlling the gross features of the upper mantle, it seems that waveform analysis will prove to be a superior tool for constraining the finer details.

DISCUSSION

The complete model T7 is listed in Table 3.3 and shown in Figure 3.21. The preliminary shear velocity model SHR14 of Helmberger and Engen (1974) is shown next to T7 for comparison. There appear to be some strong differences between the two velocity profiles. These may indicate that Poisson's ratio varies significantly within the upper mantle. An important study for the future will be to combine the data sets from T7 and SHR14 in order to determine which of the differences between the velocity curves are well grounded in the data and which are simply artifacts.

The strong velocity gradient beneath the low velocity zone in western North America appears to put this region in the same class with western Russia (King and Calcagnile, 1976) and western Canada (Dey-Sarkar and Wiggins, 1976a). These areas can be contrasted with those which have a very weak or perhaps even negative velocity gradient in the 200 to 350 km portion of the upper mantle. This class of regions includes the

TABLE 3.3   MODEL T7

Layer	Depth to Bottom (km)	$\alpha \frac{km}{sec}$	Layer	Depth to Bottom (km)	$\alpha \frac{km}{sec}$
1	20	6.00	46	450.0	9.43
2	35	6.50	47	460.0	9.46
3	45	7.95	48	470.0	9.50
4	55	8.00	49	480.0	9.54
5	65	8.05	50	490.0	9.58
6	73.1	7.75	51	500.0	9.62
7	89.8	7.72	52	510.0	9.65
8	103.3	7.70	53	520.0	9.69
9	117.5	7.73	54	530.0	9.73
10	127.0	7.77	55	540.0	9.77
11	135.7	7.83	56	550.0	9.81
12	144.4	7.88	57	560.0	9.84
13	150.5	7.94	58	570.0	9.88
14	156.4	8.03	59	580.0	9.92
15	162.3	8.11	60	590.0	9.96
16	168.2	8.19	61	600.0	10.00
17	180.0	8.25	62	610.0	10.03
18	190.0	8.28	63	620.0	10.07
19	200.0	8.30	64	630.0	10.12
20	210.0	8.33	65	640.0	10.18
21	220.0	8.35	66	650.0	10.25
22	230.0	8.38	67	660.0	10.31
23	240.0	8.41	68	665.0	10.38
24	250.0	8.43	69	669.0	10.58
25	260.0	8.46	70	675.0	10.80
26	270.0	8.48	71	685.0	10.83
27	280.0	8.51	72	695.0	10.86
28	290.0	8.54	73	705.0	10.89
29	300.0	8.56	74	715.0	10.92
30	310.0	8.59	75	725.0	10.95
31	320.0	8.61	76	735.0	10.98
32	330.0	6.84	77	745.0	11.01
33	340.0	8.67	78	755.0	11.04
34	350.0	8.69	79	765.0	11.07
35	360.0	8.72	80	775.0	11.10
36	370.0	8.74	81	785.0	11.13
37	380.0	8.77	82	795.0	11.16
38	386.0	8.79	83	805.0	11.19
29	392.0	8.80	84	815.0	11.22
40	395.0	9.00	85	825.0	11.25
41	400.0	9.24	86	835.0	11.28
42	410.0	9.27	87	845.0	11.31
43	420.0	9.31	88	855.0	11.34
44	430.0	9.35	89	865.0	11.37
45	440.0	9.39	90	885.0	11.43
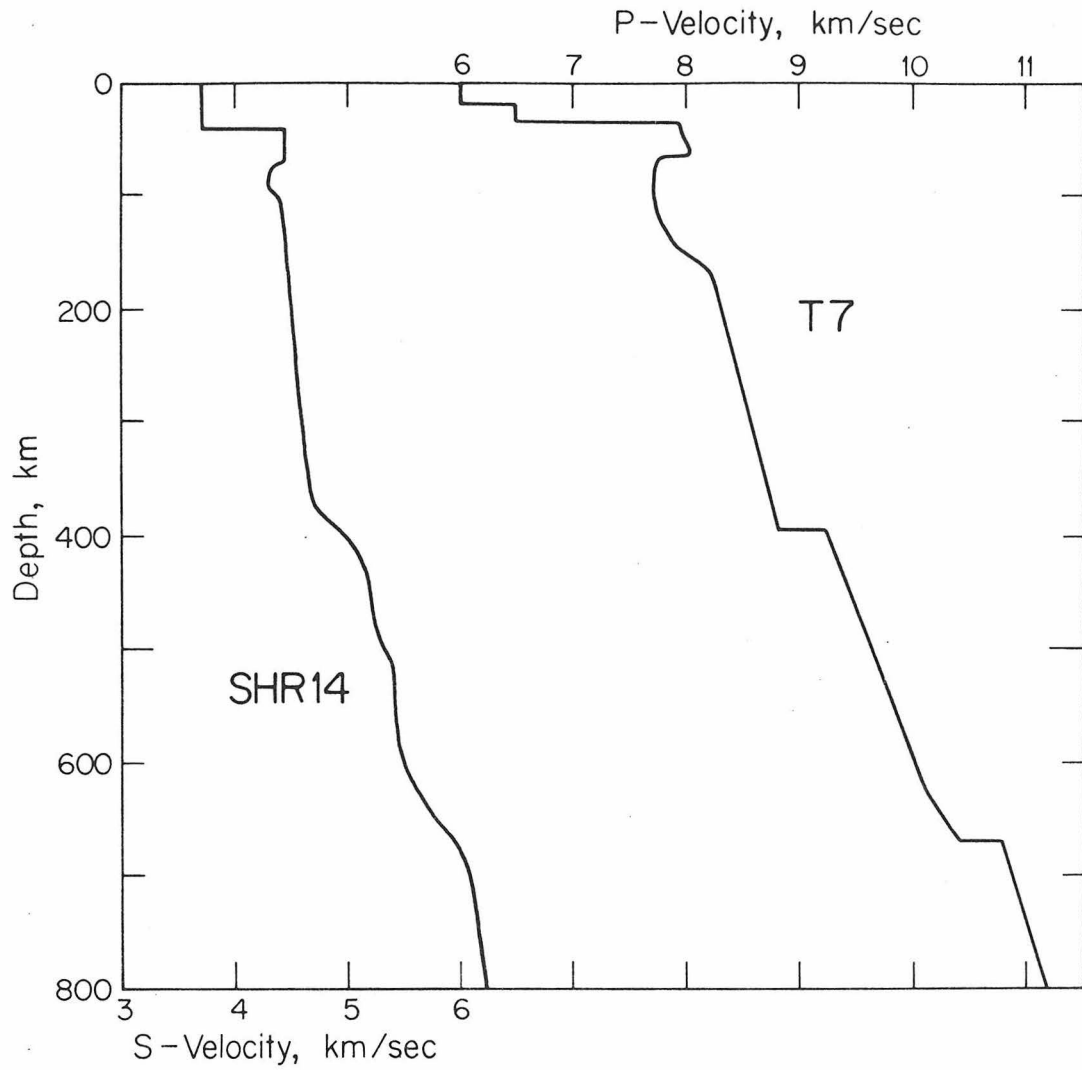
Figure 3.21 The figure compares the P velocity profile T7 with the
S wave profile SHR14. It is as yet unknown whether the
differences between the profiles are well grounded in
the data.

Japan-Kurile Arc (Fukao, 1977), the central U. S. (Helmberger and Wiggins, 1971; Green and Hales, 1968) and northeastern Australia (Simpson et al. 1974). This type of variation between different regions is one of the best documented examples of lateral variations in the mantle to date. Since the existence of these variations has been confirmed with uniform methodologies and very complete data sets, they are almost certainly manifestations of real differences in physical state within the earth.

The 5% velocity jump in T7 at the first discontinuity is relatively weak compared to the jump in many other recent compressional velocity profiles. The ARC-TR model of Fukao (1977) has a 6% jump, the KCA model of King and Calcagnile (1976) has a 7% jump and the SMAK model of Simpson et al. (1974) has a 10% jump spread out over a 100 km thick transition zone. The 4% jump at 670 km compares with a 4% jump in KCA, a 6% jump in SMAK and a 7% jump in ARC-TR. ARC-TR and SMAK both have a 550 km discontinuity while T7 and KCA do not. It has often been suggested that significant lateral variations in the mantle do not occur below 400 km depth. The differences in the lower portions of the various profiles may therefore reflect differences in method and in completeness of data sets rather than true variations in the mantle.

The method of waveform analysis is basically concerned with balancing the strength of the direct arrival against the strength of a reflected arrival from a discontinuity. Therefore the sizes of the discontinuities and the strengths of the gradients should be the best resolved features of T7. In overview, the method of long period waveform analysis appears to be stable and to have good resolution of the details of mantle structure.

An important advantage of the technique is that it can be used anywhere that moderate sized earthquakes occur. Many other methods require high quality nuclear blast sources. A final encouraging observation is that model T7 matches the recent model of King and Calcagnile (1976) very closely. Their model, KCA, appears to be T7 depressed by 20 km. This may mean that the various methods of mantle study are beginning to converge on a common picture of its structure.

Appendix 1

THE RESPONSE OF THE WWSSN SHORT PERIOD SEISMOMETER

The short period seismometer of the World-Wide Seismograph Station Network (WWSSN) records in a frequency band of .3 to 10 hertz. In this high frequency range the transducer inductance begins to have a strong effect on the behavior of the transducer-galvanometer circuit. This means that unlike most longer period instruments, which can be theoretically described by the classical equations for coupled, damped harmonic oscillators (Benioff, 1932; Chakrabarty, 1949; Eaton, 1957; Hagiwara, 1958) the WWSSN instrument requires the more general treatment given in Chakrabarty et al. (1964a, b) or Savill et al. (1962) By using this formulation it is possible to generate response curves in both the frequency and time domains which satisfy all of the available empirical data on the WWSSN short period system.

By selecting the steady state terms from Chakrabarty's et al. (1964a) equation for the response and transforming from the Laplace to the Fourier domain, the expression for the relative amplitude response A and the phase ϕ may be written

$$A(\omega) = M\omega^3 \, F(\omega) \; / \; (C^2 + B^2)^{1/2} \tag{1}$$

$$\phi(\omega) = \mathrm{Tan}^{-1} \, (B/C) - \mathrm{Tan}^{-1} \, (u(\omega)) \tag{2}$$

where

$$C = 2\epsilon_s \omega(\omega_g^2 - \omega^2) + 2\epsilon_g \omega(\omega_s^2 - \omega^2) - \sigma_i^2 \omega^2 \tag{3}$$

$$B = (\omega_s^2 - \omega^2)(\omega_g^2 - \omega^2) + (\sigma_r^2 - 4\epsilon_g \epsilon_s)\omega^2 \tag{4}$$

where

$$u(\omega) = L(r + s)\omega/Q^2 \tag{5}$$

$$F(\omega) = \frac{1}{\sqrt{1 + u^2}} \tag{6}$$

$$\omega_s^2 = \omega_{so}^2 + 2\varepsilon_{so}\omega\, u(\omega)\, F(\omega)^2 \tag{7}$$

$$\omega_g^2 = \omega_{go}^2 + 2\varepsilon_{go}\omega \left(\frac{\omega L s^2}{Q^2(R+S)} \right) F(\omega)^2 \tag{8}$$

$$\varepsilon_s = \varepsilon_{so}\, F(\omega)^2 \tag{9}$$

$$\varepsilon_g = \varepsilon_{go} \left(1 + \frac{L\omega}{(R+S)}\, u(\omega) \right) F(\omega)^2 \tag{10}$$

$$\sigma_r^2 = \sigma_o^2\, F(\omega)^4\, [1 - u(\omega)^2] \tag{11}$$

$$\sigma_i^2 = \sigma_o^2\, F(\omega)^4\, 2u(\omega) \tag{12}$$

$$Q^2 = rR + rs + sR \tag{13}$$

M is a magnification constant, L is the inductance of the transducer and R, r and s are the resistance of the transducer, galvanometer and shunt branches of the circuit, respectively (see Figure Al.1). ω_{so} and ω_{go} are the natural frequencies of the transducer and galvanometer, ε_{so} and ε_{go} their damping constants and σ_o the coupling constant as they are commonly defined for the low frequency or low inductance formulation. Chakrabarty (1949) has given expressions for these parameters in terms of the physical properties of the instrument. We have neglected the effect of the back EMF generated by the galvanometer since it has an inductance of only a few millihenries.
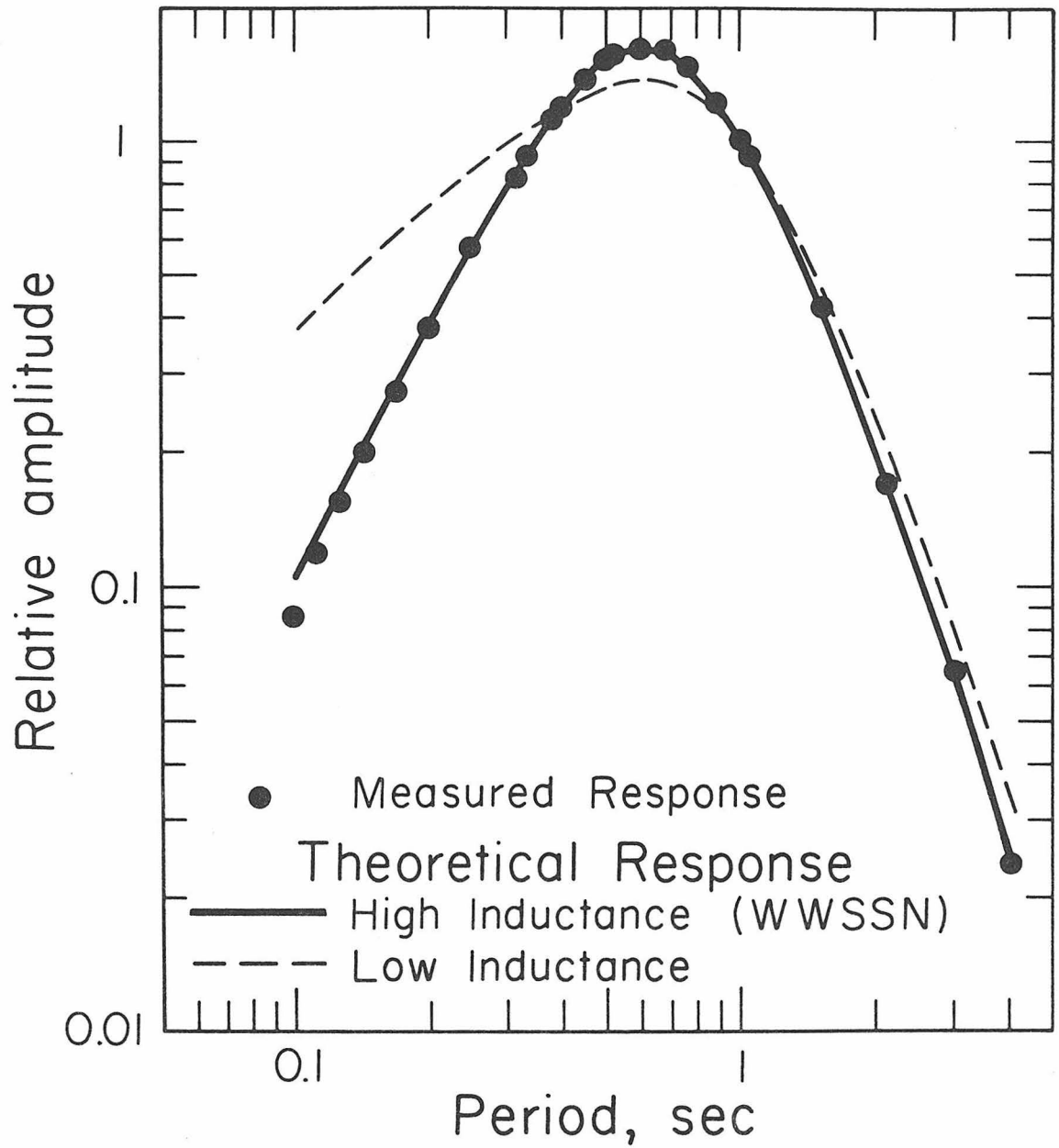
Figure A1.1 Fourier amplitude response of WWSSN short period instrument
as measured in shake table tests (points), as computed from
the formulation including inductance effects (solid line)
and as computed from classical formulation (dashed line).

Some very good empirical data on the WWSSN instrument were obtained in a shake table test performed on the system before its initial deployment. The results were published in the World-Wide Seismograph System Operations and Maintenance Manual, hereafter referred to as the WWSSOMM. The measured frequency response is shown as data points in Figure 1. A circuit equivalent (Benedict, 1967) to the one used in the experiment is shown in Figure A1.1. Two other important pieces of information are available from the WWSSOMM. The first is that when the system has the resistance configuration used in the laboratory test, the transducer is connected across its CDRX or critical external damping resistance. Since the damping constant ϵ_s is actually a function of frequency, there is no true critical damping resistance, but at this particular value, the instrument behaves as though it were critically damped when it is subjected to a weight lift test. The second piece of information is that when an instrument is operating in the field, it should react to a weight lift test as though it were slightly underdamped. It should have an initial to secondary swing ratio of 17:1. Figure A1.1 also shows the configuration of resistances which one measures in the WWSSN short period instrument presently recording at Goldstone, California (GSC). We might expect, then, that equations (1) and (2) should describe a system which has a frequency response like that shown in Figure A1.2, which behaves critically damped when in the laboratory configuration and behaves slightly underdamped when in the recording configuration.

Attenuating Network

Damp Trim
Resistor

$R = \begin{matrix} 0 \ \Omega \ (L) \\ 22 \ \Omega \ (O) \end{matrix}$ $R = \begin{matrix} 79 \ \Omega \ (L) \\ 68 \ \Omega \ (O) \end{matrix}$ $R = \begin{matrix} 83 \ \Omega \ (L) \\ 90 \ \Omega \ (O) \end{matrix}$

Transducer
Coil
L=6.8 h
R=62.5 Ω
T_o= 1.0 sec

Shunt
Resistance
$R = \begin{matrix} 0.275 \ \Omega \\ 18.0 \ \ \ \ \Omega \end{matrix} \begin{matrix} (L) \\ (O) \end{matrix}$

Galvanometer
R = 80 Ω
T_o=0.75 sec

(L) = Laboratory Test Value
(O) = General Operating Value
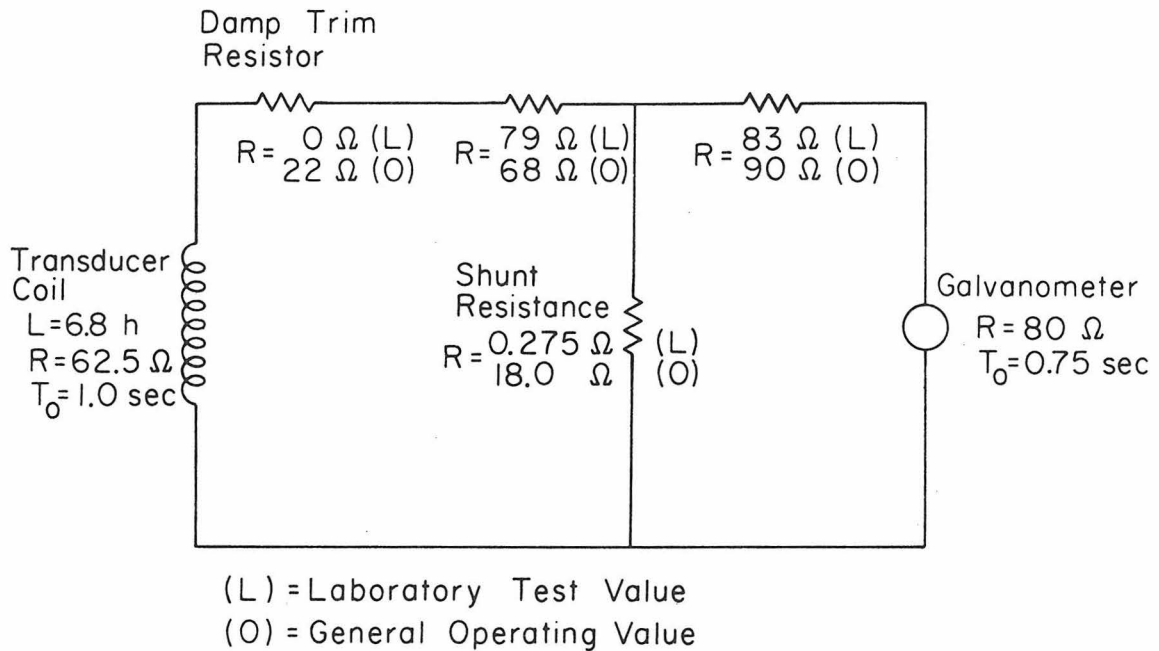
Figure A1.2 A circuit electrically equivalent to the one in the
WWSSN system with resistance values as used for the
laboratory test (L) and as used in operation (O).

Before the theoretical results can be compared with the empirical, appropriate values must be assigned to the 5 parameters ω_{so}, ω_{go}, ε_{so}, ε_{go}, and σ_o. ω_{so}, ω_{go} and ε_{go} can be adjusted independently of the transducer inductance and in the WWSSN system they are set to 1 hertz, 1.33 hertz and 1.33 hertz, respectively. σ_o is a quantity which measures the coupling between the transducer and galvanometer. As shown by Chakrabarty (1949 and 1964a), as long as s is small compared to R or r, which it is for the WWSSN system (Figure A1.1), the coupling effect is negligible and σ_o may be set equal to zero. The appropriate value for ε_{so} was not published in the WWSSOMM, so it must be determined by some other means. By ranging through the possible values for ε_{so}, we found that a very good fit to the data occurs at $\varepsilon_{so} = .583 \; \omega_o$ (Figure 1). The only remaining problems are to relate ε_{so} in the recording configuration to ε_{so} in the laboratory configuration and to make sure that the results correctly predict the system response to weight lift tests.

Chakrabarty (1949) has shown that ε_{so} is inversely proportional to the total effective circuit resistance seen by the transducer. Assuming the value of $\varepsilon_{so} = .583 \; \omega_o$ is correct for the laboratory circuit configuration we can then write

$$\varepsilon_{so} = \omega_{so} \; \frac{82.7 \; \Omega}{62.5 \; \Omega + R_{ext}}$$

where R_{ext} is the effective external resistance across the transducer. ε_{so} for the operating configuration should therefore be $.490 \; \omega_o$. To test

these values for the system parameters one can numerically model the response of a system described by equations (1) and (2) to a weight lift test. Such a test closely approximates a step in acceleration. Multiplying equations (1) and (2) by $-i\omega^3$ and transforming using an FFT algorithm we found that equations predict an overshoot ratio for the laboratory configuration of 7600:1, very close to critical. For the recording configuration they predict 16:1. It seems clear that this theoretical formulation is highly compatible with all available data on the WWSSN instrument.

Figure A1.3b shows the δ function response of the WWSSN instrument in the time domain. Figure A1.3a and the dashed line in Figure A1.2 show the response derived from the negligible inductance limit of equations (1) and (2). They are included to illustrate the importance of using the high inductance formulation in either time or frequency domain. Figure A1.4 shows a theoretical phase curve for a WWSSN instrument in its recording configuration. Note that because of the inductance the phase ranges over $5\pi/2$ radians instead of the usual 2π.
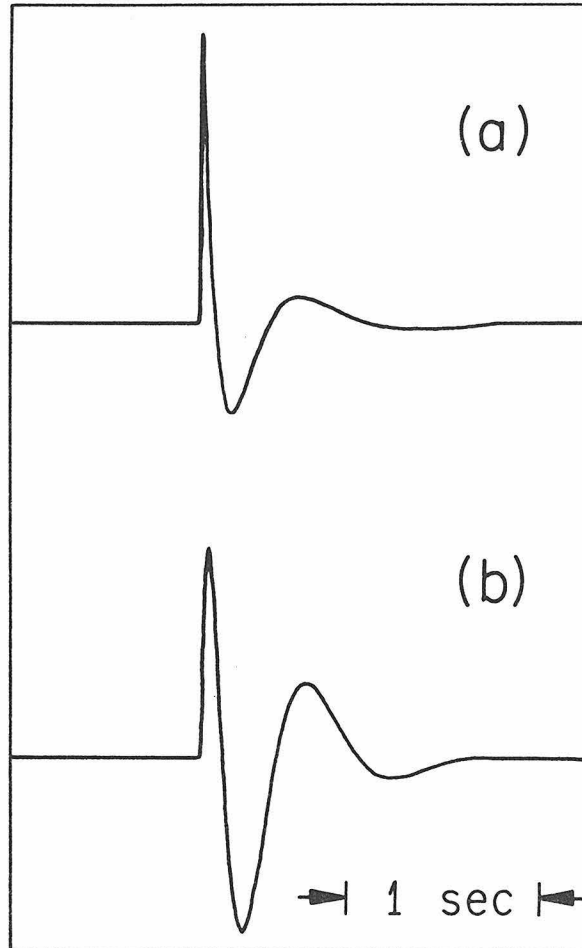
Figure Al.3 a. Time domain response of WWSSN short period instrument
             using classical formulation. b. Using formulation which
             includes inductance effects.
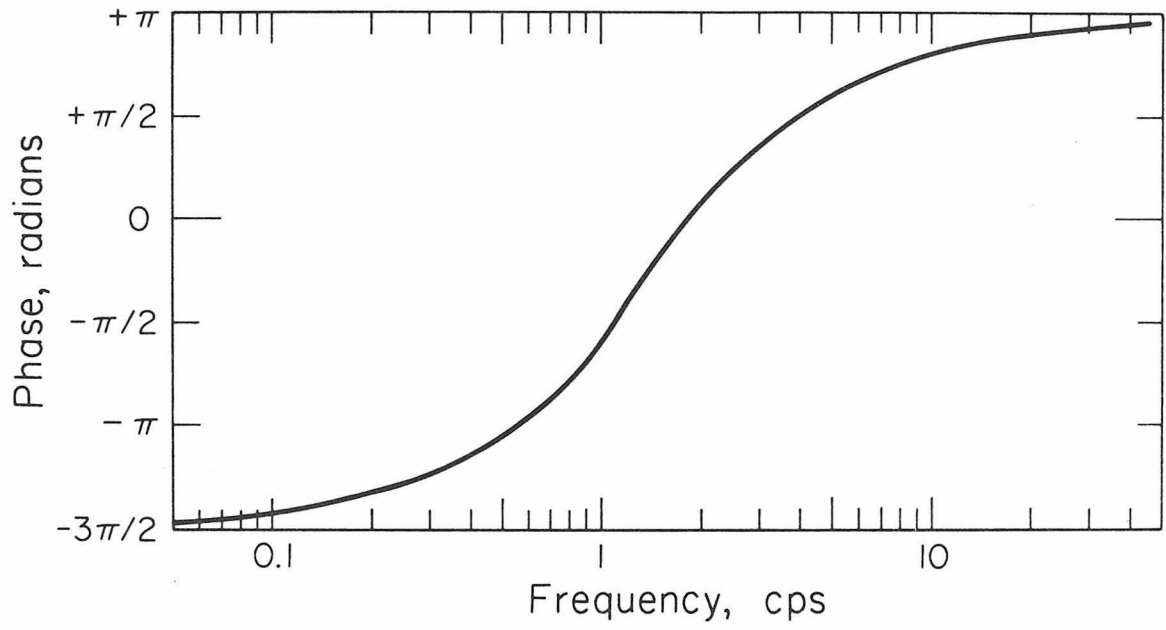
Figure Al.4   Phase response curve for WWSSN short period instrument.

Appendix 2.

FOCAL HEMISPHERES FOR SV AND SH

The focal hemisphere representation of the radiation pattern of P waves has been one of the most effective tools for studying global tectonics. The corresponding representations for SV and SH have, until now, been much less useful because the nodal curves for the shear waves are complex and difficult to interpret. The recent work of Helmberger (1974), Fukao(1971) and Bouchon (1976) has shown that such phases as sP and sS have a significant effect on body waveforms of shallow earthquakes. The work of Helmberger and Engen (1974) has shown that it is very important in shear velocity structure studies to know when a given station will record primarily SH or SV shear motion. For these reasons, a simple formalism for computing and plotting the nodes of the S radiation on the focal hemisphere proves to also be a useful tool. A formalism which accomplishes these tasks was developed early in the research program associated with this thesis. The S wave focal hemisphere plots played some role in each of the studies reported therein.

Langston and Helmberger (1975) have given expressions for the SH, SV or P wave radiation strength R for a fault with given strike, dip and rake. The variable parameters are Θ, the azimuth to the observation point as measured from the fault strike and p the ray parameter of the direct ray to the observing station. Using the same notation as these authors, the SH radiation term is

$$R = A_4(\theta) - \frac{\varepsilon \eta_\beta}{P} A_5(\theta) \qquad (1)$$

where

$$A_4(\theta) = \cos(2\theta)\cos(\lambda)\sin(\delta) - 1/2 \sin(2\theta)\sin(\lambda)\sin(2\delta) \qquad (2)$$

$$A_5(\theta) = -\sin(\theta)\cos(\lambda)\cos(\delta) - \cos(\theta)\sin(\lambda)\cos(2\delta) \tag{3}$$

$$\eta_\beta = (1/\beta^2 - p^2)^{1/2} \tag{4}$$

λ is the fault rake, δ the dip and β the shear wave speed in the source region. ε is +1 for downgoing rays and -1 for upgoing rays. For the first motion approximation, the ray parameter for a given staion is

$$p = \sin(i)/\beta \tag{5}$$

and

$$\eta_\beta = \cos(i)/\beta \tag{6}$$

where i is the takeoff angle. Substituting in equation 1 gives

$$R = A_4(\theta) - \varepsilon \cot(i) A_5(\theta) \tag{7}$$

The equation for the node where R is zero is

$$i(\theta) = \cot^{-1}\left[A_4(\theta)/(\varepsilon A_5(\theta))\right] \tag{8}$$

The expression gives the takeoff angle i for a given θ at which the radiation pattern goes through a node. The takeoff angle in a hemisphere is limited to the range between 0 and 90 degrees. Therefore, equation 8 will have no solution if the quantity in the brackets is negative. In all but one instance, the solution of $i(\theta)$ is single valued when it exists. The exception occurs for those values of λ and δ which are multiples of $\pi/2$. In this case, there are vertical nodes where at some θ the node exists at all values of i. A given radiation pattern can have either one or two vertical nodes. If it has two vertical nodes then they represent the complete solution. If it has one vertical node then that node plus an alternate solution to equation 8 are the complete solution. The factor ε in equation 8 is the only difference between the upper and

lower focal hemispheres. The simplest procedure for plotting the nodes is to first find and plot all vertical nodes. Any remaining nodal curves are then plotted as a function of Θ from equation (8).

The equation for the nodal curves for SV radiation is

$$-\epsilon_p \eta_\beta A_1(\Theta) + (\eta_\beta^2 - p^2) A_2(\Theta) + 3\epsilon p \eta_\beta A_3 = 0 \qquad (9)$$

where

$$A_1(\Theta) = \sin(2\Theta)\cos(\lambda)\sin(\delta) + 1/2 \cos(2\Theta)\sin(\lambda)\sin(2\delta) \qquad (10)$$

$$A_2(\Theta) = \cos(\Theta)\cos(\lambda)\cos(\delta) - \sin(\Theta)\sin(\lambda)\cos(2\delta) \qquad (11)$$

$$A_3 = 1/2 \sin(\lambda)\sin(2\delta) \qquad (12)$$

The solution for $i(\Theta) = 0$ is

$$i(\Theta) = 1/2 \cot^{-1} [\epsilon(A_1(\Theta) - 3A_3) / (2A_2(\Theta))] \qquad (13)$$

The expression is again single valued except for the case of vertical nodes. If there are two vertical nodes, they are the complete solution, and if there is only one vertical node, there is an additional solution of equation (13).

It is also useful to have a solution for the P wave nodes in the same format as the SH and SV solution. The node equation for P waves is

$$-p A_1(\Theta) + 2\epsilon p \eta_\alpha A_2(\Theta) + (p^2 - \eta_\alpha^2)A_3 = 0 \qquad (14)$$

where $A_1(\Theta)$, $A_2(\Theta)$ and A_3 are the same as for the SV case. η_α is computed from the compressional wave speed α. Equation (14) transforms to

$$2A_3 \cot^2(i) - 2\epsilon A_2(\Theta) \cot(i) + (A_1 - A_3) = 0 \qquad (15)$$

with solution

$$i(\Theta) = \cot^{-1} [(\epsilon A_2(\Theta) \pm \sqrt{A_2^2(\Theta) - 2A_3(A_1(\Theta) - A_3)})/(2A_3)] \qquad (16)$$

Note that the solution is double valued as it should be for some P wave fault plane orientations.

Figure A2.1 shows all six focal hemispheres for a general choice of the strike, dip and rake. The SH and SV curves are rather exotic in appearance, and it is difficult to relate them logically to the P wave solution. The shear wave focal hemisphere plots can still be a great help in understanding body wave radiation. If the observing stations for a shallow event are plotted as data points on all hemispheres, it will be easy to tell at which stations sP, pP, sS or pS are nodal. This will aid in interpreting the variation of waveform with azimuth. The S focal hemispheres can be used in the same way to decide at which stations SH will dominate.
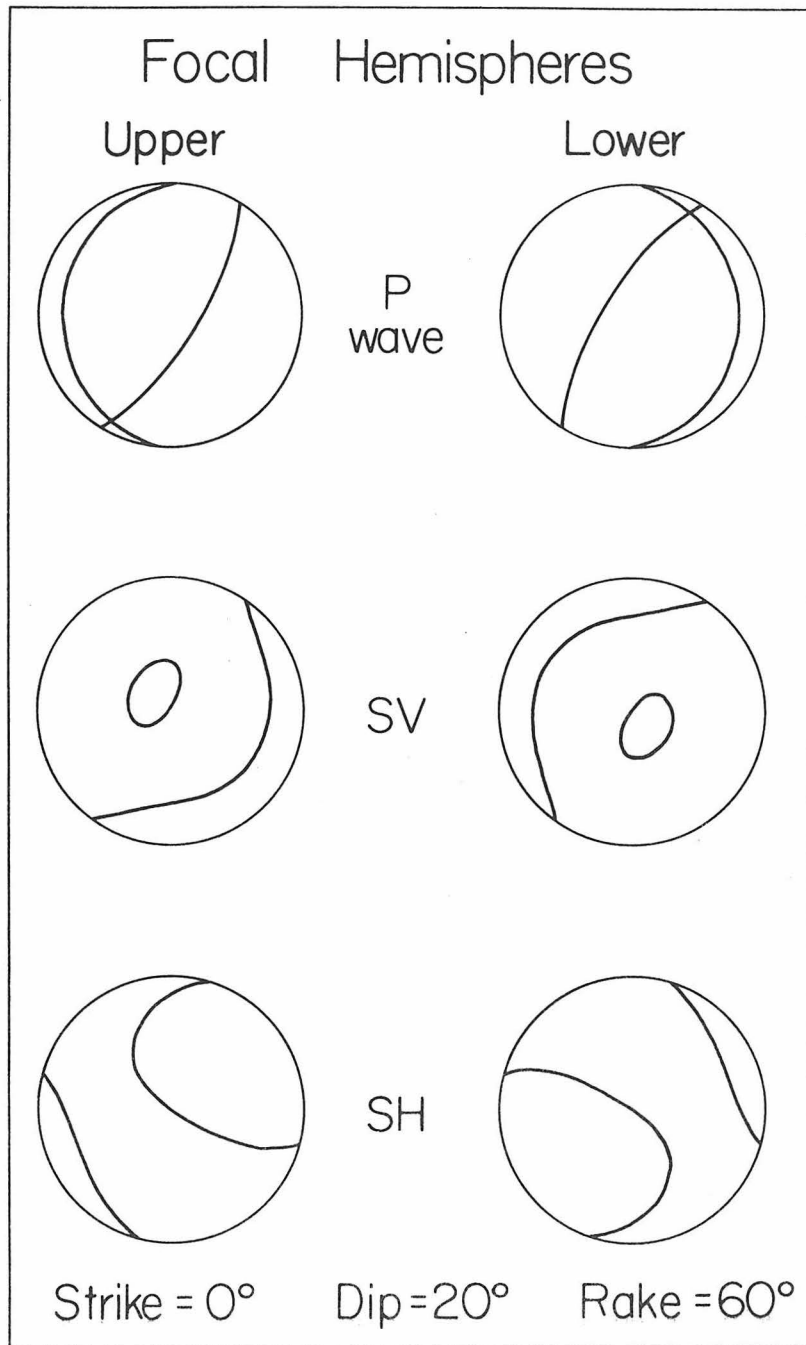
Figure A2.1   These are plots of the nodal curves for a double couple of the P, SH and SV radiation patterns.   The S wave nodal curves are generally more exotic in appearance than the P wave.

Appendix 3.

THEORETICAL SOURCE MODELS FOR BODY WAVEFORMS

The three different studies in this thesis have relied heavily on theoretical source models for the Borrego Mountain, Truckee and Oroville earthquakes. In Chapter 1, the models were used to account for the free surface effect on the far field waveforms. In Chapter 2, the Borrego Mountain model was used to identify the S, sS and sP phases. In Chapter 3, all of the models were used to predict the source pulse shapes at epicentral ranges between 10° and 30°. The purpose of this appendix is to establish that the models accurately predict the far field body waveforms for ranges between 30° and 80° where the effects of earth structure are negligible.

All three source models were parameterized in the same fashion. The unattenuated ground motion is described as a sum of geometrical rays. Each ray is represented by the same triangular time function. This function has two parameters, a rise time δt_1 and a falloff time δt_2. The source term is computed from the Langston and Helmberger (1975) expressions for the radiation of a double couple point source. The three free parameters of these expressions are the strike, dip and rake of the fault. Each pulse is lagged to the appropriate relative arrival time for the ray. The arrival time is a function of the source depth which is the final free parameter. The usual procedure for computing the unattenuated ground motion is to first compute the relative arrival time and reflection coefficients for the rays from assumed crustal models. The rays are weighted by the source term and summed in a separate calculation. The crustal models used for the three

different source models are given in Table A 3.1. The fault models
are in Table 3.2.

The fault model for the Borrego Mountain earthquake is actually
a sum of three sources. Each secondary source must also be assigned
a relative time, strength and location. The relative locations are
given in x-y coordinates where +x is north and +y is east. The fault
plane solution of the first and largest shock is identical to the one
found from first motions by Allen and Nordquist (1972). The solution
correctly predicts the observed surface wave radiation. (Rhett Butler,
personal communication). The fit of the synthetic body waves to the
observed waveforms is shown in Figure A3.1a and b. The middle trace
for each station is the synthetic computed using the triangular source
time pulses. The number N is a measure of the goodness of fit which
approaches one as the synthetic approaches the data (Burdick and Mellman
1976). The bottom trace is the synthetic computed using a circular
model of 8 km radius as described in Chapter 1. The equivalence of
the two synthetics shows that directivity is not an important effect
so long as faulting is bilateral in the vertical direction. The over-
all correspondence between data and synthetics is quite remarkable.

The fault plane solution of the Truckee earthquake is the one
found by Tsai and Aki (1970). It appears to be well constrained
by the data, and it also appears to fit the surface wave data. The good
quality far field body waveforms were very few in number because of the
small size of the earthquake. There was only one good quality long
period P wave at BLA and one poor quality one at LPS. The SH data
were somewhat better than the P. The S and sS pulses were visible at

TABLE A3.1   HALF SPACE CRUSTAL MODELS

Event	α (km/sec)	β (km/sec)	Density g/cc
Borrego	6.1	3.5	2.7
Oroville	6.0	3.5	2.7
Truckee	6.1	3.5	2.7

TABLE A3.2   SOURCE MODELS

Fault Plane Solutions and Source Depths

Event	Strike	Dip	Rake	Depth (km)
Borrego 1	− 45°	81°	178°	7.8
Borrego 2	128°	77°	12°	7.3
Borrego 3	− 91°	28°	98°	11.1
Oroville	180°	65°	−70°	5.5
Truckee	44°	80°	0	

Time Functions

Event	δt_1 (sec)	δt_2 (sec)
Borrego 1	0.4	4.5
Borrego 2	0.3	6.3
Borrego 3	0.4	4.7
Oroville	1.5	1.5
Truckee	1.0	2.0

Relative Amplitudes, Locations and Times

Event	Rel. Amp.	x (km)	y (km)	Rel. Time (sec)
Borrego 2	.22	−2.8	3.7	8.9
Borrego 3	.07	−10.3	3.7	15.3
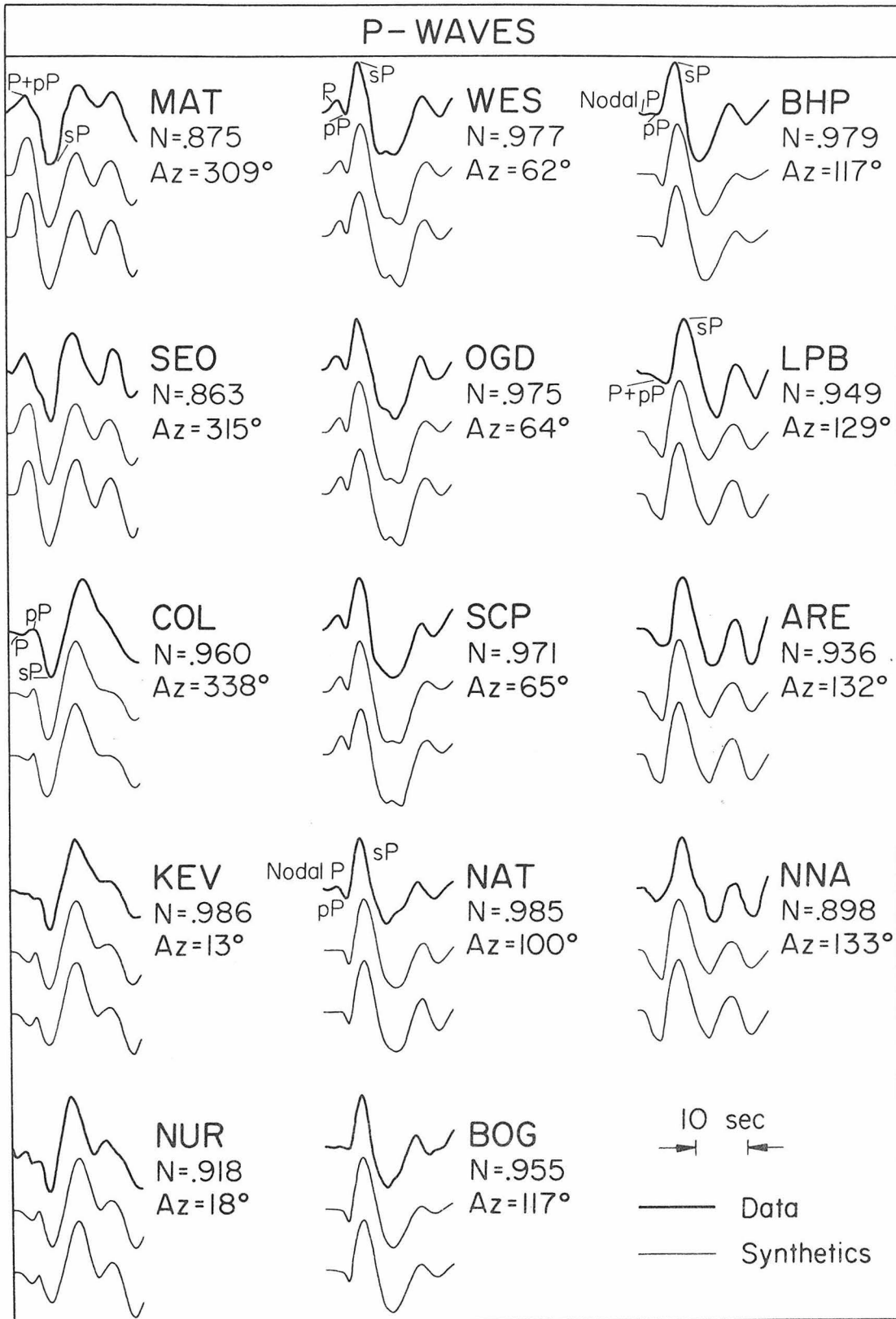
Figure A3.1a   P waveforms for the Borrego Mountain earthquake.

SH-WAVES

KEV
N=.954
Az=13°

MAL
N=.977
Az=48°

ARE
N=.980
Az=132°

UME
N=.968
Az=18°

WES
N=.959
Az=62°

NNA
N=.976
Az=133°

AKU
N=.983
Az=27°

OGD
N=.965
Az=64°

LPA
N=.971
Az=136°

ESK
N=.953
Az=33°

SCP
N=.996
Az=65°

PEL
N=.977
Az=142°

LOR
N=.940
Az=36°

LPB
N=.991
Az=129°

10 sec
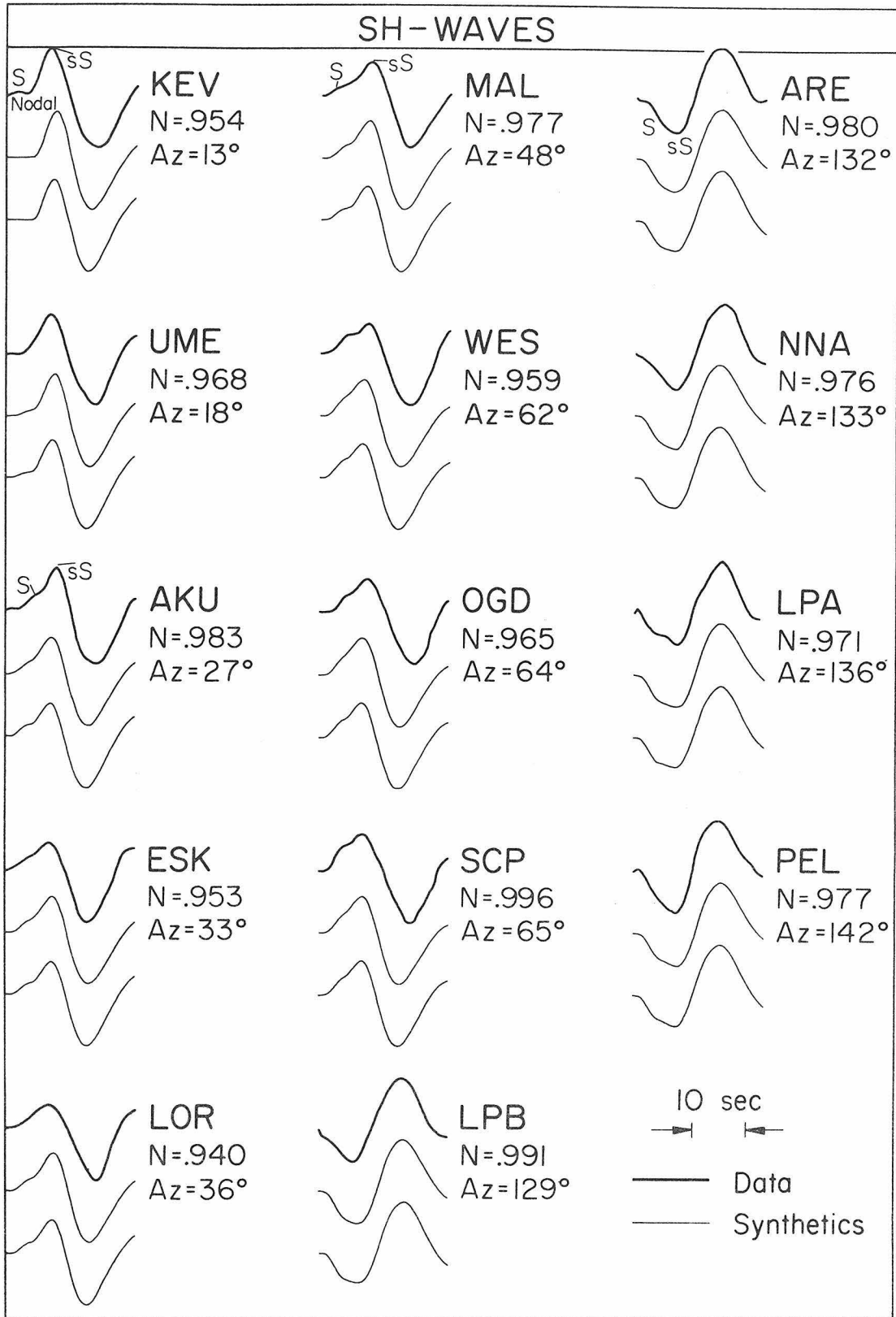
Data
Synthetics

Figure A3.1b   S waveforms for the Borrego Mountain earthquake.

a number of stations even though the noise level was still high. The synthetics and the data are compared in Figure A3.2. The amplitudes of the far field body waves indicate a moment of $.6 \pm .2 \times 10^{24}$ dyne-cm.

The source model for the Oroville earthquake was found by Langston and Butler (1976). It appears to be consistent with the first motion and surface wave data. However, none of the available data tightly constrain the strike or rake of the fault. Figure A3.3 shows the fit of the synthetics for the source model to the far field body waves. The figure is reproduced from the publication of Langston and Butler (1976) by kind permission of the authors. The correspondence between data and synthetics is very good. The accuracy of the theoretical source models in predicting the body waveforms strongly indicates that all the important physical effects are accounted for by the model. This implies that we are justified in assuming that the models can be used to interpret the far field body waveforms. We can also assume that they correctly predict the source pulses for epicentral ranges between 10° and 30°.
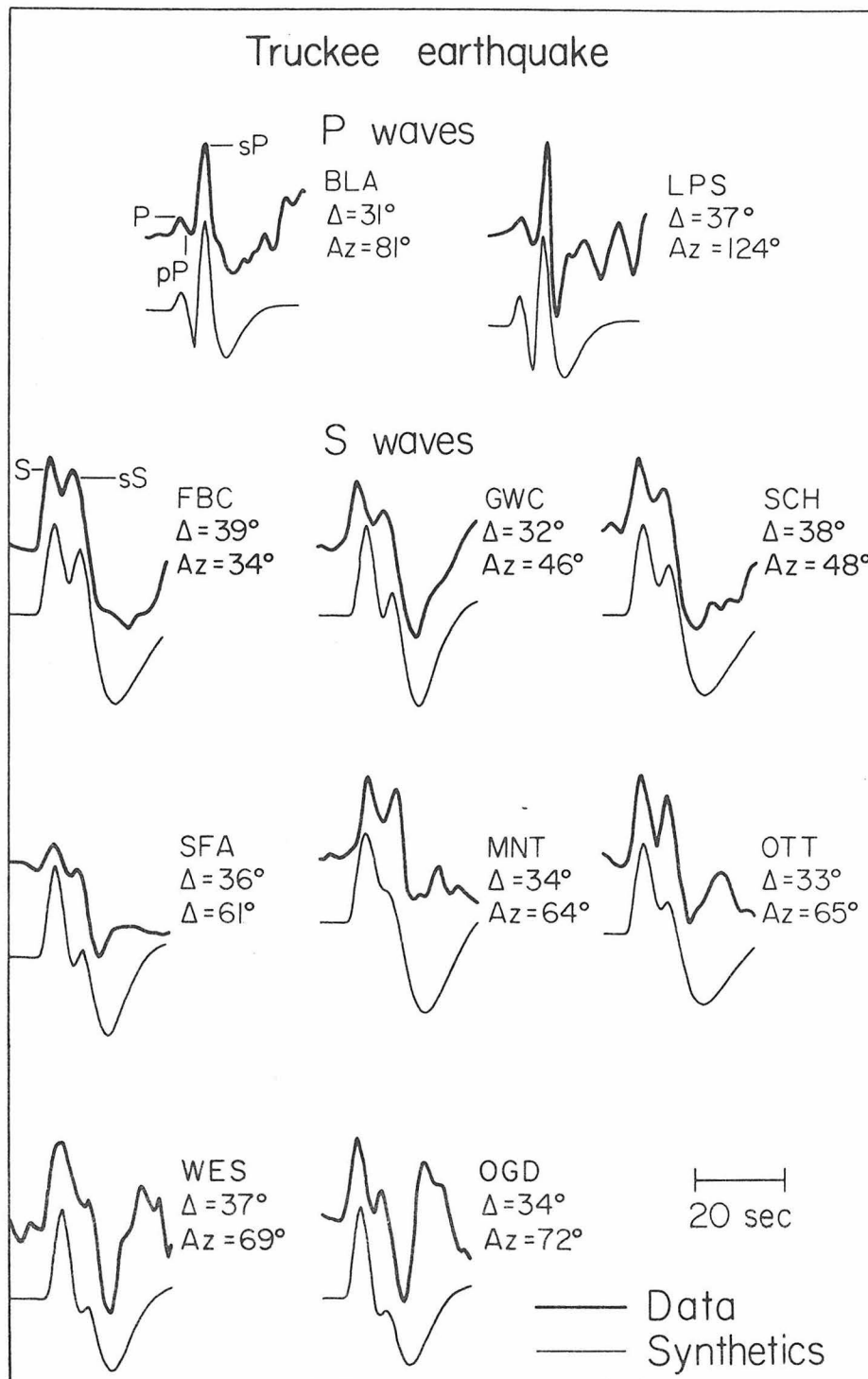
Figure A3.2 P and S waveforms for the Truckee earthquake.
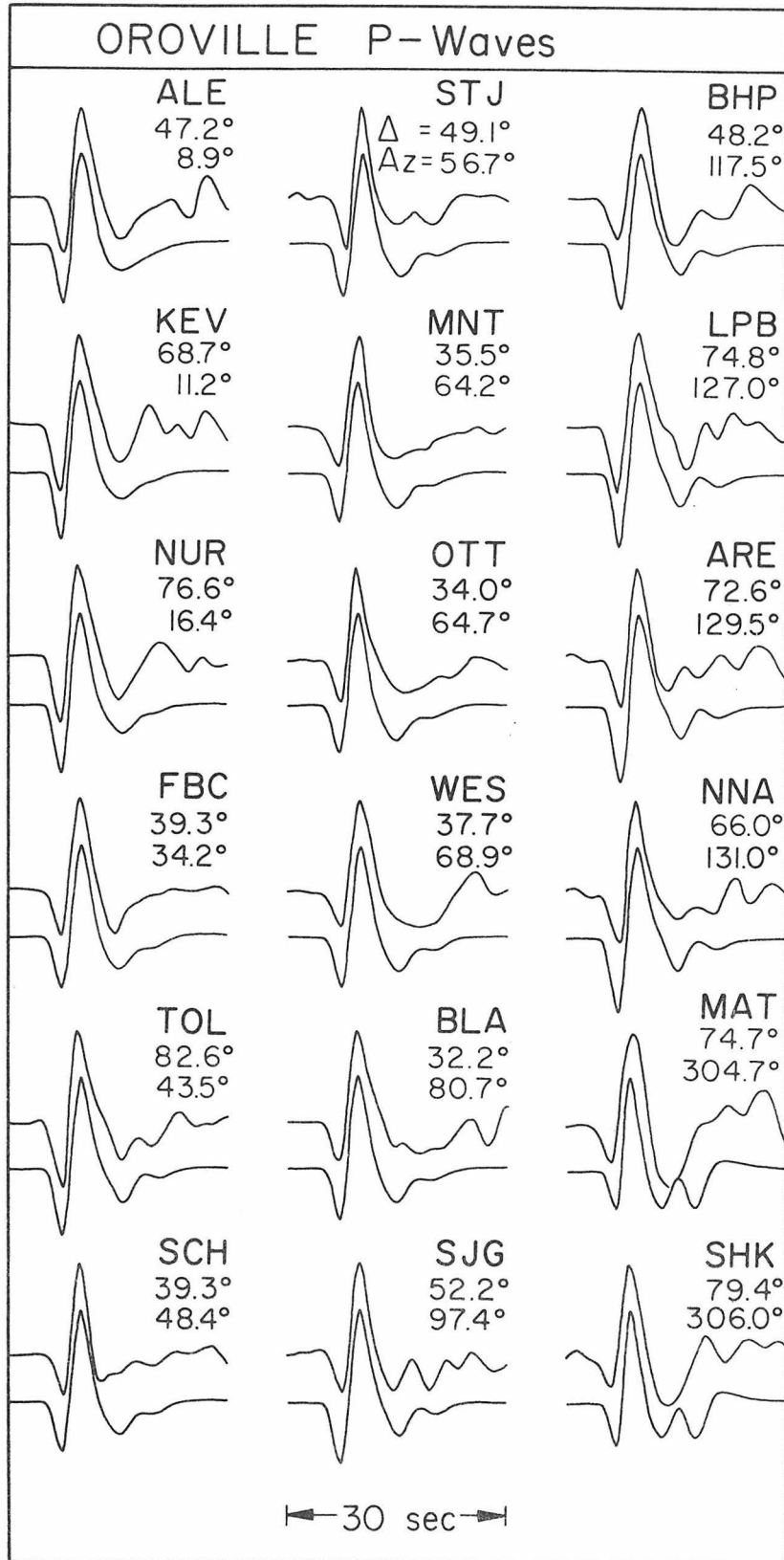
Figure A3.3 P waveforms for the Oroville earthquake.

REFERENCES

Aki, K. (1968). Seismic displacements near a fault, J. Geophys. Res., 73, 5359-5376.

Aki, K. (1972). Earthquake Mechanism, Tectonophysics, 13, 423-436.

Allen, C. R., and J. M. Nordquist (1972). Foreshock, main shock and larger aftershocks of the Borrego Mountain earthquake, U. S. Geol. Survey Prof. Paper 787, 16-23.

Alewine, R. W. (1974) Application of linear inversion theory towards the estimation of seismic source parameters, Ph.D Thesis, California Institute of Technology.

Anderson, D. L., Ari Ben Menahem, and C. B. Archambeau (1965). Attenuation of seismic energy in the upper mantle, J. Geophys. Res., 70, 1441-1448.

Anderson, D. L. and R. S. Hart (1976). An earth model based on free oscillations and body waves, J. Geophys. Res., 81, 1461-1475.

Anderson, D. L. and R. S. Hart (1944). The Q of the earth, J. Geophys. Res. (in press).

Archambeau, C. A., E. A. Flinn and D. G. Lambert (1969). Fine structure of the upper mantle, J. Geophys. Res., 74, 5825-5865.

Benedict, R. R. (1967). Electronics for Scientists and Engineers, Prentice-Hall, Inc., Englewood Cliffs, New Jersey.

Benioff, H. (1932). A new vertical seismograph, Bull. Seism. Soc. Am., 22, 155-169.

Ben-Menahem, Ari, and M. Nafi Toksöz (1962). Source mechanism from spectra of long period surface waves 1. The Mongolian earthquake of December 4, 1957, J. Geophys. Res., 67, 1943-1955.

Ben-Menahem, A., and M. Nafi Toksöz (1963a). Source mechanism from spectra of long period seismic surface waves: 3. The Alaska earthquake of July 10, 1958, Bull Seis. Soc. Am., 53, 905-919.

Ben-Menahem, A., and M. Nafi Toksöz (1963b). Source mechanism from spectra of long period seismic surface-waves. 2. The Kamchatka earthquake of November 4, 1952, J. Geophys. Res., 68, 5207-5222.

Bouchon, Michel (1976). Teleseismic body wave radiation from a seismic source in a layered medium, Geophys. J. R. astr. Soc., 47, 515-530.

Burdick, L. and D. L. Anderson (1975). Interpretation of velocity
   profiles of the mantle, J. Geophys. Res., 80, 1070-1074.

Burdick, L. J. and D. V. Helmberger (1974). Time functions appropriate
   for deep earthquakes, Bull. Seism. Soc. Am., 64, 1419-1428.

Burdick, L. J. and C. A. Langston,(1977). Modeling crustal structure
   through the use of converted phases in teleseismic body waveforms,
   Bull. Seism. Soc. Am., 67, 677-691.

Burdick, L. J. and G. R. Mellman,(1976). Inversion of the body waves
   of the Borrego Mountain earthquake to the source mechanism, Bull.
   Seism. Soc. Am., 66, 1485-1499.

Burford, R. L. (1972). Continued slip on the Coyote Creek fault after
   the Borrego Mountain earthquake, U. S. Geol. Survey Prof. Paper
   787, 105-111.

Carder, D. S., D. W. Gordan and J. N. Jordan (1966). Analysis of
   surface foci travel times, Bull Seism. Soc. Am., 56, 815-840.

Chakrabarty, S. K. (1949). Response characteristics of electro-
   magnetic seismographs and their dependence on instrumental
   constants, Bull Seism. Soc. Am, 39, 205-218.

Chakrabarty, S. K. and S. N. Roy Choudhury (1964a). Response
   characteristics of Electromagnetic seismographs, Bull. Seism.
   Soc. Am., 54, 1445-1458.

Chakrabarty, S. K., G. C. Choudhury and S. N. Roy Choudhury (1964b).
   Magnification curves of electromagnetic seismographs, Bull.
   Seism. Soc. Am., 54, 1459-1471.

Chinnery, M. A. (1963). The stress changes that accompany strike slip
   faulting, Bull. Seism. Soc. Am., 53, 921-932.

Chinnery, M. A. (1966a). Secondary faulting - I. Theoretical Aspects,
   Can. J. Earth Sci., 3, 163-174.

Chinnery, M. A. (1966b). Secondary faulting - II. Geological aspects,
   Can. J. Earth Sci., 3, 1

Choudhury, M. A. and J. Dorel (1973). Spectral ratio of short period
   ScP and ScS phases in relation to the attenuation in the mantle
   beneath the Tasman Sea and the Antarctic Region, J. Geophys. Res.,
   78, 462-469.

Clark, M. M. (1972). Surface ruptures along the Coyote Creek fault,
   U. S. Geol. Survey Prof. Paper 787, 55-86.

Clark, M. M., R. V. Sharp, R. O. Castle and P. W. Harsh (1976). Surface faulting near Lake Oroville, California, in August 1975, Bull. Seism. Soc. Am., 66, 1101-1110.

Dey-Sarkar, S. K. and R. A. Wiggins (1976a). Upper mantle structure in Western Canada, J. Geophys. Res., 81, 3619-3632.

Dey-Sarkar, S. K. and R. A. Wiggins (1976b). Source deconvolution of teleseismic P wave arrivals between 14° and 40°, J. Geophys. Res., 81, 3633-3641.

Dowling, J. and O. Nuttli (1964). Travel time curves for a low velocity channel in the upper mantle, Bull. Seism. Soc. Am., 54, 1981-1996.

Eaton, J. P. (1957). Theory of the electromagnetic seismograph, Bull. Seism. Soc. Am., 47, 37-75.

Eshelby, J. D.,(1957). The determination of the elastic field of an ellipsoidal inclusion and related problems, Proc. Roy. Soc. London, Series A, 241, 376-396.

Frazier, C. W. and J. J. Filson (1972). A direct measurement of the earth's short period attenuation along a teleseismic raypath, J. Geophys. Res., 77, 3782-3787.

Fukao, Y.(1971). Seismic body waves from surface faults, J. Phys. Earth, 19, 4, 271-281.

Fukao, Y. (1972). Source processes of a large deep-focus earthquake and its tectonic implications -- The western Brazil earthquake of 1963, Phys. Earth. Planet. Interiors, 5, 61-76.

Fukao, Y. (1977). Upper mantle P-structure at the trench-side of the Japan-Kurile Arc, Geophys. J. R. astr. Soc., (in press).

Futterman, W. I. (1962). Dispersive body waves, J. Geophys. Res., 67, 5279-5291.

Green, R. W. E. and A. L. Hales (1968). The travel times of P waves to 30° in the central United States and upper mantle structure, Bull. Seism. Soc. Am., 58, 267-289.

Greensfelder, R. (1968). Aftershocks of the Truckee, California earthquake of September 12, 1966, Bull. Seism. Soc. Am., 58, 1607-1620.

Hagiwara, T. (1958). A note on the theory of the electromagnetic seismograph, Bull. Earthquake Res. Inst., 36, 139-164.

Hamilton, R. M. (1972). Aftershocks of the Borrego Mountain earthquake from April 12 to June 12, 1968, U. S. Geol. Survey Prof. Paper 787, 31-54.

Hart, R. S., R. Butler, H. Kanamori (1977). Surface-wave constraints on the August 1, 1975 Oroville earthquake, Bull. Seism. Soc. Am., 67, 1-7.

Helmberger, D. V. (1973). On the structure of the low velocity zone, Geophys. J. R. astr. Soc., 34, 251-263.

Helmberger, D. V. (1974). Generalized ray theory for shear dislocations, Bull. Seism. Soc. Am., 64, 1, 45-64.

Helmberger, D. V. and G. R. Engen (1974). Upper mantle shear structure, J. Geophys. Res. 79, 4017-4028.

Helmberger, D. V. and R. Wiggins (1971). Upper mantle structure of the midwestern United States, J. Geophys. Res., 76, 3229-3245.

Herrin, E. (1969). Regional variations of P-wave velocity in the upper mantle beneath North America, in The Earth's Crust and Upper Mantle, Pembroke J.Hart ed., William Byrd Press, Richmond, Virginia, 242-245.

Herrmann, R. B. (1976). Focal depth determination from the signal character of long period P waves, Bull. Seism. Soc. Am., 66, 1221-1232.

Husseini, M. I. and M. J. Randall (1976). Rupture velocity and radiation efficiency, Bull Seism. Soc. Am., 4, 1173-1187.

Johnson, L. R. (1967). Array measurements of P velocities in the upper mantle, J. Geophys. Res., 72, 6309-6325.

Johnson, L. R. (1969). Array measurements of P velocities in the lower mantle, Bull. Seism. Soc. Am., 59. 973-1008.

Jordan, T. H. and S. A. Sipkin (1977). Estimation of the attenuation operator for multiple ScS waves, Geophys. Res. Letters (in press).

Julian, B. R. (1970). Regional variations in upper mantle structure beneath North America, Ph.D. Thesis, California Institute of Technology.

Julian, B. R. and D. L. Anderson (1968). Travel times, apparent velocities and amplitudes of body waves, Bull. Seism. Soc. Am., 58, 339-366.

Kachadoorian, R., R. F. Yerkes and A. O. Waananen (1967). Effects of the Truckee, California earthquake of September 1966, Bull. Seism. Soc. Am., 58, 215-248.

Kanamori, H. (1967a). Spectrum of P and PcP in relation to the mantle-core boundary and attenuation in the mantle, J. Geophys. Res., 72, 559-571.

Kanamori, H. (1967b). Spectrum of short-period core phases in relation to the attenuation in the mantle, J. Geophys. Res., 72, 2181-2186.

Kanamori, H. (1970a). Synthesis of long period surface waves and its application to earthquake source studies -- Kurile Islands earthquake of October 13, 1963, J. Geophys. Res., 75, 5011-5027.

Kanamori, H. (1970b). The Alaska earthquake of 1964: Long period surface waves and source mechanism, J. Geophys. Res. 75, 5029-5040.

Kanamori, H. and D. L. Anderson (1975). Theoretical basis of some empirical relations in seismology, Bull. Seism. Soc. Am., 65, 1073-1095.

Kanamori, H. and D. L. Anderson (1977). Importance of physical dispersion in surface-wave and free oscillation problems, Rev. Geophys. Space Phys., 105-112.

Kanamori, H. and G. S. Stewart (1976). The mechanism of the Guatemala earthquake of February 4, 1976, revealed by teleseismic surface-wave and body-wave analysis, EOS Transactions, 57, 950.

Kennett, G. L. N. (1975). The effect of attenuation on seismograms, Bull. Seism. Soc. Am., 65, 1643-1651.

King, D. W. and G. Calcagnile (1976). P wave velocities in the upper mantle beneath Fennoscandia and Western Russia, Geophys. J. R. astr. Soc., 46, 407-432.

Kovach, R. L. and D. L. Anderson (1964). Attenuation of shear waves in the upper and lower mantle, Bull. Seism. Soc. Am., 54, 1855-1864.

Lachenbruch, A. and J. Sass (1973). Thermo-mechanical aspects of the fault zone, in Proc. Conf. Tectonic Problems San Andreas Fault System. A. Nur and R. Kovach, eds., Stanford Univ. Publications in the Geological Sci., 13.

Lahr, K. M., J. C. Lahr, A. G. Lindh, C. G. Bufe and F. W. Lester, (1976). The August 1975 Oroville earthquakes, Bull. Seism. Soc. Am., 66, 1085-1099.

Langston, C. A. (1976). Body wave synthesis for shallow earthquake sources: Inversion for source and earth structure parameters, Ph.D. Thesis, California Institute of Technology.

Langston, C. A. (1977). The effect of planar dipping structure on source and receiver responses for constant ray parameter, Bull. Seism Soc. Am., (in press).

Langston, C. A. and R. Butler (1976). Focal mechanism of the August 1, 1975 Oroville earthquake, Bull. Seism. Soc. Am., 66, 1111-1120.

Langston, C. A. and D. V. Helmberger (1975). A procedure for modeling shallow dislocation sources, Geophys. J. R. astr. Soc., 42, 117-130.

Lee, Y. W. (1960). Statistical Theory of Communication, John Wiley, New York, 509 pp.

Lehmann, I. (1962). The travel times of the longitudinal waves of the Logan and Blanca atomic explosions and their velocities in the upper mantle, Bull. Seism. Soc. Am., 52, 519-526.

Lehmann, I. (1964). On the travel times of P as determined from nuclear explosions, Bull. Seism. Soc. Am., 54, 123-139.

Lehmann, I. (1967). On the travel times of P as obtained from the nuclear explosions Bilby and Shoal, Phys. Earth and Planet. Interiors, 1, 14-23.

Liu, H. P., D. L. Anderson, H. Kanamori (1976). Velocity dispersion due to anelasticity, Geophys. J. R. astr. Soc., 47, 41-58.

Marshall, P. D., A. Douglas, B. J. Barley, J. A. Hudson (1975). Short period teleseismic S waves, Nature, 253, 181-182.

Massé, R. P., M. Landisman and J. B. Jenkins (1972). An investigation of the upper mantle compressional velocity distribution beneath the Basin and Range Province, Geophys. J. R. astr. Soc., 30, 19-36.

Mikumo, T. (1971). Source processes of deep and intermediate earthquakes as inferred from long period P and S waveforms, J. Phys. Earth, 19, 303-320.

Mikumo, T. and T. Kurita (1968). Q distribution for long period P waves in the mantle, Bull. Seism. Soc. Am., J. Phys. Earth, 16, 11-36.

Morrison, P. W., B. W. Stump and R. Uhrhammer (1976). The Oroville earthquake sequence of August 1975, Bull. Seism. Soc. Am., 66, 1065-1084.

Niazi, M. (1969). Use of source arrays in studies of regional structure, Bull. Seism. Soc. Am., 59, 1631-1643.

Niazi, M. and D. L. Anderson (1965). Upper mantle structure of western North America from apparent velocities of P waves, J. Geophys. Res., 70, 4633-4640.

Operation and Maintenance Manual World-Wide Seismograph System, Model 10700, The Geotechnical Corporation, 3401 Shiloh Road, Garland, Texas.

Pakiser, L. C. (1963). Structure of the crust and upper mantle in the western United States, J. Geophys. Res., 68, 5747-5756.

Pakiser, L. C. and I. Zietz (1965). Transcontinental crustal and upper mantle structure, Rev. Geophys., 3, 505-520.

Prodehl, C. (1970). Seismic refraction study of crustal structure in the western United States, Geol. S. Am. Bull., 81, 2629-2646.

Randall, M. J. (1976). Attenuative dispersion and the frequency shifts of the earth's free oscillations, Phys. Earth Planet. Int., 12, 1-4.

Rodgers, D. A. and M. A. Chinnery (1973). Stress accumulation in the transverse ranges, Southern California, in Proc. Conf. Tectonic Problems San Andreas Fault System, A. Nur and R. Kovach, eds., Stanford Univ. Publications in the Geological Sci., 13.

Romney, C., B. G. Brooks, R. H. Mansfield, D. S. Carder, J. N. Jordan and D. W. Gordon (1962). Travel times and amplitudes of principal body phases recorded from Gnome, Bull Seism. Soc. Am., 52, 1057-1074.

Sato, R. and A. F. Espinosa (1967). Dissipation in the earth's mantle and rigidity and viscosity in the earth's core determined from waves multiply reflected from the mantle-core boundary, Bull. Seism. Soc. Am., 57, 829-856.

Savage, J. C. (1966). Radiation from a realistic model of faulting, Bull. Seism. Soc. Am., 56, 577-592.

Savage, J. C. and L. M. Hastie (1966). Surface deformation associated with dip-slip faulting, J. Geophys. Res., 71, 4897-4904.

Savill, R. A., E. W. Carpenter, and J. K. Wright (1962). The derivation and solution of indicator equations for seismometer-galvanometer combinations including the effect of inductance, Geophys. J. R. astr. Soc., 6, 409-425.

Scholz, C. H., M. Wyss and S. W. Smith (1969). Seismic and aseismic slip on the San Andreas Fault, J. Geophys. Res., 74, 2049-2069.

Simpson, D. W., R. F. Mereu, and D. W. King (1974). An array study of P wave velocities in the upper mantle transition zone beneath Northeastern Australia, Bull. Seism. Soc. Am., 64, 1757-1788.

Smith, S. and M. Wyss (1968). Displacement on the San Andreas fault subsequent to the 1966 Parkfield earthquake, Bull. Seism. Soc. Am., 58, 1955-1973.

Solomon, S. C. and M. Nafi Toksöz (1970). Lateral variation of attenuation of P and S waves beneath the United States, Bull. Seism. Soc. Am. 60, 819-838.

Stewart, G. S., R. Butler, H. Kanamori (1976). Surface and body wave analysis for the February 4, 1975 Haicheng and July 27, 1976 Tangshan Chinese earthquakes, E⊕S Transactions, 57, 953.

Teng, Ta-Liang (1968). Attenuation of body waves and the Q structure of the mantle, J. Geophys. Res., 73, 2195-2208.

Tsai, Yi-Ben and K. Aki (1970). Source mechanism of the Truckee, California earthquake of September 12, 1966, Bull. Seism. Soc. Am., 60, 1199-1208.

Wiggins, R. A. and D. V. Helmberger (1973). Upper mantle structure of the western United States, J. Geophys. Res., 78, 1870-1880.

Wiggins, R. A. and D. V. Helmberger (1974). Synthetic seismogram computation by expansion in generalized rays, Geophys. J. R. astr. Soc., 37, 73-90.

Yoshida, M. and M. Tsujiura (1975). Spectrum and attenuation of multiply reflected core phases, J. Phys. Earth, 23, 31-42.